creative commons

COMMONS DEED

저작자표시-비영리-동일조건변경허락 2.0 대한민국

이용자는 아래의 조건을 따르는 경우에 한하여 자유롭게

- 이 저작물을 복제, 배포, 전송, 전시, 공연 및 방송할 수 있습니다.
- 이차적 저작물을 작성할 수 있습니다.

다음과 같은 조건을 따라야 합니다:

저작자표시. 귀하는 원저작자를 표시하여야 합니다.

비영리. 귀하는 이 저작물을 영리 목적으로 이용할 수 없습니다.

동일조건변경허락. 귀하가 이 저작물을 개작, 변형 또는 가공했을 경우에는, 이 저작물과 동일한 이용허락조건하에서만 배포할 수 있습니다.

- 귀하는, 이 저작물의 재이용이나 배포의 경우, 이 저작물에 적용된 이용허락조건을 명확하게 나타내어야 합니다.
- 저작권자로부터 별도의 허가를 받으면 이러한 조건들은 적용되지 않습니다.

저작권법에 따른 이용자의 권리는 위의 내용에 의하여 영향을 받지 않습니다.

이것은 이용허락규약(Legal Code)을 이해하기 쉽게 요약한 것입니다.

Disclaimer

dCollection

理學博士 學位論文

III 족 금속 불순물 도핑된 ZnO 나노구조의 성장과 특성 및 나노소자로의 응용

Growth and Characterization of Group III-Metal impurity doped ZnO nanostructures for the application to Nano-devices

指導敎授 張 志 豪

2010年 2月

韓國海洋大學校 大學院

應用科學科

鄭美娜

理學博士 學位論文

III 족 금속 불순물 도핑된 ZnO 나노구조의 성장과 특성 및 나노소자로의 응용

Growth and Characterization of Group III-Metal impurity doped ZnO nanostructures for the application to Nano-devices

指導敎授 張 志 豪

2010年 2月

韓國海洋大學校 大學院

應用科學科

鄭美娜

本 論文을 鄭美娜의 理學博士 學位論文으로 認准함.

위원장 양민 인

위원 장지호 인

위원 김홍승 인

위원 오동철 인

위원 이효종 인

2009年 11月 27日

韓國海洋大學校 大學院

Contents of this thesis

1. Introduction

2. Experimental

3. Growth and characterization of dispersive 0-dimensional (0D) doped ZnO nanostructures

4. Growth and characterization of integrated 1-dimensional (1D) doped ZnO nanostructures

5. Field emission properties of doped ZnO nanostructures

List of figures

List of tables

국문요약

II-VI 화합물 반도체 재료인 ZnO 물질은 다양한 나노구조를 기반으로 성장 및 응용의 관점에서 많은 연구가 진행되어 왔다. 그러나 고차원적이고 다양한 기능을 갖는 광범위한 응용을 위해서는 무엇보다도 ZnO의 물성을 조절하는 기술은 반드시 필요하다. 따라서 2000년대 중반부터 ZnO 나노 구조의 도핑에 관한 연구가 진행되어 왔고, 다양한 불순물 첨가로 인한 구조적, 광학적, 전기적, 자기적 특성에 대한 보고들이 소개된 바 있다. 특히, 많은 도펀트 중에서, group-III 족 금속 (Al, Ga, In) 불순물을 이용한 나노구조의 도핑은 ZnO 나노 구조의 자유 전하 농도를 쉽게 증가시킬 수 있다는 점에서 적합한 도펀트로써 알려져 있다. 그러나, III 족 금속 불순물 도핑시킨 ZnO 나노 구조의 연구에 있어서, 아직까지도 개선되어야 할 많은 문제점들이 존재한다; 예를 들면, 도펀트 별로 크게 차이가 나는 성장 조건에서 도핑을 시도하여 각 결과의 비교나 상호 참조가 불가능하고, 나노 구조는 다양한 형상을 가지며 이에 따른 다양한 응용이 가능함에도 실험적으로 용이하게 얻어지는 형상에 대해서만 중점적으로 진행되어 왔다. 또한 도펀트의 종류 및 농도에 따라 체계적인 변화를 고찰하는 것이 필요함에도 이러한 연구 결과는 드물어, 연구의 필요성이 지적되고 있다.

본 논문에서는 ZnO 나노구조의 전도성 제어를 통한 물성 제어 방법을 제안할 목적으로 II-VI 화합물 반도체인 ZnO 물질을 이용하여, 분산형 타입의 0차원과 집적형 타입의 1차원구조로 나누어 나노 구조로 제작하고, 3족 금속 (Al, Ga, and In) 원소를 이용하여 나노 구조에 도핑을 시도하였다. 도핑으로 인한 형상변화, 구조적, 광학적, 전기적 특성을 조사하고 불순물 도핑된 나노 구조의 전기적 특성 변화가 소자 응용에 미치는 영향에 대하여 알아보았다.

1장에서는 나노 기술에 대한 기본적인 내용과 ZnO 물성, 그리고 3족 금속 불순물 도핑된 ZnO 나노 구조의 중요성 및 본 연구의 목적에 대해여 언급한다.

2장에서는 실험부분으로서, 나노 구조의 성장 방법 및 차원을 가진 나노 구조의 특징에 대해 간단히 소개하고, 본 연구에 사용된 다양한 측정 기술에 대하여 조사하여 본다.

3장에서는 분산형 타입의 도핑된 0차원 ZnO 나노 구조의 성장과 물성에 관한 내용이다. 도핑 전, 성장 조건을 결정하고, 일정한 성장 조건 하에서, 도펀트의 물성을 고려하여 Al, Ga, In을 도핑시킨다. 또한 도핑으로 유발된 나노 구조의 형상 변화, 구조적, 광학적, 전기적 특성 변화를 고찰하였다.

4장은 III족 불순물 도핑된 집적형 1차원 나노 구조의 성장과 특성에 관한 내용이다. 도핑 전 성장 조건을 결정하고, 일정한 성장 조건 하에서 Al, Ga, In을 도핑시켰다. 또한 도핑으로 유발된 구조적, 광학적, 전기적 특성 변화에 대하여 고찰하였다.

5장에서는 도핑으로 유발된 전도성 및 형상의 변화가 나노소자 응용에 미치는 영향을 고찰하고자 한다. III족 금속 불순물 도핑된 ZnO 나노 구조를 제작하고, 이를 이용하여 전도성 변화가 소자의 동작 특성에 직접적으로 영향을 미치는 전계효과 소자를 제작하여 소자의 동작특성과 도핑된 나노 구조의 물성변화의 상관관계를 추론하였다.

마지막으로 6장에서는 본 연구에서 얻은 결과를 정리하여 요약 및 결론에 대하여 기술하였다.

KOREA MARITIME UNIVERSITY 1945 한국해양대학교

Abstract

As a II-VI binary semiconductor compound, zinc oxide (ZnO) has been attracted a lot of attention in a field of nano-science and technology. However, tailoring physical property of ZnO is essential to widen its application into the diverse functionality. There have been many studies on various impurities-doped ZnO nanostructures related with the structural, optical, electrical, and magnetic properties. Among those dopants, group-III-metal impurities (M= Al, Ga, and In) are known as an effective dopants to increase free carrier concentration in the nanostructures. But, there are some problems; for example, doping has been performed under wide various conditions, hence comparative study on effect of each dopant is still lacked. Also researches have been focused on 1-dimensional structure, disregard of diverse morphologies of nanostructure.

In this thesis, I suggest controlling physical properties of ZnO nanostructure by impurity doping. Two distinct types, dispersive 0-dimensional (0D) and integrated 1-dimensional (1D) nanostructures, are doped using group III-metal impurities (M= Al, Ga, and In) to consider various applications of nanostructure. The morphological, structural, optical, and electrical properties induced by doping were investigated, And I have discussed on the emission property of field emitter device related with the electrical property of nanostructures.

In the chapter 1, introduction of nanotechnology, physical properties of ZnO, importance of group-III metal impurities doped ZnO nanostructures, and the purpose of this study are described.

In the chapter 2, growth method, characteristic of dimensions, and various analysis principles are explained.

In the chapter 3, growth and characterization of dispersive 0D ZnO nanostructures are described. Prior to the doping, growth condition for pure ZnO nanostructures was determinated. Group-III metal impurities like as Al, Ga, and In doped nanostructures were grown under the consistent growth condition. The morphological, structural, optical, and electrical properties originated from impurity-doping were investigated.

In the chapter 4, growth and characterization of integrated 1D ZnO nanostructures are introduced. Under the consistent growth condition, impurity-doped ZnO nanostructures were synthesized. Physical property variation was investigated in terms of structural, optical, and electrical properties.

In the chapter 5, relationship between physical property of nanostructure and device performance is discussed. Field emission devices were fabricated using the group III-metal impurity doped ZnO nanostructures. The variation of the conductivity and structural properties induced by doping are prospected and experimental results are discussed.

Finally, results found from this dissertation are summarized and concluded in the chapter 6.

Chapter 1. Introduction

1.1 Nanotechnology

In the past decade, research efforts in nanoscience and nanotechnology have grown explosively worldwide. A revolution is occurring in science and technology, based on the recently developed ability to measure, applicate and grow matter on the nanoscale (1 to 100 billionths of a meter) [1].

The new behavior observed from these nanoscale size is dominated by quantum mechanics, material confinement in small structures, large surface to volume fraction, and other unique properties [1]. Atoms, molecules, clusters and nanoparticles can be used as functional building blocks for fabricating advanced and totally new phases of condensed matter on the nanometer length scale. The optimal size of those nanostructures depends on the particular property to be engineered by altering the dimensions of the building blocks, controlling their surface geometry, chemistry and assembly, it will be possible to tailor functionalities in unprecedented ways.

1.1.1 History of nanotechnology

Emergency of nanotechnology is not a rapid development in its history as shown in Fig. 1.1 [2]. The origin of nanotechnology was placed on diverse decorative objects or stainless glass of ancient times. However, the development of nanotechnology is speeding up with entering modern times. Here, some achievements summary;

The vision proposed by Richard Feynman in the famous speech "There is plenty of room at the bottom." (1959) has now become reality. Already at that time, Feynman noted that nanoscale science and engineering would require the development of new experimental techniques and of specific instrumentation. In 1980, the idea of manipulating atoms and molecules on the nanoscale was expressed as the invention of the scanning tunneling microscope (STM); Xe atoms were deposited on Ni (110) at 4 K and were displaced to form the 'IBM' logo. Next, as the remarkable work, carbon nanotubes (CNTs) as the novel material were discovered in 1991 by Sumio Ijima at the NEC fundemental research laboratory in Tsukuba, Japan. In the 2000s, each industrialized country has developed a special research program devoted to nanotechnology. The most striking example is undoubtedly the National Nanotechnology Initiative (NNI), championed by President Clinton in 2000, with a total investment that reaches several hundred million US$ per year. At the same time, individual countries within the union (e.g. Denmark and the UK) have their own nanotechnology programmes. Major efforts are accomplished in Asia, particularly in Japan, Korea, Taiwan and Singapore.

KOREA MARITIME UNIVERSITY 1945 한국해양대학교

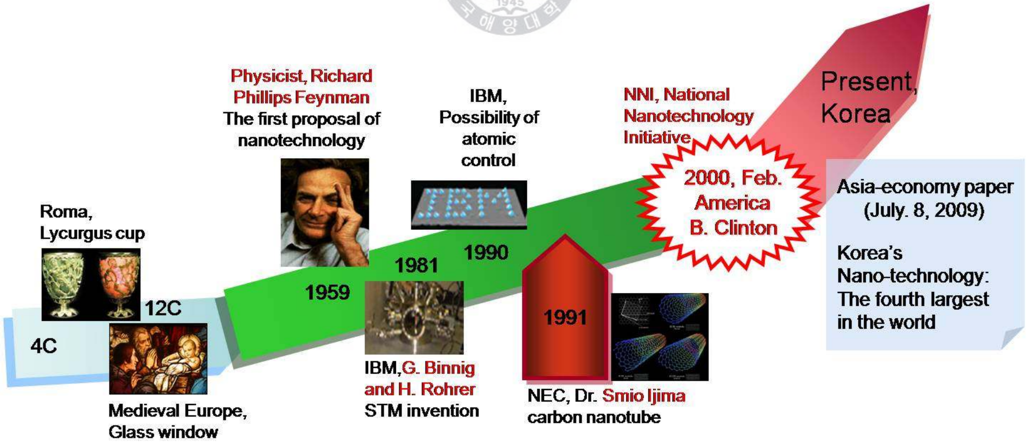

Fig. 1.1 History of nanotechnology

1.1.2 A wide area of nanotechnology

Nanoscale science and engineering will lead to better understanding of nature;

significant changes in industrial manufacturing, the economy, healthcare, and environmental management and sustainability in the Fig. 1.2. The nanotechnology of current and future includes the following [3]:

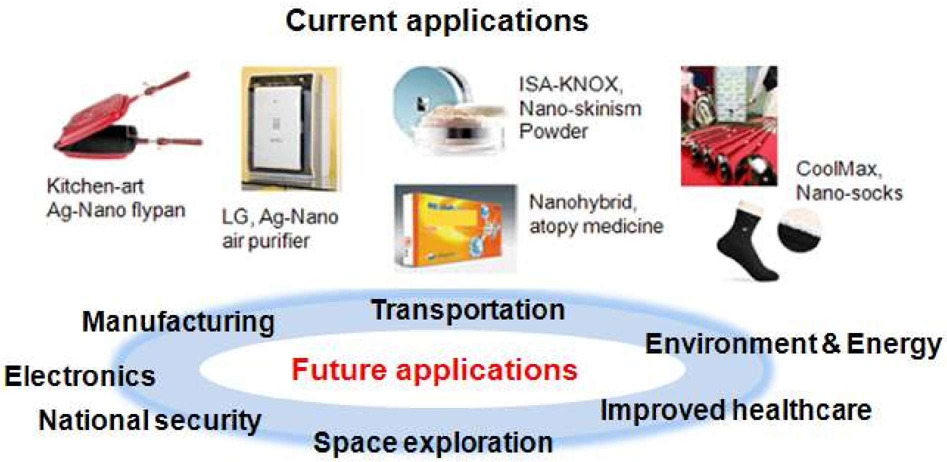

Fig. 1.2 Current and future application in the nanotechnology

KOREA MARITIME UNIVERSITY

- Manufacturing: The nanometer scale is expected to become a highly efficient length scale for manufacturing. Nanoscience provides the understanding and nanoengineering develops the tools. Materials with high performance, unique properties and functions will be produced that traditional chemistry could not create.
- Improved Healthcare: Nanotechnology will help prolong life, improve its quality, and extend human physical capabilities.
- Transportation: Nanomaterials and nanoelectronics will yield lighter, faster, and safer vehicles and more durable, reliable, and cost-effective roads, bridges, runways, pipelines, and rail systems.
- Environment: Nanoscience and engineering could significantly affect molecular understanding of nanoscale processes that take place in the environment; the

generation and remediation of environmental problems through control of emissions; the development of new "green" technologies that minimize the production of undesirable by-products; and the remediation of existing waste sites and streams. Nanotechnology also will afford the removal of the smallest contaminants from water supplies (less than 200 nanometers) and air (under 20 nanometers) and the continuous measurement and mitigation of pollution in large areas.

- Energy: Nanotechnology has the potential to significantly impact energy efficiency, storage, and production. Several new technologies that utilize the power of nanostructuring, but developed without benefit of the new nanoscale analytical capabilities.
- Space exploration: The stringent fuel constraints for lifting payloads into earth orbit and beyond, and the desire to send spacecraft away from the sun for extended missions (where solar power would be greatly diminished) compel continued reduction in size, weight, and power consumption of payloads. Nanostructured materials and devices promise solutions to these challenges. Nanostructuring is also critical to the design and manufacture of lightweight, high-strength, thermally stable materials for aircraft, rockets, space stations, and planetary/solar exploratory platforms. The augmented utilization of miniaturized, highly automated systems will also lead to dramatic improvements in manufacturing technology. Moreover, the low-gravity, high-vacuum space environment may aid the development of nanostructures and nanoscale systems that cannot be created on earth.
- National Security: Defense applications include (1) continued information dominance through advanced nanoelectronics, identified as an important capability for the military; (2) more sophisticated virtual reality systems based on nanostructured electronics that enable more affordable, effective training;

(3) increased use of enhanced automation and robotics to offset reductions in military manpower, reduce risks to troops, and improve vehicle performance; (4) achievement of the higher performance (lighter weight, higher strength) needed in military platforms while providing diminished failure rates and lower life-cycle costs; (5) needed improvements in chemical/biological/nuclear sensing and in casualty care; (6) design improvements in systems used for nuclear non-proliferation monitoring and management; and (7) combined nanomechanical and micromechanical devices for control of nuclear defense systems.

1.2 Oxide-based materials and nanostructure

Among the various materials such as metal-, carbon-, semiconductor-, and oxide-based materials, as shown in the Fig. 1.3 [4-7], oxide-based materials are one of most interesting material systems.

KOREA MARITIME UNIVERSITY 1945

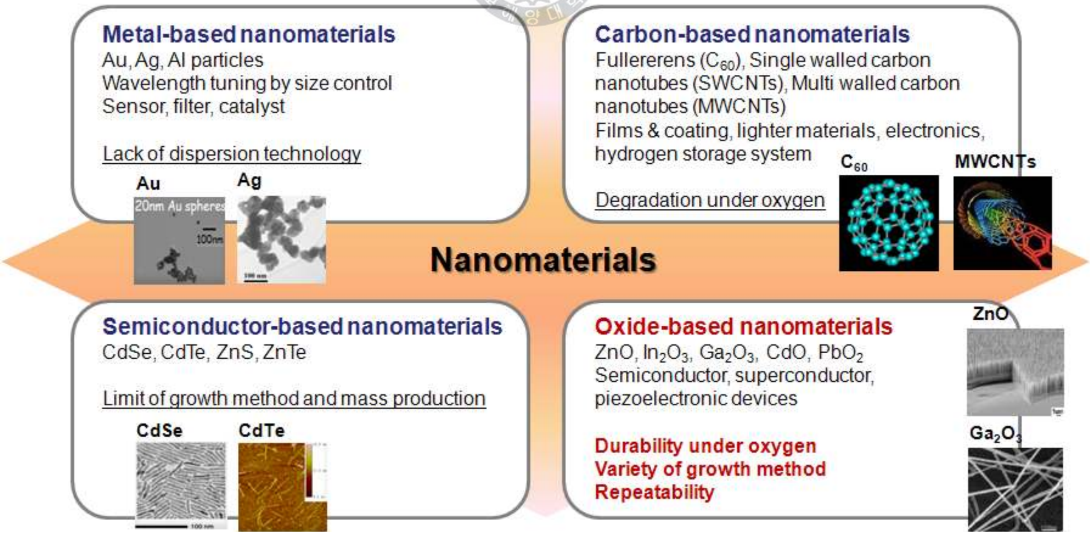

Fig. 1.3 Type of various nanomaterials

Oxides are the basis of smart and functional materials. Synthesis and device fabrication using functional oxides have been attracted a lot of attention recently because the physical properties of these oxides can be easily tuned. Functional oxides have two structural characteristics; cations with mixed valence states, and anions with deficiencies (vacancies) [8].

Table 1.1 Summary on growth method and morphology of diverse oxide-based nanostructures

Material	Nanostructures	Fabrication method	Refs.
ZnO	Belts	Thermal evaporation	[12,13]
	Wires	Thermal evaporation	[13-15]
	Rods	Thermal evaporation	[13,16]
	Rods	Gas reaction	[17]
	Rods	Metal-organic vapor-phase epitaxy	[18,19]
	Rods	Chemical vapor deposition	[20,21]
MgO	Rods	Thermal evaporation	[22]
	Wires	Thermal evaporation	[23,24]
	Belts	Chemical vapor deposition	[25]
CdO	Belts	Thermal evaporation	[12]
	Wires	Solution-phase process	[26]
MnO_2	Wires	Hydrothermal method	[27]
Mn_3O_4	Wires	Thermal evaporation	[28]
Al_2O_3	Tubes	Template method	[29]
Ga_2O_3	Belts or ribbons	Thermal evaporation	[30,31]
	Wires	Arc discharge	[32]
	Wires	Thermal evaporation	[33]
In_2O_3	Belts	Thermal evaporation	[12]
	Wires	Thermal evaporation	[34]
	Fibers	Thermal evaporation	[35]

By varying either of both of these characteristics, the electrical, optical, magnetic, and chemical properties can be tuned, giving the possibility of fabricating smart devices. The structure of functional oxides are very diverse and varied, and there are endless new phenomena and applications. Table 1.1 summaries on the synthesis method and morphology of diverse oxide material-based nanostructures. Especially, among them, ZnO has many merits. For examples, stronger durability than carbon-based materials, various growth methods for nanostructure growth, and repeatibility, and so on. It has attracted intensive research effort for its unique properties and versatile applications in transparent electronics, ultraviolet (UV) light emitters, piezoelectric devices, chemical sensors and spin electronics [9-11].

1.3 Material properties of ZnO

1.3.1 Crystal structure and lattice parameters

ZnO has two crystal phases, wurtzite structure (stable) and zinc blende (metastable). Fig. 1.4 shows the hexagonal wurtzite-type structure [10].

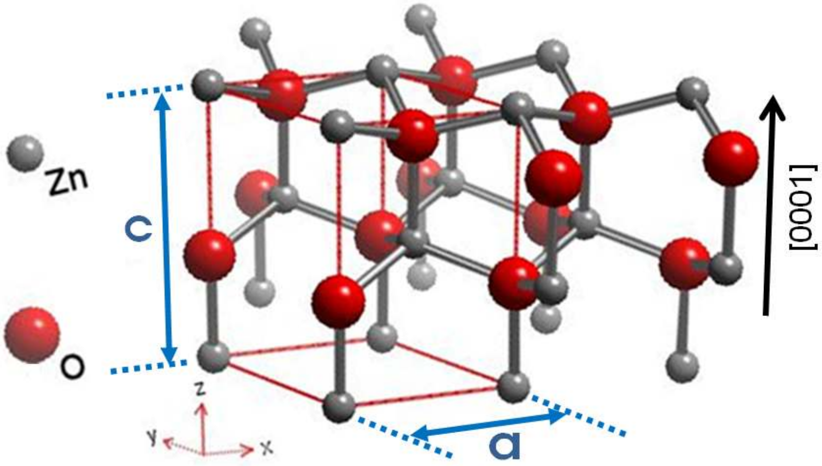

Fig. 1.4 Crystal structure of ZnO wurtzite phase

The hexagonal lattice belongs to the space group $P6_3mc$, and is characterized by two interconnecting sublattices of Zn^{2+} and O^{2-}, such that each Zn ion surrounded by a tetrahedra of O ions, and vice-versa. This tetrahedral coordination gives rise to polar symmetry along the hexagonal axis. This polarity is responsible for a number of the properties of ZnO, including piezoelectricity and spontaneous polarization, and is also a key factor in crystal growth, etching and defect generation. The four most common face terminations of wurtzite ZnO are the polar Zn terminated (0001) and O terminated $(000\bar{1})$ faces (c-axis oriented), and non-polar $(11\bar{2}0)$ (a-axis) and $(10\bar{1}0)$ faces which both contain equal number of Zn and O atoms. The polar faces are known to posses different chemical and physical properties, and O-terminated face possess a lightly different electronic structure to the other three faces [36]. Additionally, the polar surfaces and the (1010) surface are found to be stable, however the $(11\bar{2}0)$ face is less stable and generally has a higher level of surface roughness than its counterparts. The (0001) plane is also basal. The lattice parameters of the hexagonal unit cell are $a = 0.3249$ nm and $c \approx 0.5206$ nm and the density of 5.605 g/cm^3. In an ideal wurtzite crystal, the axial ratio c/a and the u parameter (which is a measure of the amount by which each atom is displaced with respect to the next along the c-axis,) were determined in the range u=0.3817-0.3856 and c/a=1.593-1.6035 [37].

1.3.2 Energy band structure

The electronic band structure of ZnO has been calculated by a number of groups [38-41]. One of the band structures was calculated using the local density approximation (LDA) incorporating atomic self-interaction corrected pseudo-potentials (SIC-PP) to accurately account for the Zn 3d electrons. Both the valence band maximum and the lowest conduction band minimum occur at the point k=0 indicating that ZnO is a direct band gap semiconductor. The higher conduction bands are free-electron-like. The O 2s bands associated with core-like energy states, occurring around -20 eV. The band gap as determined from this calculation is 3.77 eV. This agrees reasonably well with the experimental value of 3.4 eV and is much closer than the value obtained from standard LDA calculations. Experimentally the ZnO valence band is split into three band states, A, B and C by spin-orbit and crystal-field splitting. This splitting is schematically illustrated in Fig. 1.5. The A and C subbands are known to possess Γ_7 symmetry, while the middle band B has Γ_9 symmetry. These properties which combined with the lattice dynamics of ZnO give rise to interesting optical properties.

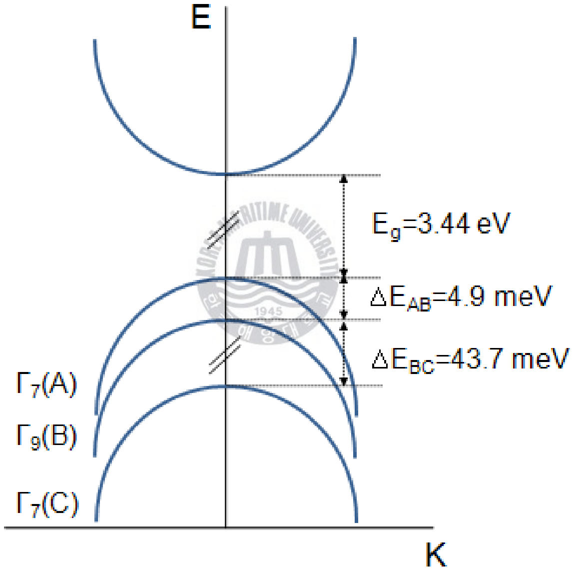

Fig. 1.5 Schematic diagram representing the crystal-field and spin-orbit splitting of the valence band of ZnO into subband states A, B and C at 4.2 K

ZnO has some advantages over GaN among which are the availability of fairly high-quality ZnO bulk single crystals and a large exciton binding energy of 60 meV. The large exciton binding energy of 60 meV paves the way for an intense near-band-edge excitonic emission at room and higher temperatures, because this value is 2.4 times that of the room-temperature (RT) thermal energy, k_BT=25 meV. Another feature is its large cohesive energy (1.89 eV), which is compared with those of ZnSe, ZnSe and GaN as shown in Table 1.2. The cohesive energy per bond (i.e. bond energy) indicates hardness of the material and influences the formation of crystalline defects. A compound having large cohesive energy is expected to be resistive against the formation of crystalline defects. Table 1.2 summarizes the comparison of structural and optical properties of ZnO with other material.

Table 1.2 Structural and optical properties of ZnO compared to other materials

material	crystal structure	lattice constant, a (Å)	c (Å)	cohesive energy, E_{coh} (eV)	melting point, T_m (K)	band-gap, (at RT) E_g (eV)	exciton binding energy, E_b (meV)
ZnO	Wurtzite	3.246	5.207	1.89	2250	3.37	60
ZnS	Wurtzite	3.823	6.261	1.59	2103	3.8	29
ZnSe	Zinc blende	5.668	-	1.29	1793	2.70	20
GaN	Wurtzite	3.189	5.185	2.24	2791	3.39	21
GaAs	Zinc blende	5.653	-	1.63	1513	1.42	4.9

1.4 ZnO-based nanostructure and applications

Nanostructured ZnO has received broad attention due to their distinguished performance in electronics, optics and photonics. Especially, since the nanotechnology initiative led by US, study of nanostructure with diverse dimensions has become a leading edge in nanostructure and nanotechnology. With decreasing in size, novel electrical, mechanical, chemical, and optical properties are introduced, which are largely believed to be the result of surface and quantum confinement effects.

As stated above, ZnO is versatile functional material that has a diverse group of morphologies [18, 42-46], such as nanowires, nanorods, tetrapods, nanobelts, nanotubes, nanosheets, nanocages, and nanocombs as shown in the Fig. 1.6. To grow different nanostructure, there are several growth parameters like as temperature, pressure, carrier gas (including gas species and gas flow), substrate, and evaporation period, which can be controlled.

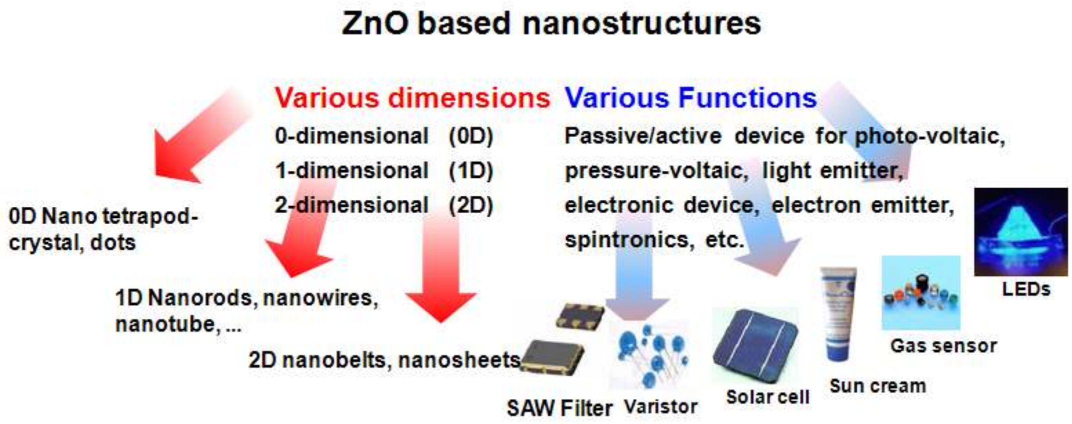

Fig. 1.6 ZnO nanostructure with various dimensions and functions

In the many applications of ZnO-based nanostructure, in fact, room temperature UV lasing in ZnO nanowires has been demonstrated [14]. UV light irradiation of the nanobelt diode of ZnO on air has been observed to result in a significant increase of the conductivity. The increase in the conductivity results from both photogeneration of electron-hole pairs as well as doping by UV-light-induced surface desorption. These processes could be observed by introducing a shutter between the light source and the ZnO nanobelt so that the flux of UV Photons could be turned on and off. As well as, it has demonstrated the manipulation of nanobelts by AFM and its potential for use in nanocantilevers [47].

ZnO exhibits sensitivity to various gas species, namely ethanol (C_2H_5OH), acetylene (C_2H_2), and carbon monoxide (CO), which makes it suitable for sensing applications. Moreover, its piezoelectric property (originating from its non-centrosymmetric structure) makes it suitable for electromechanical sensor or actuator applications [48]. Also, ZnO is biocompatible which makes it suitable for biomedical applications. Last but not least, ZnO is a chemically stable and environmentally friendly material. Consequently, there is considerable interest in studying ZnO in the form of powders, single crystals, thin films, or nanostructures.

1.5 Consideration to widen potentiality of ZnO-based nanotechnology

In the chapter 1.4, various ZnO nanostructures with diverse morphologies and their application are summarized. Although many applications of ZnO-based nanostructure have been discovered, there are several issues which should be investigated to widen the potentiality of ZnO based nanotechnology.

Nanotechnology can be understood as a technology of fabrication, measurement and application of nanostructures and nanomaterials. Many technologies have been explored to fabricate nanostructures and nanomaterials. These technical approaches can be divided into several ways; growth media (vapor phase growth, liquid phase growth, solid phase growth, and hybrid growth), form of products (nanoparticles, nanorods, nanowires, thin film, and nanostructured bulk materials), different fabrication and processing (top-down and bottom-up approaches, spontaneous and forced processes). Among those fabrication methods, more improved techniques will be required to obtain nanostructure with repeatability and controllability via simple and cheap process. Moreover, the small size and complexity of nanostructures make the development of new measurement technologies more challenging than ever. Measurements of physical properties of nanomaterials require extremely sensitive instrumentation, while the noise level must be kept very low. In short, an advanced technical development to level up the current nanotechnology in terms of fabrication, meaurement, and application should be accomplished to widen the application of ZnO based nanotechnology.

Note that to find out novel properties, tailoring physical properties of ZnO is also important, which can be achieved by doping and alloying process. In fact, doping and alloying in ZnO nanostructure offer a method to adjust the electrical, optical, and magnetic properties, which is an important technologies to broaden application. Table 1.3 shows structure and induced physical properties grown as a function of various dopants and growth system.

Table 1.3 Types of dopant for ZnO nanostructues, nanostructure and growth methods

Dopants	Stucture	Property	Method	Refs.
Mg	Rods	Band gap tuning	Metal-organic chemical vapor deposition (MOCVD)	[49]
	Particles		Solution-phase growth	[50]
Cd	Rods, wires	Band gap tuning	Thermal evaporation	[51]
	Wires		Thermal evaporation	[52]
Co, Ni	Wires	Ferromagnetic property	Hydrothermal method	[53]
Co	Wires		Electrodeposition	[54]
Al	Rods	n-type property	Thermal evaporation	[55]
	Cones		Pulsed laser deposition	[56]
Ga	Rods		Hydrothermal method	[57]
	Rods		Solution-phase growth	[58]
	Tips		MOCVD	[59]
In	Spirals		Thermal evaporation	[60]
	Belts		Thermal evaporation	[61]
P	Wires	p-type property	Chemical vapor deposition	[62]
As	Wires		MOCVD	[63]
	Wires		MOCVD	[64]

Many types of dopants for ZnO nanostructure have been introduced (Mg [49,50], Cd [51,52], Co [53,54], Ni [53], Al [55,56], Ga [57-59], In [60,61], P [62], and As

[63,64] and so on), however, there is still lack of information on the physical properties of nanostructure compared to bulk/thin film materials. Moreover, physical property of nanostructure is closely related with the morphology of nanostructure. Doping and alloying will induce not only physical property change but also morphological change. Therefore, synthesis of doped ZnO nanostructure with various morphologies using well-known impurities is required and systematic study on doped- and alloyed nanostructure should be accomplished.

n-type ZnO nanostructure

It is well known that nominally undoped ZnO reveals n-type conduction with a typical carrier concentration of 10^{17} cm^{-3} [65,66]. However, this value is inadequate for practical electronic applications, where a carrier concentration of 10^{18}-10^{20} cm^{-3} is required. Therefore, the doping of ZnO nanostructure to increase the carrier concentration or to decrease the resistivities is essential to realize nanoscale devices. Typical dopants that have been employed to increase the conductivity of ZnO group-III (B, Al, Ga, and In) and group-IV (Pb, Sn)-elements. However, group III-metal elements (M=Al, Ga, and In) in ZnO nanostructures are mainly used for n-type doping [55-61]. Ye and co-workers recently reported on the synthesis (by thermal evaporation methods) of quasi-aligned Al-doped ZnO nanorods on heavily doped n-type Si (111) substrates, and demonstrated their field emission properties [56]. In case of Ga, by introducing Ga into ZnO nanorods, the resistivities of about 4×10^{-3} Ωcm could be achieved [59] which is almost as low as values reached for transparent conduction oxide materials. When doping ZnO with In by vapor phase transporation method, where a mixture of ZnO and In_2O_3 powder is mostly used as the starting source material. Besides the unavoidable presence of the secondary phase of In_2O_3, the change of the morphology into various shapes such as nanobelts and hierarchical structure was observed [61]. So far, doping of n-type ZnO nanostructures is in progress, and morphology and conductivity control seem to difficult.

p-type ZnO nanostructure

Although recent advances in the fabrication techniques have enabled synthesis of ZnO nanostructure with good crystalline and optical qualities, p-type doping difficulty of ZnO, due to the low dopant solubility and self-compensating process, is still a major obstacle to the device application of ZnO nanowires. P-type ZnO films have been produced by N [67,68], P [69], and As [70] doping, ZnO nanowires doped with these elements have not realized yet. In the previous work [63] it was demonstrated that As could be uniformly diffused into ZnO nanowires by post-annealing, but its effect on the properties of ZnO nanowires was not investigated in detail. Also, p-type conduction was reported in ZnO nanowire arrays grown using P_2O_5 as dopant materials [62]. However, such p-type conduction was unstable and changed to n-type after 2 months of storage in air ambient. The instability is probably due to the larger atomic size of phosphorus than oxygen. Unlike the thin film counterpart, controlled doping in ZnO nanostructure remains a challenge to overcome.

On the one hand, recent efforts to dope ZnO nanowires with other elements were intended to achieve ferromagnetism [71] shape control [72] electric resistance control [73] or band gap engineering [74]. In short, among diverse dopant materials, approach using well-known dopants is suitable to solve lack of detail information in the nanostructure.

1.6 Importance of group III-metal impurity doping

As mentioned above, it is well known that ZnO is naturally an n-type semiconductor because of the presence of intrinsic defects, such as oxygen/Zn vacancies, oxygen/Zn interstitials, and the complex defects related to oxygen/Zn vacancies. Among intrinsic defects, dominant donor was either the O vacancy (V_O) or the Zn interstitial (Zn_i). In the year 2000, by Kohan *et al.* [75] showed theoretically both V_O and Zn_i have high formation energies in n-type ZnO. Furthermore, they are deep, not shallow, donors. They concluded that neither V_O nor Zn_i would exist in measurable quantities, and that even if one or the other were present, its ionization energy would be too high to produce free electrons. In contrast, other theoretical analyses have concluded that Zn_i is actually a shallow donor, rather than deep [76,77]. However, the high formation energy of Zn_i mentioned earlier would still limit its ability to influence the conductivity of n-type material. After Kohan *et al.* showed that V_O and Zn_i were not good explanations for the n-type nature of ZnO. He argued that H is always a donor in ZnO, that it is easily ionized, and that it has a low enough formation energy to be abundant [78]. This proposal has been subjected to testing, because H-containing, high-quality, bulk ZnO, grown by a seeded chemical vapor transport (SCVT) technique, has been commercially available for the last few years [79]. In general, these tests have confirmed that a shallow donor due to H exists in SCVT ZnO [80,81] and can contribute significantly to its conductivity. However, some of the group III elements, such as Al, Ga and In, are also shallow donors, and are more abundant than H in many cases. Finally, very recent evidence has emerged that even native defects can make important donors, but as complexes, not isolated entities. Therefore I recommend to adopt group-III metal elements as the effective method to control n-type ZnO nanostructure.

1.7 Proposal of this study

The studies of group III-metal impurity (M=Al, Ga, and In) doped ZnO nanostructures have been mainly performed in terms of diverse morphologies using various growth methods. Although several previous studies on M-doped nanostructures have been progressed, there are some problems to overcome. In fact, it is difficult to compare the physical properties of M-doped ZnO nanostructures because they were grown under different growth condition such as growth methods, growth temperature, type of carrier gas, and with/without catalyst. Therefore, the growth of nanostructures under consistent growth condition should be required.

Second, most of doped ZnO nanostructures are based on wire-type. There are few reports on systematic M-doped nanostructure grown by changing growth parameters. Thus, the investigation on doped ZnO nanostructure with various dimensions as well as the control of growth parameters as mentioned above is inevitably important issue.

Third, study on the physical properties of M-doped ZnO nanostructures is still insufficient due to a lack of systematic research as previously stated. The purpose of this study is the growth and characterization of group III-metal impurity doped ZnO nanostructure for the application to nanostructures, following issues are addressed.

1) Growth and characterization of dispersive 0-dimensional (0D) M-doped (M=Al, Ga, and In) ZnO nanostructure

2) Growth and characterization of integrated 1-dimensional (1D) M-doped (M=Al, Ga, and In) ZnO nanostructure

3) Discussion on the device performance of field emission device made by the doped ZnO nanostructure with diverse dimensions

1.8 Outline of this thesis

The thesis consists of 6 chapters and appendix. Details are summarized as follows.

In the chapter 1, introduction of nanotechnology, physical properties of ZnO, importance of group-III metal impurities doped ZnO nanostructures, and the purpose of this study are described.

In the chapter 2, growth method, characteristic of dimensions, and various analysis principles are explained.

In the chapter 3, growth and characterization of dispersive 0D ZnO nanostructures are described. Prior to the doping, growth condition for pure ZnO nanostructures was determinated. Group-III metal impurities like as Al, Ga, and In doped nanostructures were grown under the consistent growth condition. The morphological structural, optical, and electrical properties originated from impurity-doping are investigated.

In the chapter 4, growth and characterization of integrated 1D ZnO nanostructures are introduced. Under the consistent growth condition, impurity-doped ZnO nanostructures are synthesized. Physical property variation was investigated in terms of structural, optical, and electrical properties.

In the chapter 5, relationship between physical property of nanostructure and device performance is discussed. Field emission devices were fabricated using the group III-metal impurity doped ZnO nanostructures. The variation of the conductivity and structural properties induced by doping was prospected and experimental results are discussed.

Finally, the results found from this dissertation are summarized and concluded in the chapter 6.

References

[1] F. Rosei, J. Phys.: Condens. Matter 16 S1373 (2004)

[2] A.Shew, Presentation at the International Congress of Nanotechnology, October 31, 2006 - November 2, 2006

[3] Mihail C et al, National Science Foundation, "Societal Implications of Nanoscience and Nanotechnology", NSET Work shop report, March 2001

[4] W.O. Miligan and R.H. Morriss, J. Am. Chem. Soc 86 3461 (1964)

[5] S. Iijima, Nature 354 56 (1991)

[6] C.B. Murray, D.J. Norris, and M.G. Bawendi, J. Am. Chem. Soc. 115 8706 (1993)

[7] Z.R. Dai, Z.W. Pan, Z.L. Wang, Funct. Adv. Mater. 13 9 (2003)

[8] Z.L. Wang, Z.C. Kang, Functional and Smart Materials, Plenum, New York 1998.

[9] C. Kingshirn, Phys. Stat. sol. (b) 244 3027 (2007)

[10] Ü. Özgür,Y.I. Alivov, C. Liu et al, J. Appl. Phys. 98 041301 (2005)

[11] R. Janisch, P. Gopal, N. A. Spaldin, J. Phys. Condens. Matter 17 R657 (2005)

[12] Z.W. Pan, Z.R Dai, Science 291 1947 (2001)

[13] B.D. Bao, Y.F. Chen, Appl. Phys. Lett. 81 757 (2002)

[14] M.H. Huang, S. Mao, et al, Science 292 1897 (2001)

[15] M.H. Huang, Y. Wu, H. Feick et al, Adv. Mater. 13 113 (2001)

[16] Y. Dai, Y. Zhang, Q.K. Li et al, Chem. Phys. Lett. 358 83 (2002)

[17] J.Y. Li, X.L. Chen, H. Li et al, J. Cryst. Growth 233 5 (2001)

[18] W.I. Park, D.H. Kim. S.W. Jung et al, Appl. Phys. Lett. 80 4232 (2002)

[19] J.J. Wu. S.C. Liu, Adv. Mater. 14 215 (2002)

[20] C. Xu, G. Xu, Y. Liu et al, Solid State Commun. 122 175 (2002)

[21] L. Guo, J.X. Cheng, X.Y. Li et al, Mater. Sci. Eng. 16 123 (2001)

[22] P.D. Yang et al, J. Mater. Res. 12 2981 (1997)

[23] Y. Yin, G. Zhang, Y. Xia, Adv. Funct. Mater. 12 293 (2002)

[24] C. Tang, Y. Bando et al, J. Phys. Chem. B, 106 7449 (2002)

[25] Y. Li, Y. Bando, Chem. Phys. Lett. 359 141 (2002)

[26] Y. Liu, C. Yin, W. Wang et al, J. Mater. Sci. Lett. 21 137 (2002)

[27] X. Wang, Y. Li, J. Am. Chem. Soc. 124 2880 (2002)

[28] W.Wang, C. Xu, G. Wang, Y. Liu et al, Adv. Mater. 14 837 (2002)

[29] B.C. Satishkumar, A. Govindaraj et al, J. Mater. Res. 12 604 (1997)

[30] Z.R. Dai, Z.W. Pan et al, J. Phys. Chem. B 106 902 (2002)

[31] J. Zhang, L, Zhang, Solid State Commun. 122 293 (2002)

[32] Y.C. Choi, W.S. Kim, W.S. Park et al, Adv. Mater. 12 746 (2000)

[33] G. Gundiah, A. Govindaraj et al, Chem. Phys. Lett. 351 189 (2001)

[34] X.S. Peng, Y.W. Wang, J. Zhang et al, Appl. Phys. A 74 437 (2002)

[35] C. Liang, G. Meng, Y. Lei et al, Adv. Mater. 13 1330 (2001)

[36] O. Dulub, L. A. Boatner, U. Diebold, Surf. Sci. 519 201 (2002)

[37] E. Kisi and M.M. Elcombe, Acta Crystallogr., Sec. C: Cryst. Struct. Commun. C45 1867 (1989)

[38] J. E. Jaffe, J. A. Snyder, Z. Lin, A. C. Hess, Phys. Rev. B 62 1660 (2000)

[39] U. Rossler, Phys. Rev. 184 733 (1969)

[40] M. Usuda, N. Hamada, T. Kotani, M. V. Schilfgaarde, Phys. Rev. B 66 125101 (2002)

[41] I. Ivanov, J. Pollmann, Phys. Rev. B 24 7275 (1981)

[42] T.W. Kim, T. Kawazoe, T. Sekiguchi et al, Appl. Phys. Lett. 84 3358 (2004)

[43] Q. Wan, K. Yu, T.H. Wang, C.L. Lin, Appl. Phys. Lett. 83 2253 (2003)

[44] Y.B. Li, Y. Bando, T. Sato et al, Appl. Phys. Lett. 81 144 (2002)

[45] L. Dloczik, R. Engelhardt, K. Ernst et al, Appl. Phys. Lett. 78 3687 (2001)

[46] J.Q. Hu, Y. Bando, J.H. Zhan et al, Appl. Phys. Lett. 83 4414 (2003)

[47] E. Comini, G. Faglia et al, Appl. Phys. Lett. 91 1869 (2002)

[48] A.B. Djurisic et al, Small, 2 944 (2006)

[49] M. Kim, Y.J. Hong, J.Y. Yoo et al, Phys. stat. sol. 2 197 (2008)

[50] H.M. Xiong, D.G. Shchukin et al, Nanomaterials, 48 2727 (2009)

[51] F. Wang, Z. Ye, D. Ma et al, J. Cryst. Growth 283 373 (2005)

[52] Q.H. Li, Q. Wan, Y.G. Wang et al, Appl. Phys. Lett. 86 263101 (2005)

[53] J.B. Cui and U.J. Gibson, Appl. Phys. Lett. 87 133108 (2005)

[54] J. Cui and U.Gibson, Phys. Rev. B 74 045416 (2006)

[55] H. Tamng, L. Zhu, H. He et al, J. Phys. D: Appl. Phys. 39 2696 (2006)

[56] S. Ye, E.A. Katherine et al, Nanotech. 18 495601 (2007)

[57] A.Escobedo-Morales and U. Pal, Appl. Phys. Lett. 93 193120 (2008)

[58] H. Wang. S.H. Baek, J.J. Song et al, Nanotech. 19 075607 (2008)

[59] J. Zhong et al, Appl. Phys. Lett. 83 3401 (2003)

[60] H. Gao, H. Ji, X. Zhang et al, J. Vac. Sci. Technol. B 26(2) 585 (2008)

[61] J Jie, G Wang, X Han, Q Yu, Y Liao, Chem. Phys. Lett. 387 466 (2004)

[62] B. Xiang, P. Wangm X. Zhang et al, Nano Lett. 7 323 (2007)

[63] W. Lee, M.C. Jeong, S.W. Joo et al, Nanotech. 16 764 (2005)

[64] W. Lee, M.C. Jeong, J.N. Nyoung, Appl. Phys. Lett. 85 6167 (2004)

[65] P. Wagner and R. Helbig, J. Phys. Chem. Solids 35 327 (1974)

[66] S. Bethke, H. Pan, and B. Wessels, Appl. Phys. Lett. 52 138 (1988)

[67] D.C. Look, D.C. Reynolds et al, Appl. Phys. Lett. 81 1830 (2002)

[68] N.Y. Garces, L. Wang, N.C. Giles et al, J. Appl. Phys. 94 519 (2003)

[69] T. Aoki, Y. Hatanaka, D.C. Look et al, Appl. Phys. Lett. 76 3257 (2000)

[70] Y.R. Ryu, T.S. Lee et al, Appl. Phys. Lett. 83 87 (2003)

[71] K.I.R. MFrazier, Y.W. Heo et al, J. Vac. Sci. Technol. B 21 1476 (2003)

[72] D.W. Zeng , C.S. Xie, B.J. Zhu et al, J. Cryst. Growth 266 511 (2004)

[73] Q. Wan, Q.H. Li, Y. Chen et al, Appl. Phys. Lett. 84 3085 (2004)

[74] B.Y. Geng et al, Appl. Phys. Lett. 82 4791 (2003)

[75] A.F. Kohan, G. Ceder, D. Morgan et al, Phys. Rev. B: Condens. Matter Mater. Phys. 61 15019 (2000)

[76] S.B. Zhang, S.-H. Wei, and A. Zunger, Phys. Rev. B: Condens. Matter Mater. Phys. 63 075205 (2001)

[77] F. Oba, S.R. Nishitani, S. Isotani, H. Adachi, and I. Tanaka, J. Appl. Phys. 90 824 (2001)

[78] C .G. Van de Walle, Phys. Rev. Lett. 85 1012 (2000)

[79] D.C. Look, D.C. Reynolds, J.R. Sizelove, R.L. Jones, C.W. Litton, G. Cantwell, and W.C. Harsch, Solid State Commun. 105 399 (1998)

[80] S.F.J. Cox et al., Phys. Rev. Lett. 86 2601 (2001)

[81] D.M. Hofmann, A. Hofstaetter et al, Phys. Rev. Lett. 88 045504 (2001)

[82] D.C. Look, G.C. Farlowet al, K. Nordlund, Phys. Rev. Lett. 95 225502 (2005)

Chapter 2. Experimental

2.1 Growth processes

2.1.1 Growth system

Various growth methods have been introduced to growth diverse oxide-based nanostructures in the Table 1.1. ZnO has probably the richest variety of different nanostructures. Its range includes highly ordered nanowire arrays, tower-like structures, nanorods, nanobelts, nanosprings, nanocombs, and nanorings. Table 2.1 summarizes some of the studies on growth method and the resulting structures of ZnO. Among the many growth methods, thermal evaporation by horizontal tube furnace is widely used for the growth of nanostructures (Fig. 2.1). The system has many merits for this experiments. Most of all, it is very easy to control the growth temperature and carrier gas flow, hence nanostructures with various dimension can be easily obtained.

I have reported on the shape control of ZnO nanostructures. As mentioned in the previous report [1], the flow rate of carrier gas was fixed to 600 sccm, however, various reaction tubes with different diameters (8 mm, 22 mm, 31 mm, 39 mm, and 50 mm) were prepared to control the carrier gas flux. Also, The growth temperature was controlled from 600 ^{o}C to 900 ^{o}C. Clusters with irregular shapes and diverse sizes (5−20 μm) were formed under the relatively low growth temperature (700−800 ^{o}C) and high carrier gas flux ($\text{flux}_{gas} > 10$ cc/mm^{2}min), While, in the intermediate carrier gas flux ($1 < \text{flux}_{gas} < 10$ cc/mm^{2}min) region, rod or wire types were exhibited. The diameter of typical rod is as large as 100− 200 nm with the length of 5−10 μm. Tetrapods are only obtained at high temperature (800−900 ^{o}C) and low carrier gas flux ($\text{flux}_{gas} < 1$ cc/mm^{2}min) region. Tetrapods have considerably uniform shape with 100 nm thick and 1−1.5 μm long legs without second phase.

From these results one can find that not only the growth temperature but also carrier gas flux has a great influence on the formation of ZnO nanostructures [2,3].

Table 2.1 Summary on growth methods of ZnO nanostructures

Growth method	Morphology	Focused parameter	Refs.
Chemical vapor deposition (CVD)	nanowires	Au catalyst	[4]
	nanowires	Partial oxygen pressure	[5,6]
	nanowires dendritic structures comb-like structures nanosheets	Partial oxygen pressure	[7]
Pulsed laser deposition (PLD)	nanorods	Catalyst free	[8]
	nanocolumns	ZnO vapor pressure	[9]
Thermal evaporation	porous membranes nanowires nanorods nanoneedles nanotetrapods	Heating ratio, Catalyst free	[10]
	nanobelts	Catalyst free	[11]
	nanorings, nanobows	Catalyst free	[12]
Aqueous solution growth	nanorods	Substrate, seed layer	[13]
	nanowires	Seed layer	[14]
	nanowires tower-like structures flower-like structures tube-like structures	Reactants, Growth time, Growth temperature Substrate	[15]
Electrodeposition	nanocolumns	Current density Deposition time Bath temperature	[16,17]

2.1.2 Mixed source method

In this experiments, metal powder-type sources are used for vapor phase transportation (VPT) growth, which is easier and cheaper to grow of nanostructure without equipment modification. For doping, not only how to mix the dopant materials but also how to control doping range are important. Mixed source method, to mix in a function of different ratio between host and dopant materials, is applied for this experiment. By previous results for doped nanostructures, it was suggested to diffuse the dopant element by using substrate, like as InP [18], GaAs [19] for p-type and ITO [20] for n-type. However, there is always a limit temperature, which is not suitable for growth of nanostructure with diverse dimensions. Note that ITO substrate is destroyed above temperature of 650 °C. The 0-dimensional (0D) nanostructures has minimum growth temperature above 700 °C. Hence mixed source method was selected to control doping concentration in a wide range for various morphologies [21].

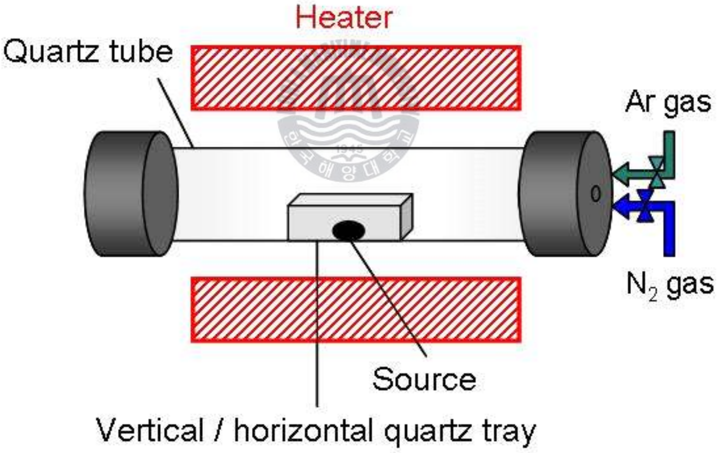

Fig. 2.1 Schematic system of horizontal reaction furnace

2.2 Two kinds of doped nanostructure with different dimensions

Nanostructures can be defined as a system in which at least one dimension is ≤ 100 nm; that is, reducing 1, 2 or 3 dimensions (D) of a bulk material to the nanometer scale produces nanometer thick 2D layers (sheets), 1D nanowires (rods, tubes), or 0D nanoclusters (particles), respectively. Interest in nanometer scale structures has been driven by fascinating questions and the potential to impact basic science and technology [22]. In this thesis, dispersive 0D and integrated 1D nanostructures were synthesized as shown in the Fig. 2.2.

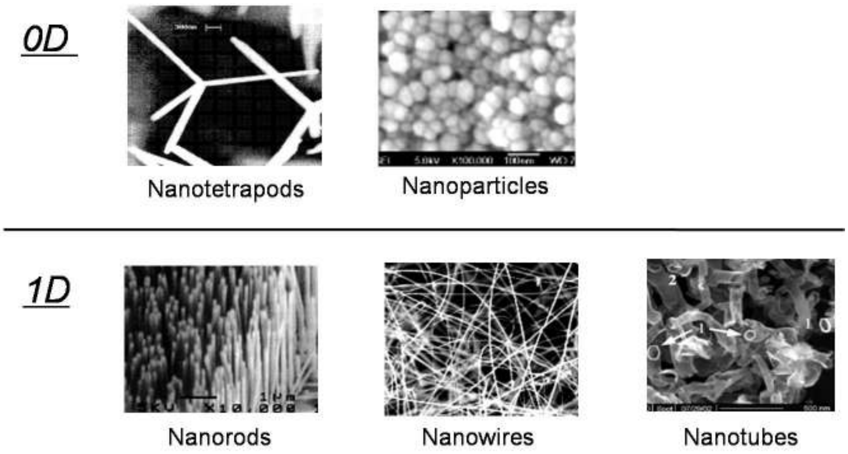

Fig. 2.2 Various nanostructures as a function of dimension

KOREA MARITIME UNIVERSITY 1945 한국해양대학교

Among them, nanotetrapods and nanorods were selected for dispersive 0D and integrated 1D structure, respectively. The growth of 0D nanotetrapod is a consequence of direct reaction between source materials. A powder-type products are obtained via condensation, agglomeration, and crystallization processes from source materials of gas-phase. Compared to other structures, synthesis of the 0D structure is simple because of no need of substrate or catalyst. Moreover, 0D nanostructure has morphological repeatability and diverse application.

The 1D nanorods are usually grown on a substrate. So it requires careful control of growth parameters. However, 1D nanorods provides vertically aligned nanostructures with controllability which is suitable for application to the various high-integrated devices. In this thesis, the growth of nanostructures with different dimension and physical properties of doped ZnO nanostructures as a function of dimension are investigated.

2.3 Characterization

2.3.1 Field emission scanning electron microscopy

Scanning electron microscopy (SEM) has become one of the most versatile and useful method for direct imaging, characterization, and studying of solid surfaces [23]. As the electrons penetrate the surface, a number of interactions occur that can result in the emission of electrons or photons from (or through) the surface.

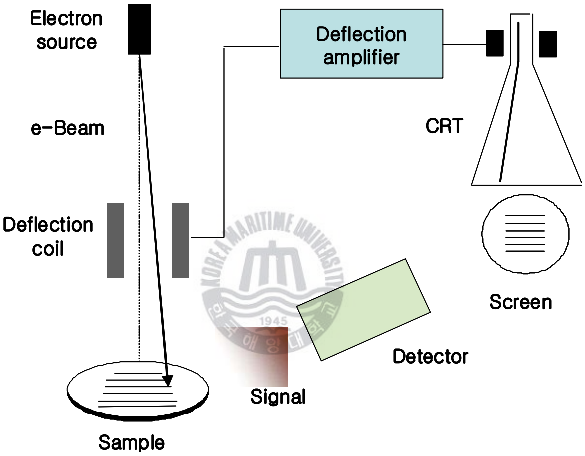

Fig. 2.3 Schematic system of an SEM

Appropriate detectors can collect a reasonable fraction of the electrons emitted, and the output can be used to modulate the brightness of a cathode ray tube (CRT) whose x- and y- inputs are driven in synchronism with the x-y voltages rastering the electron beam. In the way an image is produced on the CRT. When the primary electrons collide with atoms of a solid surface in the specimen the electrons take part in various interactions. The principle images produced in the SEM are of three types; secondary electron images, backscattering electron images, and elemental

X-ray maps. Secondary and backscattering electrons are conventionally separated according to their energies. They are produced by different mechanisms. When a high-energy primary electron interacts with an atom, it undergoes either inelastic scattering with atomic electrons or elastic scattering with the atomic nucleus. In an inelastic collision with an electron, some amount of energy is transferred to the other electron. If the energy transfer is very small, the emitted electron will probably not have enough energy to exit the surface. If the transferred energy exceeds the work function of the material, the emitted electron can exit the solid. When the energy of the emitted electron is less than about 50 eV by convention, it is referred to as a secondary electron (SE), or simply a secondary. Most of the emitted secondaries are produced much deeper in the material suffer additional inelastic collisions, which lower their energy and trap them in the interior of the solid.

Higher energy electrons are primary electrons that have been scattered without loss of kinetic energy (i.e.,elastically) by the nucleus of an atom, although these collisions may occur after the primary electron has already lost some of its energy to inelastic scattering. Backscattered electrons (BSEs) are considered to be the electrons that exit the specimen with an energy greater then 50 eV, including Auger electrons. However, most BSEs have energies comparable to the energy of the primary beam. The higher the atomic number of a material, the more likely it is that backscattering will occur. Thus a beam passes from a low-Z (atomic number) to a high-Z area, the signal due to backscattering, and consequently the image brightness, will increase. There is a built in contrast caused by elemental differences. It is usual to define the primary beam current i_0, the BSE current i_{BSE}, the SE current i_{SE}, and the sample current transmitted through the specimen to ground i_{SC}, such that the Kirchoff current law holds:

$$i_0 = i_{BSE} + i_{SE} + i_{SC}$$

These signals can be used to form complementary images. As the beam current is increased, each of these currents will also increase. The backscattered electron yield (η) and the secondary electron yield (δ), which refer to the number of backscattered and secondary electrons emitted per incident electron, respectively, are defined by the relationships.

$$\delta = \frac{i_{SE}}{i_0}, \quad \eta = \frac{i_{BSE}}{i_0} \ ,$$

In most currently available SEMs, the energy of the primary electron beam can range from a few hundred eV up to 30 keV. The values of δ and η will change over this range, however, yielding micrographs that may vary in appearance and information content as the energy of the primary beam is changed.

2.3.2 Energy dispersive X-ray spectroscopy

KOREA MARITIME UNIVERSITY 1945 한국해양대학교

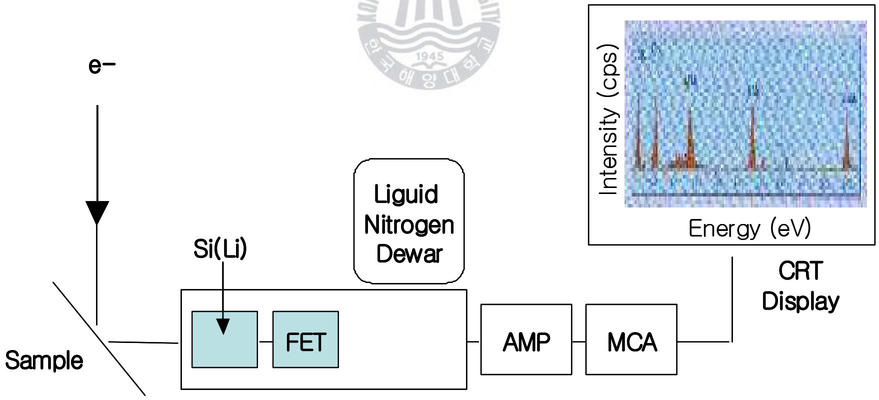

Fig. 2.4 Schematic system of an EDX

Energy-dispersive X-ray spectroscopy (EDX) has been used for quality control and test analysis in many industries including [23]; computers, semiconductors, metals, cement, paper, and polymers. EDX has been used in medicine in the analysis of blood, tissues, bones, and organs; in pollution control, for asbestos identification; in field studies including ore prospecting, archeology, and oceanography; for identification and forgery detection in the fine arts; and for forensic analysis in law enforcement. With a radioactive source, an EDX system is easily portable and can be used in the field more easily than other spectroscopy techniques. The main advantages of EDX are its speed of data collection; the detector's efficiency (both analytical and geometrical); the ease of use; its portability; and the relative ease of interfacing to existing equipment.

X-rays are produced as a result of the ionization of an atom by high-energy radiation wherein an inner shell electron is removed. To return the ionized atom to its ground state, an electron from a higher energy outer shell fills the vacant inner shell and, in the process, releases an amount of energy equal to the potential energy difference between the two shells. This excess energy, which is unique for every atomic transition, will be emitted by the atom either as an x-ray photon or will be self-absorbed and emitted as an Auger electron.

As shown in the Fig 2.4, the heart of the EDX is a diode made from a silicon crystal with lithium atoms diffused, of drifted, from and end into the matrix. The lithium atoms are used to compensate the relatively low concentration of grown in impurity atoms by neutralizing them. In the diffusion process, the central core of the silicon will become intrinsic, but the end away from the lithium will remain p-type and the lithium end will be n-type. The result is a p-i-n diode. When an X-ray photon enters the intrinsic region of the detector through the p-type end, there is a high probability that it will ionize a silicon atom through the photoelectric effect. This results in an X-ray or an Auger electron, which in turn produces a number of electron-hole pairs in the Si (Li). Both charge carriers move freely through the lattice and are drawn to the detector contacts under the action of the applied bias field to produce a signal at the gate of a specially designed field effect transistor mounted directly behind the detector crystal. The transistor forms the input stage of a low-noise charge-sensitive preamplifier located on the detector housing. The output from the preamplifier is fed to the main amplifier, where the signal is finally amplified to a level that can be processed by the analog-to-digital converter (ADC) of the multichannel analyzer (MCA). The height of the amplifier output pulse is proportional to the input preamplifier pulse, and hence is proportional to the X-ray source.

2.3.3 Auger electron spectroscopy

Auger electron spectroscopy (AES) has emerged as one of the most widely used analytical techniques for obtaining the chemical composition of solid surfaces. The basic advantages of this technique are its high sensitivity for chemical analysis in the 5 to 20 Å region near the surface, a rapid data acquisition speed, its ability to detect all elements above helium, and its capability of high-spatial resolution.

When an electron is ejected from an inner shell of an atom the resultant vacancy can be filled by either a radiative (X-ray) or nonradiative (Auger) process. In AES the atomic core levels are ionized by the incident electron beam and the resulting Auger electrons are detected with an electron spectrometer. These electrons form small peaks in the total energy distribution function, N(E). The Auger process can be understood by considering the ionization process of an isolated atom under electron bombardment. The incident electron with sufficient primary energy, E_p, ionizes the core level, such as a K level. The vacancy thus produced is immediately filled by another electron from L1.

This process is shown in Fig. 2.5. The energy (E_K - E_{L1}) released from this transition can be transferred to another electron, as in the L_2 level. This electron is ejected from the atom as an Auger electron. The Auger electron will have energy given by

$$E = E_K - E_{L1} - E_{L2}$$

This excitation process is denoted as a KL_1L_2 Auger transition. It is obvious that at least two energy states and three electrons must take part in an Auger process. Therefore, H and He atoms cannot give rise to Auger electrons. Several transitions (KL_1L_1, KL_1L_2, LM_1M_2, etc.) can occur with various transition probabilities. The Auger electron energies are characteristic of the target material and independent of the incident beam energy.

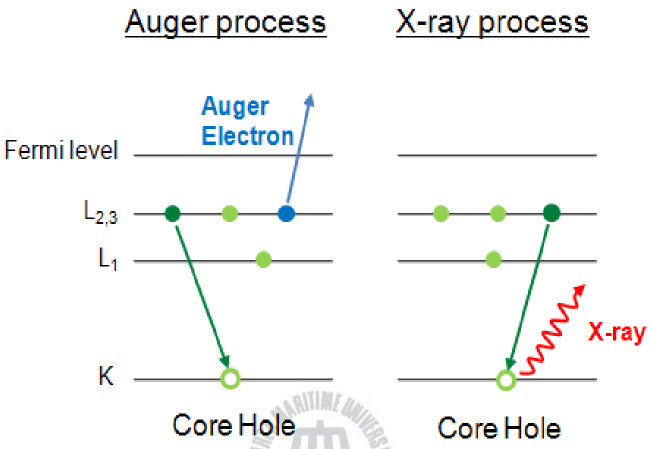

Fig. 2.5 Auger process

2.3.4 Hard X-ray photoemission spectroscopy

Hard X-ray photoemission spectroscopy (HXPES) with high-resolution, high hroughput and large photoelectron attenuation length has been developed at SPring-8 utilizing high brilliant undulator X-rays. This enhanced versatility of the photoemission spectroscopy, enabling to apply to laboratory prepared thin films and nano-structured samples of advanced materials.

Generally, X-ray Photoelectron Spectroscopy known as XPS or ESCA (Electron Spectroscopy for Chemical Analysis) was developed in the mid 1960s by K. Siegbahn and his research group. The basic mechanism behind an XPS instrument is illustrated in the Fig. 2.6, where photons of a specific energy are used to excite the electronic states of atoms below the surface of the sample.

Electrons ejected from the surface are energy filtered via a hemispherical analyser (HSA) before the intensity for a defined energy is recorded by a detector. Since core level electrons in solid-state atoms are quantized, the resulting energy spectra exhibit resonance peaks characteristic of the electronic structure for atoms at the sample surface. While the x-rays may penetrate deep into the sample, the escape depth of the ejected electrons is limited. That is, for energies around 1400 eV, ejected electrons from depths greater than 10 nm have a low probability of leaving the surface without undergoing an energy loss event, and therefore contribute to the background signal rather than well defined primary photoelectric peaks.

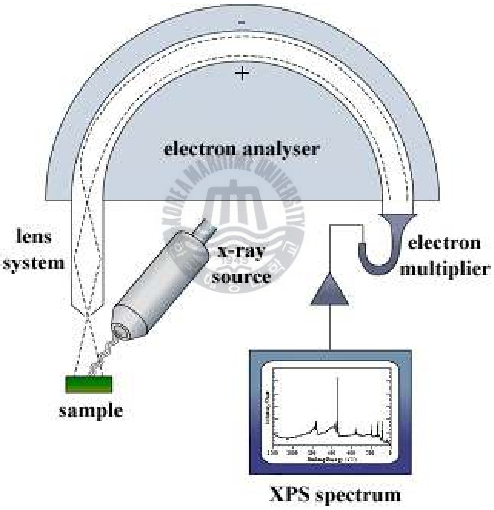

Fig. 2.6 Schematic system of an XPS instrument

I performed at a planar undulator beam line, BL15XU, of Spring-8. X-rays monochromated at 5.95 keV with a Si(111) double crystal were injected onto samples mounted in an analyzer chamber. A channel-cut monochromator was placed before injection to the samples, to reduce the energy bandwidth. The vacuum of the analyzer chamber was ~10^{-5} Pa. The large escape depth at high energy (above 5 nm at 5.95 keV) allows determination of bulk electronic states with high precision. Photoelectrons were collected by a Gammadata Sciencta SES2002 electron analyzer system, which was modified to accommodate higher photoelectron kinetic energies up to 6 keV. The instrumental energy resolution, including X-ray bandwidth, was estimated to be 250 meV at 300 K by the Fermi energy (E_F) of an Au plate.

2.3.5 Powder X-ray diffraction

X-ray diffraction (XRD) is a powerful technique used to uniquely identify the crystalline phases present in materials and to measure the structural properties (strain state, grain size, epitaxy, phase composition, preferred orientation, and defect structures) of these phases. XRD is also used to determine the thickness of thin films and mutilayers, and atomic arrangements in amorphous materials and at interfaces [24]. The fundamental principles of XRD are discussed.

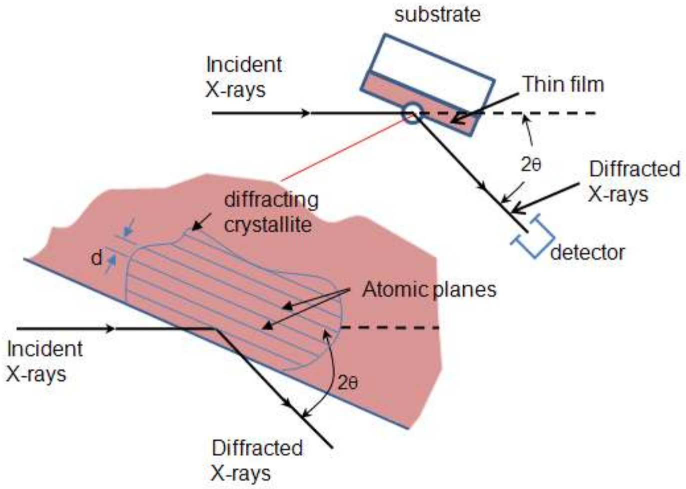

Fig. 2.7 Basic features of a typical XRD experiment

Fig. 2.7 shows the basic features of an XRD measurement, where the diffraction angle 2Θ is the angle between the incident and diffracted x-rays. In a typical experiment, the diffracted intensity is measured as a function of 2Θ and the orientation of the specimen, which yields the diffraction pattern. The X-ray wavelength λ is typically 0.7-2 Å, which corresponds to X-ray energy (E=12.4 keV/λ) of 6-17 keV.

As mentioned above, X-rays are electromagnetic radiation with typical photon energies. For diffraction applications, only short wavelength x-rays (hard x-rays) in the range of a few angstrom to 0.1 angstrom (1 keV - 120 keV) are used. Because the wavelength of x-rays is comparable to the size of atoms, they are ideally suited for probing the structural arrangement of atoms and molecules in a wide range of materials.

The energetic x-rays can penetrate deep into the materials and provide information about the bulk structure. X-rays are produced generally by either x-ray tubes or synchrotron radiation. In a x-ray tube, which is the primary x-ray source used in laboratory x-ray instruments, x-rays are generated when a focused electron beam accelerated across a high voltage field bombards a stationary or rotating solid target. As electrons collide with atoms in the target and slow down, a continuous spectrum of x-rays are emitted, which are termed Bremsstrahlung radiation. The high energy electrons also eject inner shell electrons in atoms through the ionization process. When a free electron fills the shell, a x-ray photon with energy characteristic of the target material is emitted. Common targets used in x-ray tubes include Cu and Mo, which emit 8 keV and 14 keV x-rays with corresponding wavelengths of 1.54 Å and 0.8 Å, respectively.

Powder x-ray diffraction (P-XRD) is the most widely used x-ray diffraction technique for characterizing materials. As the name suggests, the sample is usually in a powdery form, consisting of fine grains of single crystalline material to be studied. The technique is used also widely for studying particles in liquid suspensions or polycrystalline solids (bulk or thin film materials).

The term 'powder' really means that the crystalline domains are randomly oriented in the sample. Therefore when the 2-D diffraction pattern is recorded, it shows concentric rings of scattering peaks corresponding to the various *d* spacings in the crystal lattice. The positions and the intensities of the peaks are used for identifying the underlying structure (or phase) of the material. For example, the diffraction lines of graphite would be different from diamond even though they both are made of carbon atoms. This phase identification is important because the material properties are highly dependent on structure (just think of graphite and diamond).

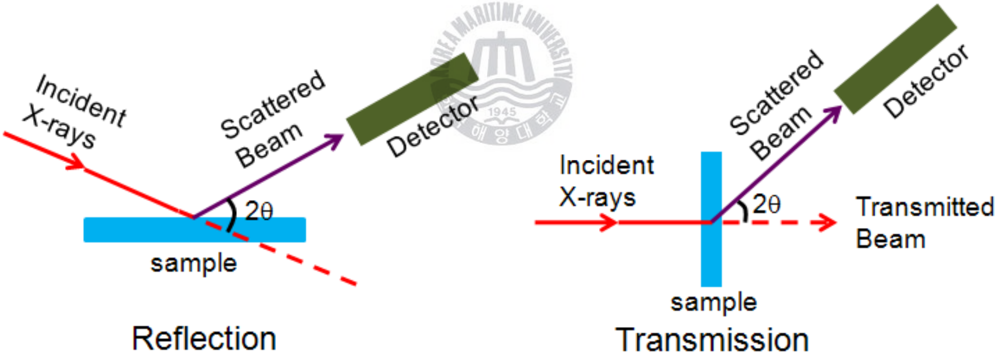

Fig. 2.8 Powder XRD method by transmission or reflection geometry

Powder diffraction data can be collected using either transmission or reflection geometry, as shown in the Fig. 2.8. Because the particles in the powder sample are randomly oriented, these two methods will yield the same data. In the MRL x-ray facility, powder diffraction data are measured using the Philips XPERT MPD diffractometer, which measures data in reflection mode and is used mostly with solid samples, or the custom built 4-circle diffractometer, which operates in transmission mode and is more suitable for liquid phase samples.

2.3.6 Photoluminescence

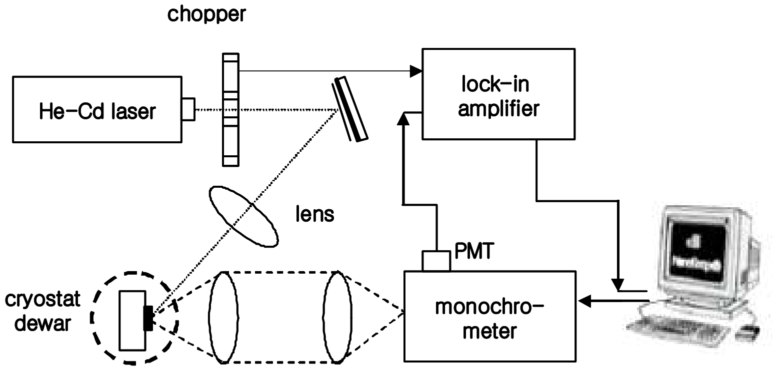

Fig. 2.9 Schematic layout of the photoluminescence system

Photoluminescence (PL) is a well-established and widely practiced tool for materials analysis due to its sensitivity, simplicity, and low cost. In the context of surface and microanalysis, PL is applied mostly qualitatively or semiquantitatively to exploit the correlation between the structure and composition of a material system and its electronic state and their lifetimes, and to identify the presence and type of trace chemicals, impurities, and defects [24]. PL systems are largely made up the source of light for excitation (laser), sample holder (or cryostat to measure at low temperature), including optics for focusing the incident light and collecting the luminescence, filter, a double or a triple monochrometer, the optical detector such as photomultiplier tube or CCD or photodiode arrays, and recoding equipments. The experimental setup for the PL measurements used in this study is schematically shown in the Fig 2.9.

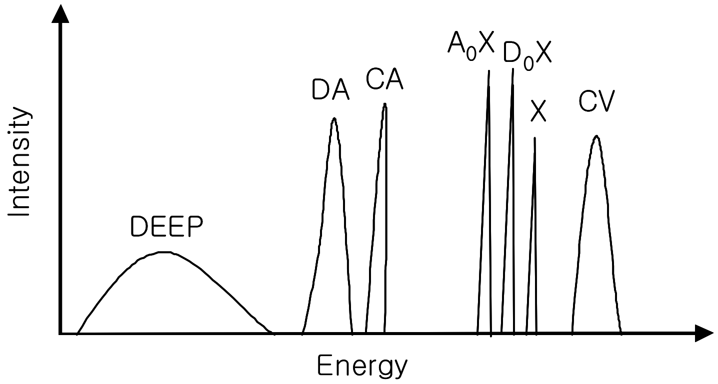

Fig. 2.10 Major features of near band edge photoluminescence spectra

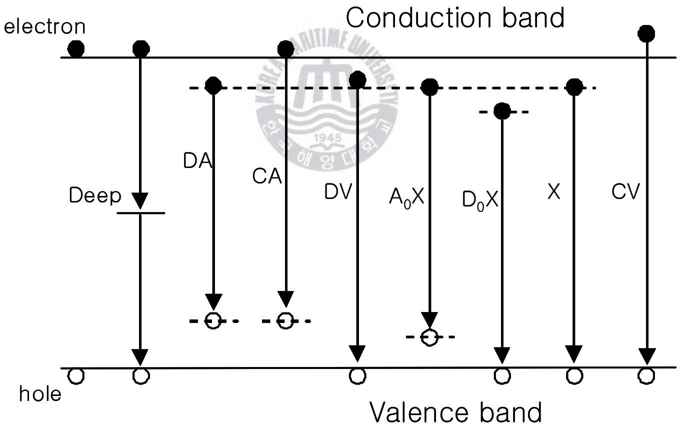

Fig. 2.11 Recombination processes of photoluminescence spectra

In PL, a material gains energy by absorbing light at some wavelength by promoting an electron forma low to a higher energy level. This may be described as making a transition form the ground state to an excited state of a semiconductor crystal (electron-hole creation), The system then undergoes a nonradiative internal relaxation involving interaction with crystalline or molecular vibrational and rotational modes, and the excited electron moves to a more stable excited level. The major features that appear in a PL spectrum under low excitation are schematically shown in the Fig.2.10.

The above structures are usually observed; transition from the conduction band to the valence band (CV), free exciton (X), excitons bound to neutral donors and acceptors (D_0X and A_0X), transition from a donor to the valence band (DV), transition from the conduction band to an acceptor (CA), transition from a donor to an acceptor (DA), radiative transition at deep states in the forbidden energy gap ((Deep), respectively. All these recombination processes are schematically represented in the Fig. 2.11.

The radiative transition from the conduction band to the valence band is usually observed at temperatures higher than the dissociation energy of exciton (~100 K). The line shape is structureless and is given by an effective density of state term multiplied by the Boltzmann filling factor.

$$I_{CV} \propto \sqrt{hv - E_g}\, \exp(-\frac{hv - E_g}{K_B T})$$

E_g is energy gap of the semiconductor, h is the photon energy of the luminescence and $k_B T$ has its usual meaning. It can be seen from above equation that the low energy edge of the structure gives the energy gap of the semiconductor and the temperature of carriers can be obtained from the slope of the high-energy part.

Recombination of electrons and holes through free excitons (X) takes place in a high-purity sample at low temperature. Bound excitonic emissions emerge in a near-gap luminescence spectrum as the donor or acceptor concentration is increased from a low level. A prominent type of recombination process involves the annihilation of an exciton bound to either of these species in their neutral charge state.

The recombination process from the conduction band to an acceptor state (CA) is free- to bound transition. As shown in the Fig. 2.11, the low energy threshold of this CA transition can be described as in above equation for CV transition, but E_g must be replaced by E_g-E_A, where E_A is the position of energy of the acceptor above the valence band edge. The CA luminescence band is mainly broadened by the kinetic energy of electrons before recombination.

The DA recombination processes compete strongly with the A_0X, and D_0X transitions, especially when the concentrations of donor and acceptor species are increased. The electronic interaction within an ionized donor-acceptor pair after the transitions, as illustrated in the Fig. 2.11, is responsible for the Coulomb term in the expression for the transition energy.

$$hv(DA) = E_g - (E_D + E_A) + \frac{e^2}{\epsilon r}$$

where e is the elementary charge, r the separation of the donor-accepter pair. The term e^2/r in the above equation is responsible for the spectral dispersion into a very large number of discrete lines. Each line is associated with a different discrete value of r allowed by the lattice structure.

Many impurities and defects give rise to deep energy levels in the forbidden energy gap of semiconductors. These deep states are efficient traps for excess carriers. Not only the capture process but also the resulting recombination through some of the deep centers is nonradiative. The knowledge about the deep level luminescence is important, since it controls the minority carrier lifetime.

2.3.7 Diffuse reflectance spectroscopy

Diffuse reflectance spectroscopy (DRS) is an excellent sampling tool for powdered or crystalline materials in the mid-IR and NIR spectral ranges. It can also be used for analysis of intractable solid samples. Diffuse reflectance is an excellent sampling technique as it eliminates the time-consuming process of pressing pellets for transmission measurements. The energy gap (E_g) of semiconductor is an important features which determines their applications in optoelectronics. The UV-Vis absorption spectroscopy is frequently used to characterize semiconductors thin films [25]. Due to low scattering in solid films, it is easy to extract the E_g values from their absorption spectra knowing their thickness. However, in colloidal samples, the scattering effect is enhanced since more superficial area is exposed to the light beam. In normal incidence mode, dispersed light is counted as absorbed light and the technique (optical absorption) does not distinguish between the two phenomena. On the other hand, it is common to obtain powdered samples instead of thin films or colloids, and frequently UV-Vis absorption spectroscopy is carried out dispersing the sample in liquid media like water, ethanol or methanol. If the particle size of the sample is not small enough, it precipitates and the absorption spectrum is even more difficult to interpret. In order to avoid these complications, it is desirable to use DRS, which enables to obtain E_g of un-supported materials [26].

Diffuse reflectance spectra were proposed by Kubelka and Munk (K-M) [27]. Originally they proposed a model to describe the behavior of light traveling inside a light-scattering specimen, which is based on the following differential equations:

$$\begin{aligned} -di &= -(S+K)i\,dx + Sj\,dx \\ dj &= -(S+K)j\,dx + Si\,dx \end{aligned} \qquad (1)$$

where *i* and *j* are the intensities of light traveling inside the sample towards its un-illuminated and illuminated surfaces, respectively; *dx* is the differential segment along the light path; *S* and *K* are the so called K-M scattering and absorption coefficients, respectively. These last two quantities have no direct physical meaning on their own, even thought they appear to represent portions of light scattered and absorbed, respectively, per unit vertical length [28]. This model holds when the particle size is comparable to, or smaller than the wavelength of the incident light, and the diffuse reflection no longer allows to separate the contributions of the reflection, refraction, and diffraction (i.e. scattering occurs).

In the limiting case of an infinitely thick sample, thickness and sample holder have no influence on the value of reflectance (R). In this case, the K-M equation at any wavelength becomes.

$$\frac{K}{S}=\frac{(1-R_{\infty})^{2}}{2R_{\infty}}=F(R_{\infty}) \qquad (2)$$

$F(R_{\infty})$ is the so-called remission or Kubelka-Munk function, where $R_{\infty}=R_{Sample}\,/\,R_{standard}$ [29].

In the parabolic band structure, the band gap E_g, and absorption coefficient α of a direct band gap semiconductor are related through the well known equation [30];

$$\alpha h\nu = C_1\sqrt{(h\nu - E_g)} \qquad (3)$$

where, α is the linear absorption coefficient of the material, $h\nu$ is the photon energy and C_1 is a proportionality constant. When the material scatters in perfectly diffuse manner (or when it is illuminated at 60± incidence), the K-M absorption coefficient K becomes equal to 2α ($K=2\alpha$). In this case, considering the K-M scattering coefficient S as constant with respect to wavelength, and using the remission function in Eq. (3), the expression can be obtained.

$$[F(R_{\infty})h\nu]^{2} = C_2(h\nu - E_g) \qquad (4)$$

Therefore, obtaining $F(R_{\infty})$ from Eq. (2) and plotting the $[F(R_{\infty})h\nu]^{2}$ against $h\nu$, the band gap E_g of a powder sample can be extracted easily.

DRS relies upon the focused projection of the spectrometer beam into the sample where it is reflected, scattered and transmitted through the sample material (Fig. 2.12). The back reflected, diffusely scattered light (some of which is absorbed by the sample) is then collected by the accessory and directed to the detector optics. The inside wall of the sphere is coated with a material that is nearly a Lambertian diffuser and at the same time has a high directional hemispherical (diffuse) reflectance − about 0.9 for the IR spectral range: plasma sprayed Cu on a brass substrate, electroplated with Au. The sphere has entrance, sample, and reference ports, all centered on a great circle of the sphere. The detector's field of view is centered on the same normal and corresponds to the bottom region of the sphere. The sample and the reference ports are located symmetrically with respect to the entrance port. The Hg:Cd:Te (MCT) detector Dewar is mounted on the top of the sphere. A pair of rotation stages underneath the sphere is used to move the sphere into positions for both reflectance and transmittance measurements.

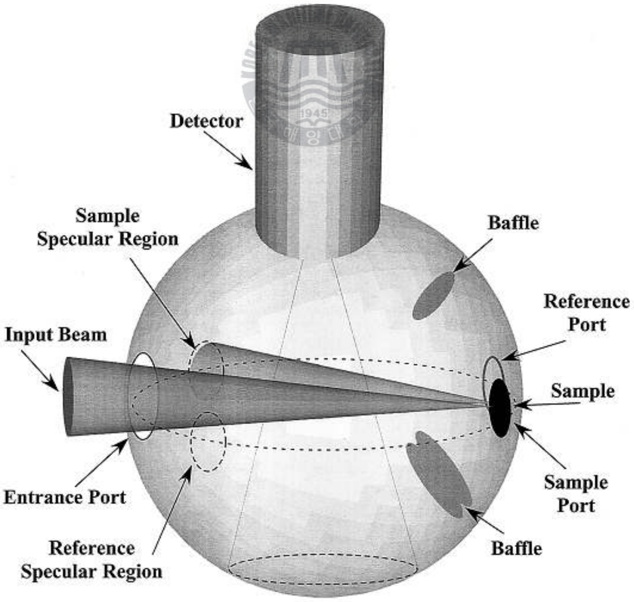

Fig. 2.12 Schematic system of integrated sphere in DRS; The sphere has entrance, sample, and reference ports.

An integrating-sphere system has been designed and constructed for multiple optical properties measurement in the IR spectral range. It is used for both diffuse and specular samples, the absolute transmittance and reflectance can be measured directly and the absorptance or emittance can be obtained from these by simple calculation. These properties are measured using a Fourier transform spectrophotometer as the spectrally tuned light source. Measurement procedures allow the absolute values of the properties to be determined for both specular and diffuse samples.

2.3.8 Hall measurement

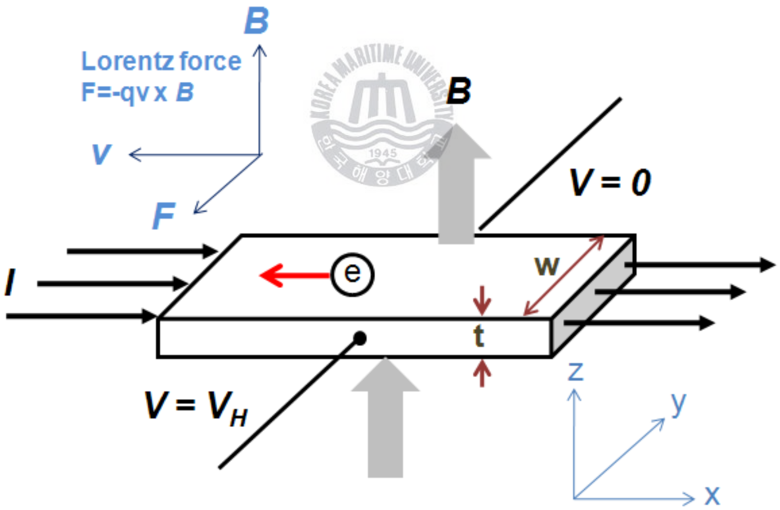

KOREA MARITIME UNIVERSITY 1945

Fig. 2.13 n-type bar-shaped semiconductor under magnetic and electric fields

The basic physical principle underlying the Hall effect is the Lorentz force. When an electron moves along a direction perpendicular to an applied magnetic field, it experiences a force acting normal to both directions, and moves in response to this force and the force effected by the internal electric field. Let's consider an n-type, bar-shaped semiconductor shown in the Fig. 2.13.

The carriers are predominately electrons of bulk density *n*. Assuming that a constant current *I* flows along the x-axis from left to right in the presence of a z-directed magnetic field, electrons subject to the Lorentz force initially drift away from the current line toward the negative y-axis. Thus, an excess surface electrical charge on the side of the sample is raised. This charge results in the Hall voltage, a potential drop across the two sides of the sample. This transverse voltage is the Hall voltage V_H and its magnitude is equal to *IB/qnd*, where *I* is the current, *B* is the magnetic field, *d* is the sample thickness, and *q* (1.602 x 10^{-19} C) is the elementary charge. It is convenient to use layer or sheet density ($n_s = nd$) instead of bulk density. Then, following equation can be obtained.

$$n_s = \frac{IB}{q|V_H|}$$

Thus, by measuring the Hall voltage V_H and from the known values of *I*, *B*, and *q,* the sheet density n_s of charge carriers in semiconductors can be determined. The Hall voltage is negative for *n*-type semiconductors and positive for *p*-type semiconductors, which means conducting type of the semiconductors can be determined by Hall effects measurements. he sheet resistance R_S of the semiconductor can be conveniently determined by use of the van der Pauw resistivity measurement technique. Since sheet resistance involves both sheet density and mobility, the Hall mobility from the equation can be determined from following equation.

$$\mu = \frac{|V_H|}{R_s IB} = \frac{1}{q n_s R_s}$$

If the conducting layer thickness *d* is known, the bulk resistivity ($r = R_S d$)

and the bulk density ($n = n_S/d$) can be determined.

There are practical aspects which must be considered when carrying out Hall and resistivity measurements. Primary concerns are

(1) ohmic contact quality and size (small ohmic contancs on the corners)

(2) sample uniformity

(3) accurate thickness determination

(4) thermomagnetic effects due to nonuniform temperature

(5) photoconductive and photovoltaic effects which can be minimized by measuring in a dark environment.

(6) sample lateral dimensions must be large compared to the size of the contacts and the sample thickness.

(7) accurate measurement of sample temperature

(8) accurate measurement of magnetic field intensity

KOREA MARITIME UNIVERSITY 1945 한국해양대학교

References

[1] M.N. Jung, J.H. Chang et al, J. Nanosce. & Nanotech. 6 3528 (2006)

[2] B.D. Yao, Y.F .Chen et al, Appl. Phys. Lett. 81 757 (2002)

[3] Z. Chen, Z. Shan et al, Scripta Mater. 52 63 (2005)

[4] Wagner, R. S., and Ellis, W. C., Appl. Phys. Lett. 4 89 (1964)

[5] Yang, P., et al., Adv. Funct. Mater. 12 323 (2002)

[6] Wang, X. D., et al., Nano Lett. 4 423 (2004)

[7] Park, J.-H., and Park, J.-G., Curr. Appl. Phys. 6 1020 (2006)

[8] Jie, J., et al., Appl. Phys. Lett. 86 031909 (2005)

[9] Hu, P., et al., Chem. Commun. 1304 (2003)

[10] Zhang, J., et al., J. Cryst. Growth 280 509 (2005)

[11] Wang, Z. L., Annu. Rev. Phys. Chem. 55 159 (2004)

[12] Hughes, W. L., and Wang, Z. L., J. Am. Chem. Soc. 126 6703 (2004)

[13] Sun, Y., et al., J. Phys. Chem. B 110 15186 (2006)

[14] Greene, L. E., et al., Nano Lett. 5 1231 (2005)

[15] Wang, Z., et al., Langmuir 20 3441 (2004)

[16] Cembrero, J., et al., Thin Solid Films 451-452 198 (2004)

[17] Mari, B., et al., Microelectron. J. 35 79 (2004)

[18] D.Q. Yu, L.Z. Hu et al, Appl. Surf. Sci. 255 4430 (2009)

[19] W. Lee, M.C. Jeong et al, Nanotechnology 16 764 (2005)

[20] C.L. Hsu, S.J. Chang et al, Nanotechnology 17 516 (2006)

[21] M.N. Jung, E.S. Lee et al, J. Alloys Compd. 481 649 (2009)

[22] C.M. Lieber, Solid State Commun., 107 607 (1998)

[23] Z.L. Wang, Y. Liu and Z. Zhang, Handbook of Nanophase and Nanostructured Materials, Volume II Characterization, Springer (2002)

[24] C. Richard Brundle, Charles A. Evans et al, Encyclopedia of Materials characterization: surfaces, interfaces, thin films (1992) by Butterworth-

Heinemann, an imprint of Elsevier

[25] U. Pal, D. Samanta, S. Ghorai, and A.K. Chaudhuri, J. Appl.Phys. 74 6368 (1993)

[26] D.G. Barton, M. Shtein, R.D. Wilson, S.L. Soled, and E. Iglesia, J. Phys. Chem. B 103 630 (1999)

[27] P. Kubelka and F. Munk, Z. Tech. Phys. 12 593 (1931)

[28] L. Yang and B. Kruse, J. Opt. Soc. Am. A 21 1933 (2004)

[29] J. Torrent and V. Barr´on, Encyclopedia of Surface and Colloid Science. (Marcel Dekker, Inc.: New York, 2002)

[30] R.A. Smith, Semiconductors, 2nd ed. (Cambridge University Press: Cambridge, 1978)

KOREA MARITIME UNIVERSITY 1945 한국해양대학교

Chapter 3. Growth and characterization of dispersive 0-dimensional (0D) doped ZnO nanostructures

3.1 Introduction

Zinc oxide (ZnO) is a wide-gap (E_g =3.44 eV) compound semiconductor, which is known as one of the suitable materials for the realization of novel optoelectronic devices, since it has a distinctive optical property such as efficient excitonic emission even at room temperature [1]. Also, ZnO-based nanostructures are expected to reveal novel properties owing to the size effects, which will reduce the density of states at band edges and enhance radiative recombination due to carrier confinement [2]. Therefore, there have been numerous studies on the various ZnO nanostructures such as nanowires [3], nanorods [4], tetrapods [5], nanobelts [6], nanotubes [7], and nanosheets [8] by thermal evaporation [9], vapor deposition [10], hydrothermal method [11], spray pyrolysis [12], catalyst-mediated organization [13,14], and electrodeposition [15]. Among the diverse ZnO nanostructures, 0-dimensional (0D) tetrapod-shape nanostructures are known as stable and tough structure, which is an important point for the purpose of application. Also high purity material could be easily obtained by thermal evaporation without any catalysts or additives. Therefore, there have been several studies on the optical [3,16,17], structural [17,18], and device applications [6,19] of this structure. Although the previous studies on the tetrapod structure have been actively achieved, there are still problems for a wide application.

The doping and alloying technologies are suggested to widen potentiality of ZnO nanostructure. As mentioned in the chapter. 1.5, the group III-metal impurity

(M=Al, Ga, and In) is used to dope dispersive 0D ZnO nanostructure. Various physical properties by impact of dopants are investigated in terms of morphological variation, structural, optical, and electrical properties.

3.2 Review on growth model of tetrapod structure

Tetrapod structure like powder-type is simply synthesized via evaporation process of Zn powder at high temperature. All existing models describe growth mechanism of the tetrapod ZnO (T-ZnO) out of a seed nucleus as shown in Fig. 3.1.

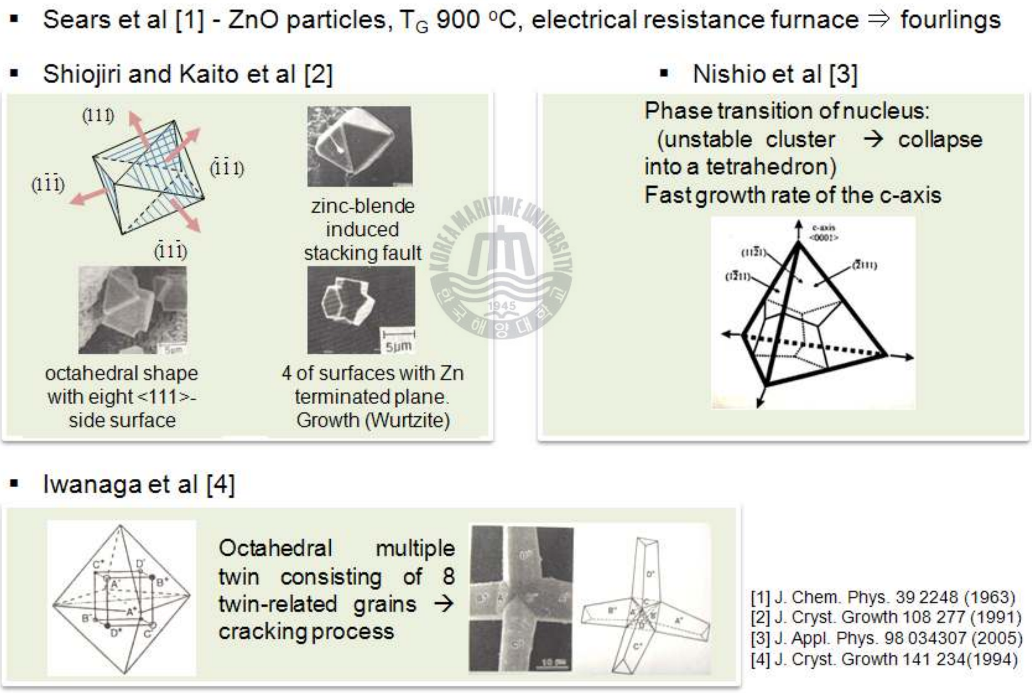

- Sears et al [1] - ZnO particles, T_G 900 °C, electrical resistance furnace ⇒ fourlings
- Shiojiri and Kaito et al [2]

zinc-blende induced stacking fault

octahedral shape with eight <111>-side surface

4 of surfaces with Zn terminated plane. Growth (Wurtzite)

- Nishio et al [3]

Phase transition of nucleus:
(unstable cluster → collapse into a tetrahedron)
Fast growth rate of the c-axis

- Iwanaga et al [4]

Octahedral multiple twin consisting of 8 twin-related grains → cracking process

[1] J. Chem. Phys. 39 2248 (1963)
[2] J. Cryst. Growth 108 277 (1991)
[3] J. Appl. Phys. 98 034307 (2005)
[4] J. Cryst. Growth 141 234(1994)

Fig. 3.1 Various growth models of ZnO tetrapod crystals

The main difference between these models is that they propose a nuclei with different shapes, geometries, and crystallographic structures, which are subsequently overgrown during the growth process along fast growing planes.

However, they do not consider the earlier nucleation and the formation of the nucleus out of the gas phase.

Shiojiri and Kaito suggested a growth model in which the seed nucleus is a zinc-blende and a single-crystalline ZnO nanocrystal of octahedral shape with eight <111>-side surfaces [20]. Four of the surfaces are zinc terminated and act as nucleation sides for hexagonal ZnO crystals, which overgrow the nucleus resulting in T-ZnO. The cubic structure of the nucleus and the interface between the two phases have not been observed directly, but the ambiguous diffraction pattern of the material after etching experiments indicates a cubic structure of the remaining material. On the other hand, cubic ZnO phases are not stable in ambient circumstances and, especially the nanosized particles, should undergo a phase transformation to w-ZnO.

Nishio *et al*. proposed a phase transformation of a cubic tetrahedral nucleus in their growth model by a lattice plane slip resulting in a multiply twinned hexagonal crystal with various elements [21]. The number of twin elements varies between four and six in their model, depending on which specific plane slipped and induced transformation. These suggestions are based on high-resolution transmission electron microscopy (HRTEM) investigations, where the authors observed T-ZnO consisting of four or six elements. However, they also found seven-element T-ZnO nanostructures and the calculated angles between two legs, using such a model, do not agree with the angles measured previously by Fujii et al [22].

Lastly, Iwanaga *et al*. introduced the common octahedron twin model, [23] which has been described in detail in several publications [22,24,25] and has recently been adopted by two other groups [26,27]. The main idea of this model is that the center nucleus is an octahedral multiple inversion twin made up of eight-trigonal pyramidal crystals with a 0001 basal plane and three $[11\bar{2}2]$ twin planes. Such an eight-trigonal pyramidal crystal cannot construct a perfect octahedron because the angle between two $[11\bar{2}2]$ planes is 85.5 ° and not 90 °. Thus, a cracking process between twin boundaries during crystal growth was assumed to release the possibly accumulated misfit strain energy. This model perfectly describes the observed crystal geometric structure; however, none of the experiments showed that the center core of T-ZnO contains an octahedral seed crystal.

If the tetrapod structure is overgrown at high temperature, second phase (lamellae) between two legs will be found. This phenomenon can be explained as follows; the boiling point of zinc is about 1180 K, and a reaction in such a high temperature is no longer a gas-liquid but gas-gas reaction, in which the control of oxidation reaction by the volume of oxygen is no longer suitable. In short the second phase is apt to generate under oxygen deficiency in the growth process.

3.3 Experimental

3.3.1 Growth of dispersive 0D undoped ZnO nanostructures

0D ZnO nanostructures were grown using a horizontal tube furnace and Zn powder (5N) without/with graphite. Dry nitrogen was used as a carrier gas. The flow rate of carrier gas was fixed to 300 sccm. To control the Zn vapor pressure, Zn amount in a range of 0.05 ~ 0.2 g varied. The growth temperature was controlled from 900 ^{o}C to 1100 ^{o}C. The prepared Zn powder on the horizontal tray was inserted at growth temperature in the center of the horizontal tube furnace. The variation of shape and dimension were observed by scanning electron microscopy (SEM) and the optical properties were characterized by photoluminescence (PL) measurement with He-Cd laser (325 nm, 10 mW) at room temperature.

3.3.2 Growth of dispersive 0D Al, Ga, and In-doped ZnO nanostructures

0D Al-doped ZnO nanostructure

Al-doped ZnO (ZnO:Al) nanostructures were synthesized by the vapor-solid nucleation method with/without graphite. The graphite amount is fixed as 0.005 g. To synthesize the ZnO:Al nanostructure, the mixture of Al (3N) and Zn (5N) powders was used as a source material. To control the Al-concentration, the weight ratio of Al (WR_{Al} = Al/[Zn+Al]) among the total weight of the mixed sources was varied. The mixed sources were loaded in a quartz tray, and introduced into a horizontal reaction tube with an inner diameter of 36 mm. The synthesis has been performed at 1100 ^{o}C under the nitrogen gas flow of 300 sccm for 30 min and powder-like white product was obtained. The shape and size of ZnO:Al nanostructures were observed by a field emission-scanning electron microscopy (FE-SEM). The nominal Al-concentration was estimated by using energy dispersive spectroscopy (EDX). Crystal structure was characterized by transmission electron microscopy (TEM).

0D Ga-doped ZnO nanostructure

Ga-doped ZnO (ZnO:Ga) nanostructures have been synthesized via the vapor-solidification method by heating the source mixture in a horizontal reactor with a diameter of 36 mm under the carrier gas ambient. As a carrier gas, nitrogen carrier gas is introduced into the quartz tube with a flow rate of 300 standard cubic centimeter per minute (sccm) to control the residual oxygen concentration. The other end of the quartz tube was open to the air. Ga-doping has been performed by using a mixed source of Zn, Ga_2O_3 and graphite powders. It was mixed to a certain ratio and loaded into a reactor using a specially designed quartz tray. The growth temperature was 1100 ^{o}C and the growth time was 30 min. After increasing the reactor temperature to a designated value, the mixed source was loaded in the tray and then the tray was introduced into the reactor. The variation of shape and dimension of synthesized nanostructures were observed by a FE-SEM.

Photoluminescence (PL) spectra of ZnO:Ga nanostructures were measured using a continuous wave He-Cd laser (325 nm) and a monochromator with a focal length of 32 cm. The Ga-content and the microstructure of ZnO:Ga nanostructures were evaluated by hard X-ray photoemission spectroscopy (HXPES).

0D In-doped ZnO nanostructure

In-doped ZnO (ZnO:In) nanostructures with various indium contents are synthesized by vapor transportation method with mixed sources (Zn and In powders) in a horizontal tube furnace. To control the In content of ZnO:In nanostructures, the In weight ratio (WR_{In}) in a mixed source (In/[Zn+In]) was controlled. The synthesis of ZnO:In nanostructures was performed by using a quartz tray at a growth temperature of 1100 ^{o}C under the nitrogen gas flow of 300 sccm. After reaction for 30 min, the morphologies of products were investigated by FE-SEM. The In-content of the products was confirmed by inductive coupled plasma atomic emission spectroscopy (ICP-AES), and the electronic structure of the ZnO:In samples was investigated by bulk sensitive HXPES.

3.4 Growth condition determination of the dispersive 0D undoped ZnO nanostructures

Crystals grow at thermal equilibrium conditions to the final shape determined by Wulff theorem. Namely, the crystals are bound with surface planes of minimum total surface free energy. However, the growth of nanostructures in reality takes place under nonequilibrium conditions; thus, the final morphology of the crystals may deviate greatly from what Wulff theorem predicts, which means that the growth behavior of various planes is manifested kinetically. Therefore, the growth takes place under circumstances far from thermal equilibrium, and the kinetics plays a more significant role in determining the morphology of the structure.

3.4.1 Control of the growth parameters

Fig. 3.2 shows growth conditions of dispersive 0D ZnO nanostructures grown by adjusting Zn flux such as Zn source amount and growth temperature, under carrier gas of 300 sccm. It is reported that the growth temperature and carrier gas flux have a great influence on the formation of ZnO nanostructures [28]. Although the carrier gas flux influences the residual pressure of group-VI element (O) in the furnace, I can determine the growth condition of ZnO nanostructures by changing only Zn flux under fixed carrier gas flow as shown in the Fig. 3.2.

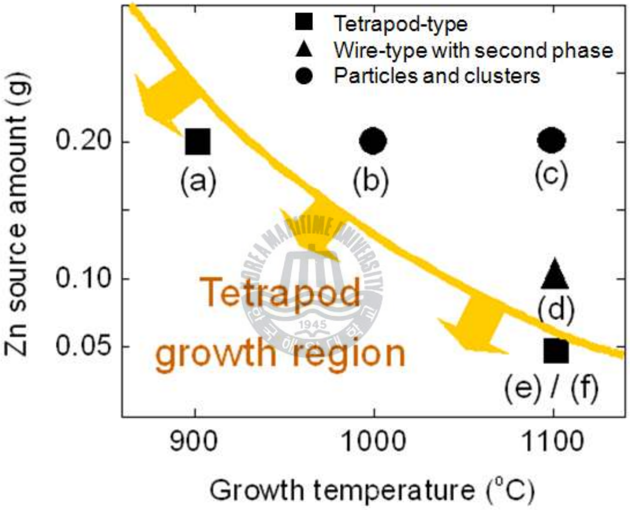

Fig. 3.2 Growth condition of dispersive 0D undoped ZnO nanostructures

3.4.2 Structural and optical properties

The morphologies of ZnO nanostructures grown at the different growth condition show in the Fig. 3.3. With increasing growth temperature (a-c) at the same Zn-amount of 0.2 g, the morphology of nanostructures is changed from tetrapod structures (a) to particles (b-c). To dope 0D ZnO nanostructure, physical properties of dopants should be considered. Compared to Zn-metal powder, group III-metals such as Al, Ga, and In have much more low vapor pressure. Therefore the growth temperature was fixed as high as 1100 ^{o}C. At the growth temperature of 1100 ^{o}C, ZnO nanostructures with uniform tetrapod-type (e) was obtained. Also, ZnO nanostructures grown with graphite at the same condition of (e) show negligible morphology change except a certain increase of secondary phase (a sheet like morphology in the Fig. 3.3(f)).

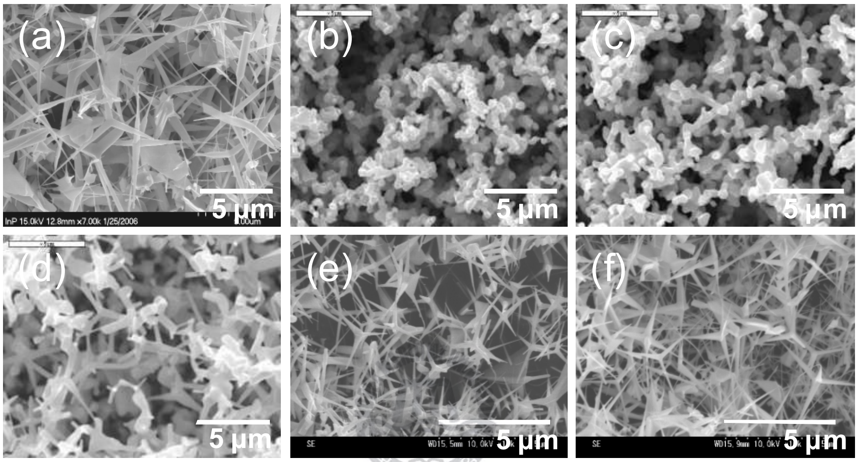

Fig. 3.3 Morphology of the ZnO nanostructures grown at different growth condition; (a) 900 ^{o}C, Zn-0.2 g, (b) 1000 ^{o}C, Zn-0.2 g, (c) 1100 ^{o}C, Zn-0.2 g, (d) 1100 ^{o}C, Zn-0.1g, (e) 1100 ^{o}C, Zn-0.05 g, (f) 1100 ^{o}C, Zn-0.05 g, with graphite

Fig. 3.4 is PL spectra of the 0D ZnO nanostructures grown at different growth condition. From PL graphs of Figs. 3.4(a-c), the tetapod-type nanostructures show the strong UV emission of 3.2 eV with a weak deep level emission. However, the morphology variation (tetrapod → particle) originated from disparity of VI/II ratio degrades the optical properties. Also, graphite deteriorates the luminescence intensity due to disparity of VI/II ratio as shown in the Fig. 3.4(f). As a consequence, the growth condition of dispersive 0D ZnO nanostructure was determinated as a Zn-amount of 0.05 g at the growth temperature of 1100 ^{o}C.

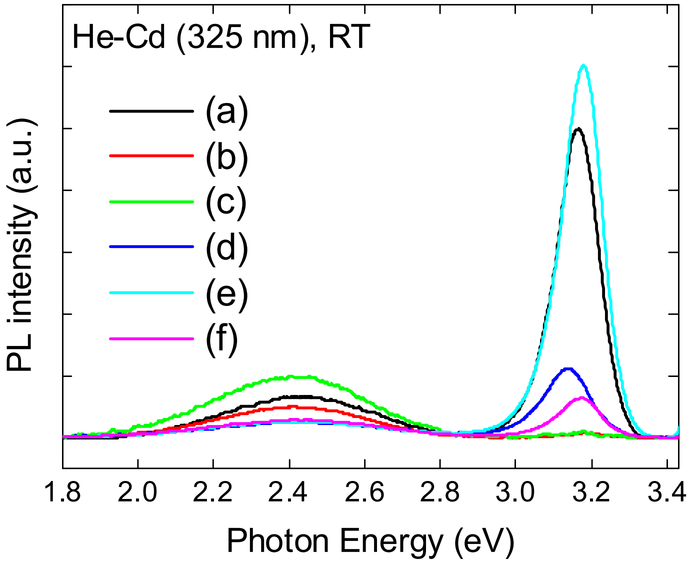

Fig. 3.4 PL spectra of the 0D ZnO nanostructures grown at different growth condition; (a) 900 °C, Zn-0.2 g, (b) 1000 °C, Zn-0.2 g, (c) 1100 °C, Zn-0.2 g, (d) 1100 °C, Zn-0.1g, (e) 1100 °C, Zn-0.05 g, and (f) 1100 °C, Zn-0.05 g, with graphite

3.5 Characterization of dispersive 0D Al-doped ZnO nanostructures

3.5.1 Morphological variation and composition

Fig. 3.5 shows ZnO and ZnO:Al nanostructures grown under different WR_{Al} at the consistent growth condition (1100 °C, Zn-0.05 g). Fig. 3.5(a) is pure ZnO nanostructures and Figs. 3.5(b-c) are ZnO:Al nanostructures grown under WR_{Al} of 0.05 and 0.5, respectively. From EDX analysis, in case of the Figs. 3.5(b-c), the Al-content was confirmed each 0 at.% and 0.31 at.% and no remarkable morphology variation was observed. It means that Al-doping is difficult due to the rapid oxidation rate of the Al metal powders at high growth temperature of 1100 °C. Thus, I decided to add graphite in the mixed sources to increase Al concentration. Fig. 3.5(d) is ZnO nanostructure grown with graphite and Figs.

3.5(e-f) show the morphologies of ZnO:Al nanostructures grown with graphite at the same condition to (b-c). The Al-content was detected to be 0.3 at.% and 0.68 at.% from Figs. 3.5(e-f) samples, which indicates that graphite increases Al-composition in the ZnO nanostructures. However, considerable increase of secondary phase between legs of tetrapod is observed from highest Al-doped sample grown with graphite (Fig. 3.5(f)).

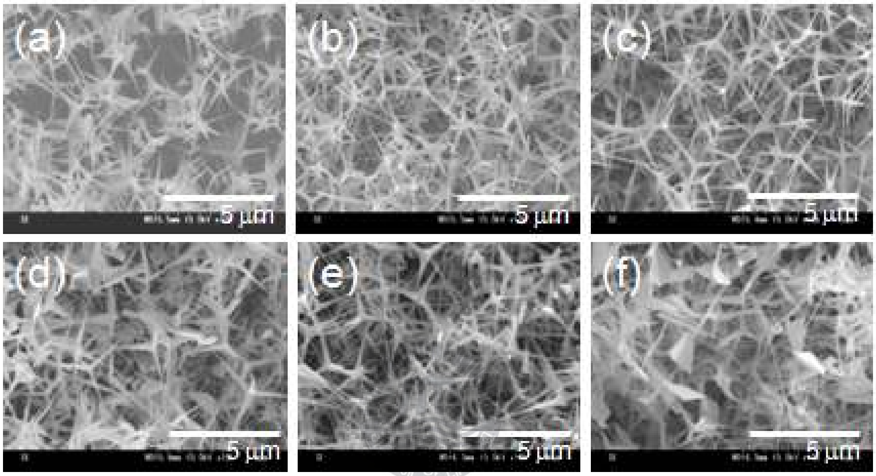

Fig. 3.5 FE-SEM images of (a) ZnO, (b) ZnO:Al, WR_{Al}-0.05 (c) ZnO:Al, WR_{Al}-0.5, (d) ZnO, (e) ZnO:Al, WR_{Al}-0.05 (f) ZnO:Al, WR_{Al}-0.5; (a-c) samples are grown using only Al powder, (d-f) are grown with Al and graphite powders.

3.5.2 TEM images

From the SEM and EDX results of 0D ZnO:Al nanostructures, graphite mixing increases the Al-composition in nanostructures. Fig 3.6 shows the TEM results of ZnO (sample A) and ZnO:Al nanostructures with relatively high Al concentration with 0.68 at.% (sample F). ZnO nanotetrapod consists of four needle-shaped tetrahedrally arranged legs connected at the center, forming a tetrapod structure. The high-resolution TEM (HR-TEM) indicates that it grows along the <0001>

direction and the clear lattice fringes show a single crystalline structures. In contrast, the ZnO:Al nanostructures (Al-0.68 %) are observed the secondary phase with tetrapods, similarly to SEM images. Furthermore, from the HR-TEM image, amorphous phase was found on the tetrapod legs, which is similar to the result reported by Yao et al [17]. From SEM and TEM results, the degradation of crystallinity like as second phase and amorphous phase is regarded as VI/II ratio change owing to the fast oxidation of Al and vaporization of graphite.

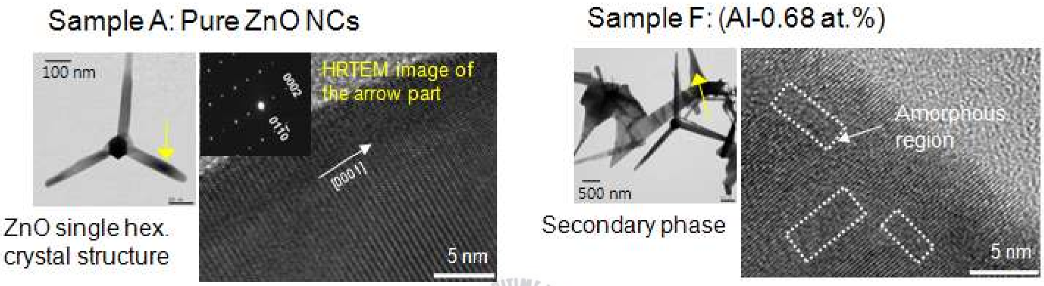

Fig. 3.6 TEM image of pure ZnO and ZnO:Al nanostructures

3.5.3 Optical property

Fig. 3.7 shows PL spectra of the ZnO:Al nanostructures grown as a function of WR_{Al} ratio and with/without graphite. The peak position of NBE emission at 3.20 eV is not changed with changing growth conditions (not shown). With increasing WR_{Al}, FWHM broadening and decrease of luminescence intensity are observed. Moreover, more faster degradation of optical properties is found out in the ZnO:Al samples grown with graphite. As mentioned above, the rapid degradation of optical property with deterioration of structural properties is deduced to be originated from non-stoichiometric VI/II ratio.

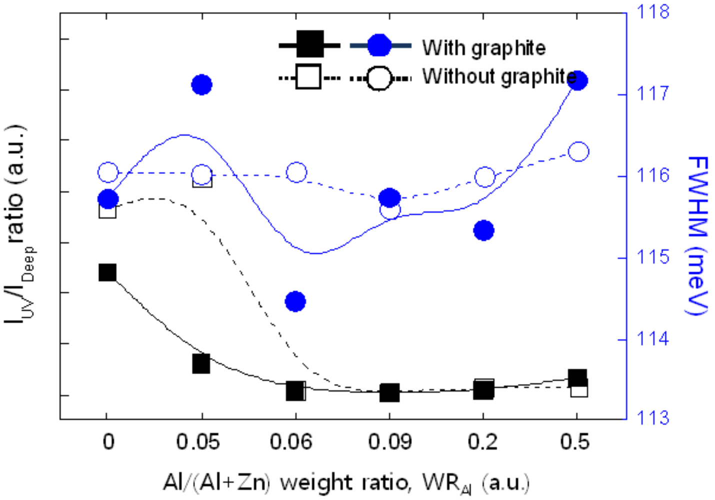

Fig. 3.7 PL spectra of the ZnO:Al nanostructures; WR_{Al}: 0.05~0.5, with/without graphite

3.6 Characterization of dispersive 0D Ga-doped ZnO nanostructures

3.6.1 Morphological variation and composition

KOREA MARITIME UNIVERSITY 1945

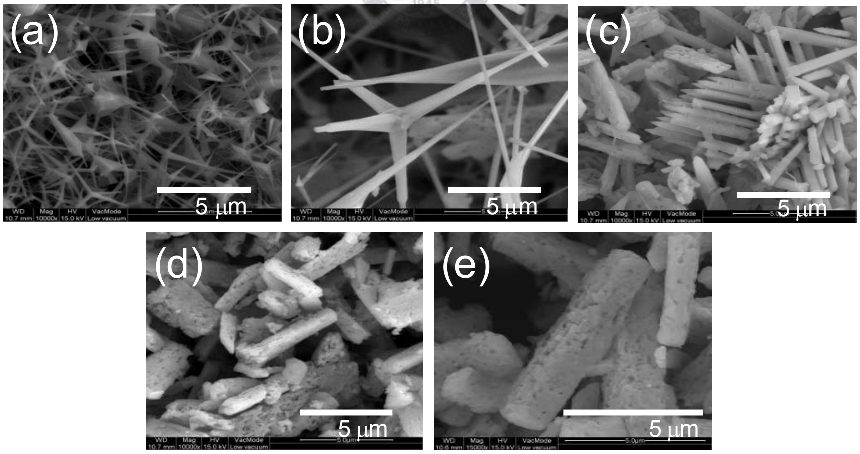

Fig. 3.8 SEM images of (a) ZnO, (b) ZnO:Ga (Ga ~ 7.7 %), (c) ZnO:Ga (Ga ~ 57.5 %), (d) ZnO:Ga (Ga~63 %), and (e) Ga_2O_3 nanostructures

ZnO:Ga nanostructures were synthesized via a vapor phase transportation method. The various ZnO:Ga nanostructures were prepared with different Ga-content. As described the experimental part, the ratio of graphite (10 %) was fixed to a source mixture and just varied Ga_2O_3/Zn ratio (WR_{Ga}) from 0 % to 100 %. After a 30 min growth, white wool-like products formed on the inner wall of the quartz tube and the tray. The powder products of ZnO:Ga nanostructures were collected on the tray in a reaction zone (1100 ^oC).

Various shapes of products such as tetrapod- and rod-like nanostructures were obtained as shown in the Fig. 3.8. When WR_{Ga} is small tetrapod-like nanostructures are mainly observed (Figs. 3.8(a) WR_{Ga}~0 and (b) WR_{Ga}~0.11), while in the large WR_{Ga} rod-like nanostructures are found (Figs. 3.8(c) WR_{Ga} ~0.5 and (d) WR_{Ga}~0.88). The Ga compositions in those samples are evaluated as (a) 0 %, (b) 7.7 %, (c) 57.5 %, (d) 63 %, and (e) 100 % by the HXPES measurements, respectively.

KOREA MARITIME UNIVERSITY 1945

Table 3.1 Summary on experimental conditions, dimensions, nominal shape, Ga-content, and classification of ZnO:Ga nanostructures

Samples	Ga weight ratio [$WR_{Ga}=Ga_2O_3/(Ga_2O_3+Zn)$]	Diameter (nm)	Length (μm)	Typical morphology	Ga-content (%)	Classification
ZnO	0	250	3-4	Tetrapod	0	Hexagonal
$ZnO:Ga_{7.7}$	0.11	<1000	>10	Tetrapod	7.7	Hexagonal
$ZnO:Ga_{57.5}$	0.50	1200	6	Rod	57.5	Monoclinic
$ZnO:Ga_{63}$	0.88	1500	7.5	Rod	63	Monoclinic
Ga_2O_3	1	2000	6.6	Rod	100	Monoclinic

As shown in the Fig. 3.8, the morphological variation presumably induced by Ga-incorporation. When the impurity composition is less than the solubility limit, the morphology of nanostructures will be maintained; thus similar shape products with undoped nanostructure will be obtained. But, when the dose is higher than the solubility-limit, structural transformation will happen. In our experiment, basic morphology of undoped nanocrystal was maintained until the Ga-composition reached ~7.7 %, while over this composition almost Ga_2O_3-like morphologies emerged. This description corresponds well with the observation. Therefore, I assume that the solubility limit of Ga into ZnO nanostructure is about 7.7 %. To confirm this assumption, investigation on the microscopic structural variation is inevitably required, since it is well-known that the successful impurity incorporation in a nanostructure is hardly achieved due to large surface energy. Therefore, a morphological variation is not enough to conclude the structural evolution. Hence, it is very important to understand the microscopic structure of impurity-incorporated nanostructures. HXPES spectra were studied to know the microstructure and Ga-composition of ZnO:Ga nanostructures. It should be noted that, since XPS is known as a surface-sensitive measurement, to investigate the bulk properties, high-energy X-ray, namely HXPES, measurement is required.

3.6.2 Phase transition and conductivity change

Fig. 3.9(a) shows the valence spectra of ZnO:Ga nanostructures. Intensity of those spectra is normalized to the intensity of the O 1*s* peak. As the Ga-content is increased, relative intensity of both Zn 4*s* (at 7.85 eV) [29] and Zn 3*d* peaks (at 10.8 eV) decreased [30], and the relative intensity of Ga 4*s* peak (at 11.7 eV) increased [31] corresponding to Ga-content increase. The sample with relatively low Ga-content shows a spectrum which is close to that of pure ZnO, while the samples with relatively high Ga-content clearly show Ga_2O_3-like spectra. However, the gradual peak position shift from Zn to Ga-related peak was not observed. It makes us exclude the possibility of alloy phase in the intermediate Ga-content, also indicating the phase separation that becomes obvious when Ga-content is higher than 50 %.

Fig. 3.9(b) shows the variation of the valence band maximum (VBM) of ZnO:Ga nanostructures. Valence band (VB) spectra are used to determine the position of the Fermi level (E_F) with respect to the VBM. The inverse triangle of each graph indicates the estimated E_F position, in which metallic states are observed. The E_F of a semiconductor will shift up/down due to donor/acceptor doping. The Fermi levels were obtained by extrapolating the leading edge of the O 2*p*-derived valence band to its intersection with the background level.

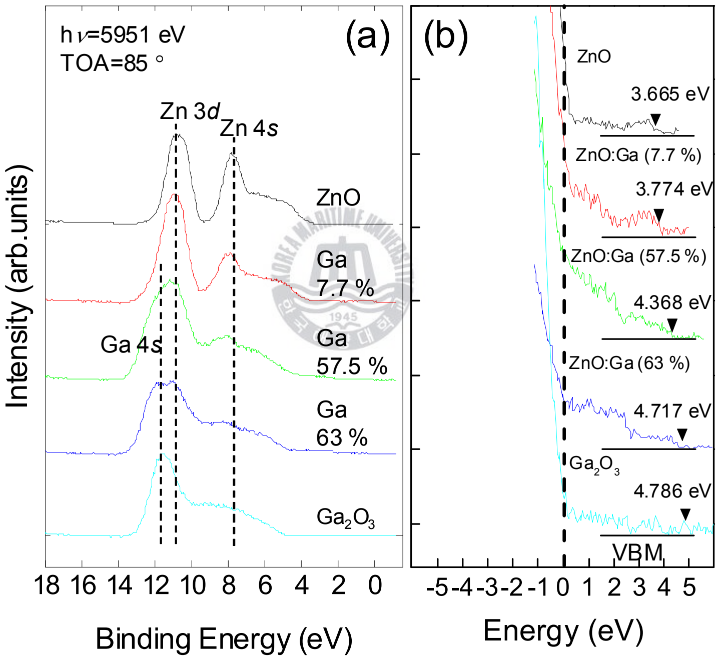

KOREA MARITIME UNIVERSITY 1945

Fig. 3.9(a) Valence Band (VB) spectra of HXPES for various ZnO:Ga nanostructures with different Ga-composition (b) Enlarged energy distribution curves near VBM

On considering the 3.37 eV energy band gap of ZnO at room temperature, the E_F of

ZnO nanostructures is observed at the high-energy side of 295 meV, which indicates n-type conductivity. Furthermore, as the Ga-content increases, the E_F shifted more to the high-energy side, presumably due to the formation of a metallic state in the conduction band. When the Ga-content exceeds 7.7 %, not conductivity increase but band gap variation to the Ga_2O_3 is observed. The energy band gap of Ga_2O_3 was reported to be 4.9 eV at room temperature [32]. In fact, optical band gap of the ZnO:Ga samples (57.5 %, 63 %, and 100 %) is 4.368 eV, 4.717 eV, and 4.786 eV. It found that morphology of ZnO:Ga is closely related with structural phase and ZnO:Ga nanostructure (7.7 %) with ZnO-like phase was confirmed the conductivity change via metallic state observation from Ga-doping.

3.7 Characterization of dispersive 0D In-doped ZnO nanostructures

3.7.1 Morphological variation and composition

The morphology of ZnO:In nanostructures was analyzed by using FE-SEM, and the results are shown in the Figs. 3.10(a-f). Various information on the sample, including the mixed source weight ratio, diameter, length, typical morphology, In-content measured by ICP-AES, and classification of each sample, is listed in the Table 3.2.

Fig. 3.10(a) shows FE-SEM image of ZnO nanostructures. The pure ZnO nanostructures show clear tetrapod-like morphology with four legs of diameter ~ 200 nm and length of 3~4 μm. Figs. 3.10(b-d) show FE-SEM images of ZnO:In nanostructures with an In-weight ratio (WR_{In} = In/[In+Zn]) of 0.063, 0.167, and 0.5, respectively. The diameter of the tetrapod increases and the length decreases along with In content. However, as long as the WR_{In} is lower than 0.5, the ZnO:In nanostructures keep tetrapod-like morphologies. Figs. 3.10(e-f) show FE-SEM images of ZnO:In nanostructures with WR_{In} of 0.833 and 1 respectively. When WR_{In} is larger than 0.5, an octahedron shape of the ZnO:In nanostructures is observed instead of a tetrapod shape. Fig. 3.10(f) shows FE-SEM images of In_2O_3 nanostructures (WR_{In} = 1) which every facet is close to an equilateral triangle with side of 400~500 nm. The distributions in size of the In_2O_3 octahedron structure are relatively uniform and the average size of products is estimated at about 450 nm.

Table 3.2 Summary on experimental conditions, dimensions, nominal shape, In content, and classification of ZnO:In nanostructures

Samples	In weight ratio (WR_{In}= In/[In+Zn])	Diameter (nm)	Length (μm)	Typical morphology	In-content (%)	Classification
ZnO	0	200	3~4	Tetrapod	0	Hexagonal
$ZnO:In_{0.05}$	0.063	220	6	Tetrapod	5	Hexagonal
$ZnO:In_{0.25}$	0.167	280	5	Tetrapod	25	Hexagonal
$ZnO:In_{0.35}$	0.500	600	4	Tetrapod	35	Hexagonal
$ZnO:In_{0.65}$	0.833	610	0.61	Octahedron	65	Cubic
$ZnO:In_{0.85}$	0.938	1450	1.45	Octahedron	85	Cubic
In_2O_3	1	500	0.5	Octahedron	100	Cubic

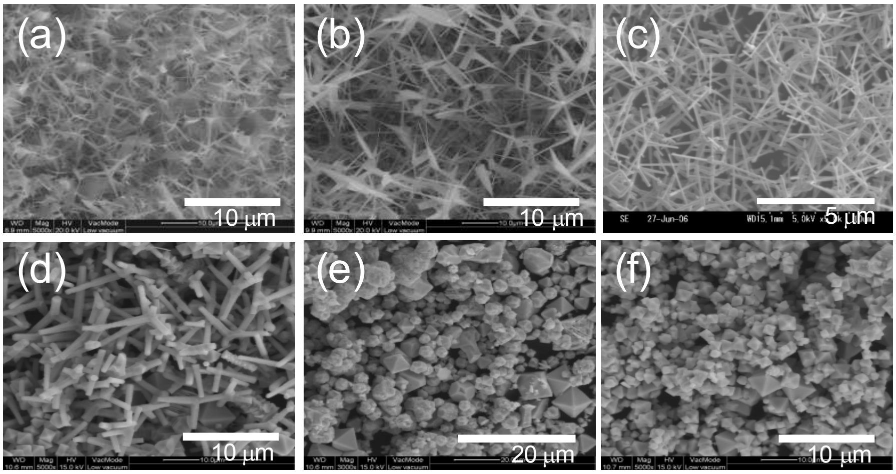

Fig. 3.10 FE-SEM images of (a) ZnO; (b) $ZnO:In_{0.05}$ (c) $ZnO:In_{0.25}$ (d) $ZnO:In_{0.35}$ (e) $ZnO:In_{0.65}$, and (f) In_2O_3 nanostructures

Based on the morphologies, the nanostructures are divided into ZnO-like hexagonal and In_2O_3-like cubic groups (as shown in the Table 3.2) and the electronic structure of each group was investigated by HXPES. The morphological change can be explained in terms of the variation of bonding coordination. Since oxygen in ZnO nanostructures has four-fold coordinate, while oxygen in In_2O_3 has six-fold coordinate, chemical bonding strength should be changed on increasing the In content. This can also be confirmed by investigating the valence band state.

3.7.2 Phase transition and conductivity change

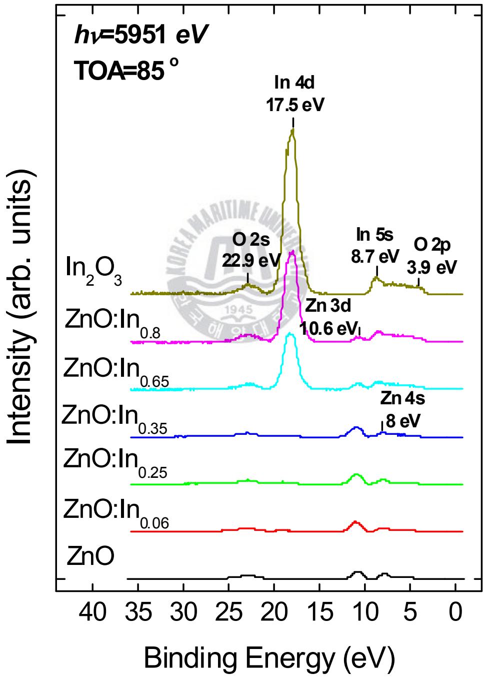

Fig. 3.11 VB spectra of HXPES for various ZnO:In nanostructures with different In-composition

Fig. 3.11 shows VB spectra of all samples. First of all, peak assignment has been performed following the previous reports [33-35]. The peak at 8 eV is assigned to the O 2*p* peak, which is hybridized with Zn 4*s* and 4*p* orbitals [33], while the peak at 4.6 eV originates from O 2*p* orbitals [34]. The peaks at 8.7 eV and 10.6 eV are attributed to the In 5*s* and Zn 3*d* [33,35] peaks, respectively. The peaks indicated by In 4*d* and O 2*s* are positioned at 17.5 eV and 23 eV, respectively [35]. Also, the In-content for each sample measured by ICP-AES is noted. Compared with WR_{In}, the measured In-content increased slowly, due to the higher vapor pressure of Zn than In. The VB spectra show systematic variation of peak position and intensity as In content increases.

Similarly to the FE-SEM results, the VB spectra were divided into the two groups: ZnO-like and In_2O_3-like groups, based on the intensity of the In 4*d* transition. As one can see in the Fig. 3.11, the ZnO-like group has negligible intensity of the In 4*d* peak, but the In_2O_3-like group has a remarkable intensity of the In 4*d* transition. From $ZnO:In_{0.65}$ (In content was measured to be 65 %), the In 4*d* peak dominates the spectrum.

KOREA MARITIME UNIVERSITY 1945

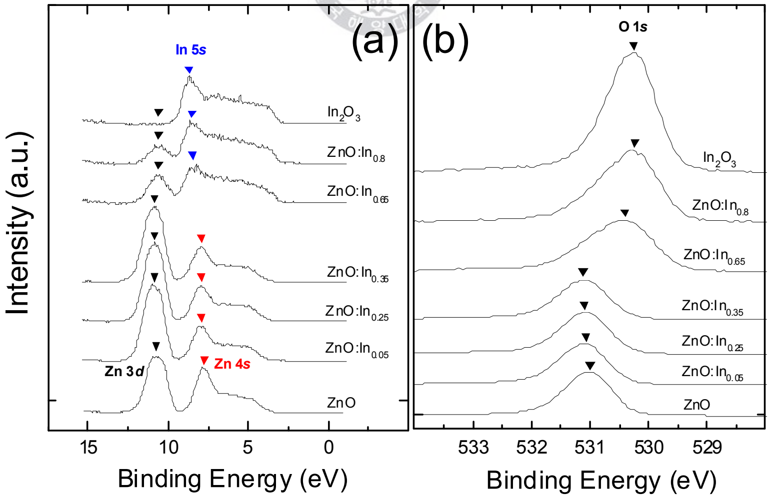

Fig. 3.12(a) VB spectra of binding energy (E_b) within ~15 eV, and (b) O 1*s* core level spectra

Fig. 3.12(a) shows details of the VB spectra up to a binding energy (E_b) of 15 eV. In 5*s*, Zn 3*d*, and Zn 4*s* transitions are shown. From the ZnO-like group, the Zn 4*s* (red inverse triangle) and Zn 3*d* (black inverse triangle) peak positions are shifted to the high-binding-energy side as the In-content increases. However, in the case of the In_2O_3 group a considerable E_b shift of Zn-related transitions was not observed; instead, the intensity of the In 5*s* (blue inverse triangle) and Zn 3*d* peaks shows In content-related behavior. From the ZnO:$In_{0.85}$ sample, the In 5*s* position is well matched with pure In_2O_3. This result clearly shows that 1) In incorporation enhances the binding energy of Zn 3*d* and Zn 4*s* levels, but 2) a further increase of In-content results in phase transformation. Hence, the Fermi-level shift is expected owing to indium doping.

Fig. 3.12(b) shows the O 1*s* core level spectra. In our experiment, the O 1*s* peak was observed at 531.1 eV for ZnO nanostructures, while it was observed at 530.3 eV for In_2O_3 nanostructures. The black inverse triangle of each spectrum indicates the O 1*s* peak shift. The integral intensity of the O 1*s* peak increases as In-content increases. This result clearly shows that the chemical bonding of oxygen is varied along with In-content, due to the bonding coordination change. There have been various discussion on the oxygen core level spectrum. In the case of ZnO:Al films, an oxygen core level shows two spectral components. One component at 531.25 ± 0.20 eV was estimated to be related with O^{2-} ions in the oxygen-deficient regions within the ZnO matrix [36]. The other component at 530.15 ± 0.15 eV was attributed to the O^{2-} ions in the wurtzite structure of the hexagonal Zn^{2+} ion array [37-39]. From the previous reports on In_2O_3 thin films [40], the oxygen signals show two O 1*s* peaks, centered at 531.5 eV and 533.3 eV. The binding energy at 533.3 eV was attributed to an adsorbed oxygen or hydroxide in the surface of the film. The other peak at 531.5 eV is explained to originate from O 1*s* of In_2O_3 films. Although there are discrepancies in the assignment of the oxygen core level spectrum, I tentatively attributed the increase of integral intensity and position shift to structural transformation by the bonding coordination change.

Until now, I have considered the In-incorporation-induced morphological and structural variations of ZnO:In nanostructures. However, the other important point will be the variation of band structure. Fig. 3.13 shows the variation of the valence band maximum (VBM) of ZnO:In nanostructures.

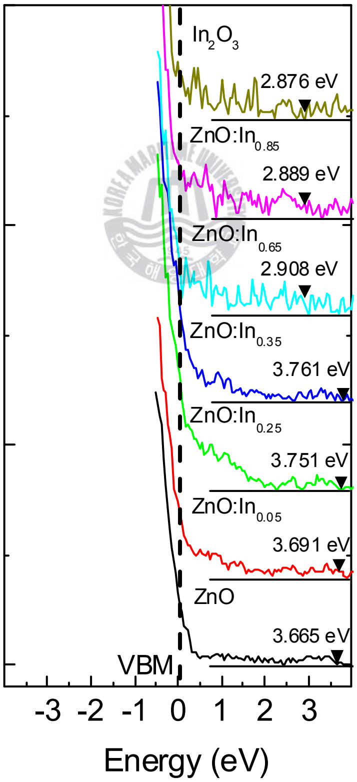

Fig. 3.13 Enlarged energy distribution curves near the VBM

As the In-content increases, the E_F shifted more to the high-energy side, presumably due to the formation of a metallic state in the conduction band. When the In-content exceeds 35 %, E_F begins to shrink, due to the energy band-gap shrinkage. The energy band gap of In_2O_3 was reported to be 2.6 eV at room temperature [41]. Therefore, the situation can be summarized as follows: when the In content is low, E_F will shift toward the high-energy side, due to substitutional incorporation of In atoms, but, when the In-content exceeds a certain amount (in this experiment it is estimated to be 35 %), both phase transformation from hexagonal to cubic and energy band gap shrinkage happen, which can be monitored in terms of morphological transformation.

3.7.3 Crystal structure and optical property

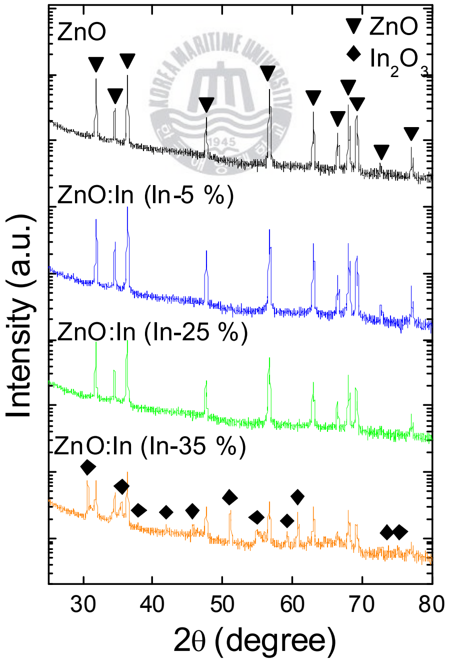

Fig. 3.14 Powder crystal X-ray diffraction patterns of ZnO and ZnO:In nanostructures

Powder-crystal X-ray diffraction (XRD) measurements were performed to investigate the structural property of ZnO:In nanostructures. Fig. 3.14 shows respective powder XRD patterns for ZnO and ZnO:In nanostructures with different R_{In} values. The strong diffraction peaks in the Fig. 3.14 (denoted by black inverted triangles) are easily assigned to wurtzite-phase ZnO (JCPDS file no. 35−1541) with lattice constants of a = 0.324 nm and c = 0.521 nm. Approximately similar assignment is possible within $WR_{In} < 0.167$ (In ≤ 25 %). However, when the $WR_{In} > 0.5$ (In ≥35 %), In_2O_3 related diffraction peaks (denoted by black diamonds) are detected, which corresponds with the SEM results.

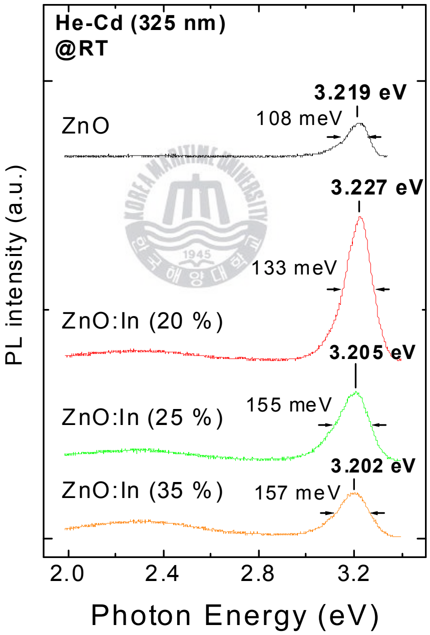

Fig. 3.15 Room temperature PL spectra of ZnO and ZnO:In nanostructures

Fig. 3.15 shows the room temperature PL spectra of ZnO and ZnO:In nanostructures. Near band edge (NBE) emission is observed at 3.219 eV from ZnO nanostructures, while it red-shifted with increasing In-content. Two possible explanations have considered for the red-shift of NBE emission. The first explanation might be a transition from direct to indirect band gap . Since In_2O_3 is known to have an indirect band gap of 2.6 eV at room temperature [41], ZnO:In nanostructure could have an indirect band gap especially in high In-concentration range. However, if the red-shift is related with the indirect transition, the PL intensity should be decreased, but that was not observed in this experiment. The NBE emission intensity of ZnO:In (35 %) is higher than that of pure-ZnO nanocrystal. Optical band gap shrinkage of ZnO:In nanostructures might be a semiconductor-metal transition, namely Mott shift [42], might be the next presumable explanation for the phenomenon. It explains the narrowing of the band gap as a result of merging of the donor level and conduction band at high impurity density, there fore red-shift of band-edge emission occurs owing to considerable increase of carrier density. Theoretically the Mott density is known to be inversely proportional to the cube of Bohr radius [42], and the reported Mott density for ZnO:In ($d_{Mott} > 4\times10^{19}$ cm^{-3}) is lower than that of ZnO:Al ($d_{Mott} > 4.5\times10^{20}$ cm^{-3}) and ZnO:Ga ($d_{Mott} > 4\times10^{20}$ cm^{-3}) [43-45].

Since the former discussion is not supported by experimental result, the red-shift is tentatively assigned due to Mott transition. Remind that the NBE intensity of ZnO:In (35 %) nanostructures is higher than that of ZnO. Impurity doping frequently accompanies an increase of PL intensity. Various ZnO films doped with group-III atoms show an increase of NBE intensity along with carrier concentration [46], although it reduces owing to the increase of non-radiative recombination centers at high impurity concentration region. The variation of PL intensity and peak position of ZnO nanostructures (shown in Fig. 3.15) could be summarized as follows; in low impurity concentration region, NBE emission intensity increases along with the impurity concentration. However, when the impurity concentration reached a certain amount, the NBE intensity begins to decrease due to the increase of non-radiative recombination centers. If the impurity concentration is as high as Mott density, red-shift of peak position will be accompanied. Note that the linewidth of NBE emission variation increases continuously with increasing In-content. Since PL linewidth broadens by the inhomogeneous strain induced by structural fluctuation, linewidth broadening indicates the increase of impurity concentration and degradation of crystal quality. It should be attributed to not only for the large difference in the covalent bonding length of In and Zn but also for the inhomogenious impurity distribution in the nanostructures. Consequently, PL spectra strongly indicate that an increase of extrinsic carrier concentration in ZnO:In nanostructure, but more direct evidence is necessary to confirm the discussion.

3.7.4 Electrical properties

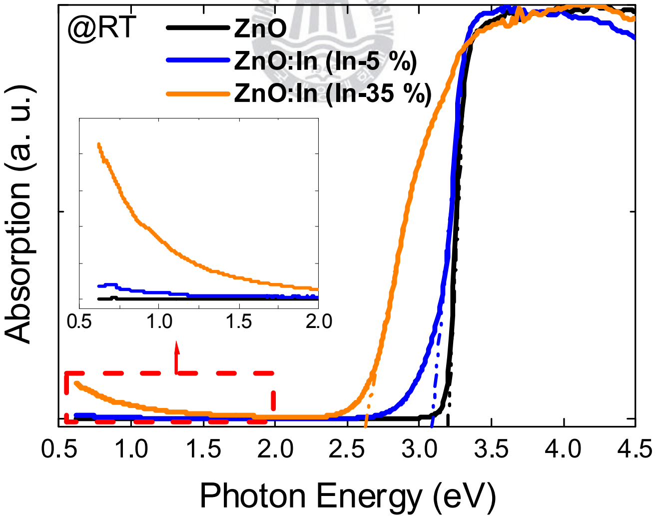

Fig. 3.16 DRS of ZnO and ZnO:In nanostructures. The emersion of absorption edge (0.6~2.0 eV) indicates free carrier absorption in the samples.

Fig. 3.16 shows Diffuse-reflectance spectra (DRS) of ZnO:In samples. Since the samples are in powder-phase which has considerable scattering at the surface, it needs to measure by accumulating scattered light using an integral sphere to obtain absorption spectra. From the absorption spectra as shown in Fig. 3.16, free carrier absorption was confirmed in terms of the emersion of absorption edge at around 0.6 ~ 2.0 eV. Although, the free carrier absorption in ZnO:In (In~35 %) nanostructures (with the highest In-concentration) should be attributed to the structural phase transition, but the free carrier absorption from the other samples should be understood due to an increase of free carriers in the conduction band caused by extrinsic impurities.

3.8 Summary

In this chapter, to dope group III-metal impurity (M=Al, Ga, and In) in the dispersive 0D ZnO nanostructures, the growth condition was determined by controlling growth parameters. Morphological variation, structural, optical and electrical properties of the M-doped ZnO nanostructures grown under consistent growth condition were investigated. Conductivity change always accompanies with morphological change of nanostructure. From that point of view, it was confirmed that the ZnO:In nanostructures have high doping concentration (~ 25 %) with uniform structures among Al, Ga, and In-impurities. Moreover, the enhanced extrinsic carrier concentration by In-doping was revealed in terms of fermi level shift and free carrier absorption.

References

[1] Z.K. Tang, G.K.L. Wang, P. Yu, et al., Appl. Phys. Lett. 72 3270 (1998)

[2] K. Park, J.S. Lee, M.Y. Sung, et al., J. Appl. Phys. 41 7317 (2002)

[3] W.D. Yu, X.M. Li, X.D. Gao, Appl. Phys. Lett. 84 2658 (2004)

[4] W.I. Park, D.H. Kim, S.W. Jung, G.C. Yi, Appl. Phys. Lett. 80 4232 (2002)

[5] T.W. Kim, T. Kawazoe, T. Sekiguchi, et al., Appl. Phys. Lett. 84 3358 (2004)

[6] Q. Wan, K. Yu, T.H. Wang, C.L. Lin, Appl. Phys. Lett. 83 2253 (2003)

[7] Y.B. Li, Y. Bando, T. Sato, et al., Appl. Phys. Lett. 81 144 (2002)

[8] L. Dloczik, R. Engelhardt, K. Ernst, et al., Appl. Phys. Lett. 78 3687 (2001)

[9] B.D. Yao, Y.F. Chen, N. Wang, Appl. Phys. Lett. 81 757 (2002)

[10] Z. Chen, N. Wu, Z. Shan, S.X. Mao, et al., Scripta Mater 52 63 (2005)

[11] J.H. Choy, E.S. Jang, J.H. Won, et al., Appl. Phys. Lett. 84 282 (2004)

[12] S.R.C. Vivekchand, G. Gundiah, et al., Adv. Mater. 16 1842 (2004)

[13] C.J. Lee, T.J. Lee, S.C. Lyu, Y. Zhang, et al., Appl. Phys. Lett. 81 3648 (2002)

[14] Q.X. Zhao, M. Willander, et al., Appl. Phys. Lett. 83 165 (2003)

[15] M. Izaki, S. Watase, H. Takahashi, Adv. Mater. 15 2000 (2003)

[16] J.Q. Hu, Y. Bando, J.H. Zhan, et al., Appl. Phys. Lett. 83 4414 (2003)

[17] V.A.L. Roy, A.B. Djurisic, W.K. Chan, et al., Appl. Phys. Lett. 83 141 (2003)

[18] H. Yan, R. He, J. Pham, P. Yang, Adv. Mater. 15 402 (2003)

[19] Q.H. Li, Q. Wan, Y.J. Chen, et al., Appl. Phys. Lett. 85 636 (2004)

[20] M. Shiojiri and C. Kaito, J. Cryst. Growth 52 173 (1981)

[21] K. Nishio, T. Isshiki, M. Kitano, and M. Shiojiri, Philos. Mag. A 76 889 (1997)

[22] M. Fujii, H. Iwanaga, M. Ichihara, and 17S. Takeuchi, J. Cryst. Growth 128 1095 (1993)

[23] H. Iwanaga, M. Fujii, and S. Takeuchi, J. Cryst. Growth 134 275 (1993)

[24] S. Takeuchi, H. Iwanaga, and M. Fujii, Philos. Mag. A 69 1125 (1994)

[25] H. Iwanaga, M. Fujii, M. Ichihara, and S. Takeuchi, J. Cryst. Growth 141 234 (1994)

[26] Y. Dai, Y. Zhang, and Z. L. Wang, Solid State Commun. 126 629 (2003)

[27] D. W. Zeng, C. S. Xie, B. L. Zhu, R. Jiang, X. Chen, W. L. Song, J. B. Wang, and J. Shi, J. Cryst. Growth 266 511 (2004)

[28] M.N. Jung, S.Y. Ha, H.S. Kim, and J.H. Chang et al, J. Nanosci. and Nanotech. 6 3628 (2006)

[29] R.T. Girard, O. Tjernberg, G. Chiaia, S. SoNderholm et al, Appl. Surf. Sci. 373 409 (1997)

[30] A.C. Thompson, D. Vaughan, in: X-ray Data Booklet Lawrence Berkeley National Laboratory, University of California, Berkeley, CA, pp. 1.3 (2001)

[31] J.J. Yeh, I. Lindau, At. Data Nucl. Data Tables 32 1 (1985)

[32] L. Binet, D. Gourier, J. Phys. Chem. Solids 59 1241 (1998)

[33] M. Gabas, S. Gota, J.R. Ramos-Barrado, M. Sanchez, N.T. Barrett, J. Avila, M. Sacchi, Appl. Phys. Lett. 86 042104 (2005)

[34] G.W. Cong, W.Q. Peng, H.Y. Wei, X.X. Han, J.J. Wu, X.L. Liu, Q.S. Zhu, Z.G.Wang, J.G. Lu, Z.Z. Ye, L.P Zhu, H.J. Qian, R. Su, C.H. Hong, J. Zhong, K. Ibrahim, T.D. Hu, Appl. Phys Lett. 88 062110 (2006)

[35] V. Brinzari, G. Korotcenkov, V. Matolin, Appl. Surf. Sci. 243 335 (2005)

[36] John C.C. Fan, JohnB. Goodenough, J. Appl. Phys. 48 3524 (1997)

[37] R. Cebulla, R. Wendt, K. Ellmer, J. Appl. Phys. 83 1087 (1998)

[38] T. Szorenyi, L.D. Laude, I. Bertoti, Z. Kantor, Zs. Geretovszky, J. Appl. Phys. 78 6211 (1995)

[39] S.L.K. Rao, V. Vinni, Appl. Phys. Lett. 63 608 (1993)

[40] G.E. Buono-core, G. Cabello, B. Torrejon, M. Tejos, R.H. Hill, Materials Research Bulletin 40 1765 (2005)

[41] X.S. Peng, G.W. Meng, J. Zhang, X.F. Wang, Y.W. Wang, C.Z. Wang, L.D.

Zhang, J. Mater. Chem. 12 1602 (2002)

[42] N.F. Mott, Metal-Insulator Transitions, Tayor and Francis, London (1974)

[43] K.J. Kim, Y.R. Park, Appl. Phys. Lett. 78 475 (2001)

[44] J. Hu, R.G. Gordon, J. Appl. Phys. 72 5381 (1992)

[45] B.E. Sernelius, K.-F. Berggren, Z.-C. Jin, I. Hamberg, C.G. Granqvist, Phys. Rev. B 37 10244 (1988)

[46] J. Jie, G.Wang, X. Han, Q. Yu, Y. Liao, G. Li, J.G. Hou, Chem. Phys. Lett. 387 466 (2004)

KOREA MARITIME UNIVERSITY 1945 한국해양대학교

Chapter 4. Growth and characterization of integrated 1-dimensional (1D) doped ZnO nanostructures

4.1 Introduction

Recent advances in the field of nanotechnology have led to the synthesis and characterization of an assortment having 1-dimensional (1D) structures, such as nanorods, nanoneedles, nanowires and nanotubes. These fascinating materials exhibit novel physical properties owing to their unique geometry with high aspect ratio. Among various materials mentioned in chapter 1.2, the zinc oxide (ZnO) is the most interesting material because of its attractive optical functions based on the large binding energy of excitons and biexcitons (60 and 15 meV, respectively) as well as its multifunctional physical properties. Notable applications of 1D ZnO nanostructures include the fabrication of nanometer scale electronic devices such as light-emitting diodes [1], nanolasers [2,3], gas sensors [4,5], field-effect transistors [6], and dye-sensitized solar cells [7].

The preparation of ZnO nanostructures has been demonstrated by various methods, including vapor phase methods [2,8,9-11], hydrothermal process [12] and template-based methods [13]. Among them, vapor phase methods such as thermal evaporation and condensation [8,10], carbon thermal reduction vapor transport [2,10] and evaporation of organic zinc precursors [12] have been used for producing ZnO nanostructures. Such methods are often performed using metal catalysts like Au [2,14], Cu [15], Sn [16], NiO [9] and Co [17] to assist and control the growth process. Hence, the metal catalyst will influence growth kinetic as well as the purity of the final products. In order to meet the demand of potential applications offered by ZnO nanostructure, both high quality n-type and p-type materials are indispensable. Therefore, it is necessary to control doping with intrinsic or extrinsic elements to optimize their structural, optical and electrical properties.

In this chapter, synthesis and characterization on doped integrated ZnO nanostructure using group III-metal impurity (M=Al, Ga, and In) are described.

4.2 Theoretical background

4.2.1 Review on the growth model

In 1964, Wagner and Ellis [18] produced Si whiskers on the Si(111) surface by chemical vapor deposition (CVD) growth technique using Au catalyst and proposed the so-called vapor–liquid–solid (VLS) mechanism of whisker formation. In this mechanism, whiskers are assumed to grow due to the adsorption of vapor atoms on the drop surface and the solidification of supersaturated liquid alloy on the surface under the drop [18-22]. In 1973, Givargizov and Chernov proposed a theoretical model of whisker formation by the VLS mechanism [19,20]. Later, the VLS concept was extended to include the nanometer-scale whiskers and is now widely used for the explanation of nanowire (NW) formation [21-23]. The empirical Givargizov and Chernov's formula [19] for the whisker growth rate $dL = dt$ (L is the whisker length and t the time) reads

$$dL = dt = k_1(\Delta\mu/k_BT - k_2/D)^2.$$

Here, $\Delta\mu$ is the vapor supersaturation, T is the surface temperature, K_B is the Boltzmann constant, k_1 is the unknown kinetic coefficient of growth for the solid/liquid interface between the NW tip and the alloy drop, k_2 is the characteristic radius, related to the vapor-solid surface energy, α_{VS} with Ω being the volume per atom in a crystal,

$$k_2 = 2\alpha_{VS}\Omega / k_B T,$$

where α_{VS} is the specific surface energy of the interface between the NW and the vapor around it. The D-dependent term in Givargizov and Chernov's expression arises due to the Gibbs−Thomson effect of elevation of chemical potential of cylindrically shaped crystal phase with diameter D. Kashchiev's formula for the growth rate of crystal face with diameter D [24,25] does not account for the Gibbs−Thomson effect (Appendix. A) but accounts for the transition from mono-nuclei to poly-nuclei mechanism of nucleation mediated growth of NWs. This effect is associated with the finite size of growing face that affects the number of islands mediating the NW growth. Since in mono-nuclei mechanism the growth rate is proportional to D^2 and in poly-nuclei mechanism it is independent of D, the NW growth rate generally should depend on D. Kashchiev's formula for $dL = dt$ is given by [24] $dL = dt = \alpha_1 D^2 / (1 + \alpha_2 D^2)$, where coefficients α_1 and α_2 depend on $\Delta\mu$, while their dependence on D can often be neglected. From the given expressions it follows that both models predict the increase of $L(D)$ dependence, thicker NWs thus growing faster than the thinner ones. Such $L(D)$ dependence was obtained in many experiments on CVD growth of NWs [19-21]. The generalized model of NW formation by VLS mechanism of Ref. [22] accounts for the Gibbs−Thomson effect and for the finite size of growing facet simultaneously. This theory also results in an increase of $L(D)$ dependence. It should be noted here that the maximum length of NWs in the adsorption-induced VLS growth is limited by the effective thickness of deposited material $H(L < H)$, the case $L = H$ corresponds to zero desorption from the drop and sufficiently large NW diameter D.

In contrast, the contribution of the adatom diffusion from the surface to the NW tips along their sidewalls may be important. Recently, Schubert et al. [26] obtained experimentally the $L(D)$ dependence of Si whiskers grown by MBE on the Si(111)-Au surface. They found that narrower whiskers grew much faster than the thicker ones. The measured $L(D)$ curve was found to be close to the inversely proportional relation $L \propto 1/D$. Kinetic model of diffusion-induced (DI) growth of NWs during MBE was developed in Refs [27,28]. It was shown theoretically and verified experimentally for GaAs NWs with sufficiently small diameters (D ~100 nm or less) at growth temperature T=585 ^{o}C that the DI contribution to the NW growth predominated and the adsorption-induced contribution was rather small.

4.2.2 Surface luminescence in the ZnO nanostructures

The existence of surface state bands has firmly been established both experimentally and theoretically [29,30]. Moreover, the surface states located close to the Fermi level are due to the so-called dangling band in elemental semiconductors [31]. A dangling bond on a crystal surface likely gives rise to a localized state within the band gap [32,33]. The saturated covalent bands can easily form states especially in the center of the gap. When the dimension of a semiconductor is reduced to nanometer scale, one of the key features is the large 'surface to volume' ratio (S/V), which makes nanosized materials much different from their bulks [34]. That is, the large S/V greatly increases the possibilities of dangling bonds or broken bonds in ZnO nanostructure. Surface states can be responsible for the origin of luminescence. Dynamics of the surface-related PL is related as a function of spectral position, temperature, and excitation intensity. The spectrum is strongly dominated by a broad asymmetric band peaked at 3.365 eV lying 9 meV below the free-exciton emission. Due to its spectral position and its excitation intensity dependence that will be presented in the following, this peak is assigned to the recombination of surface excitons (SX). Dominant SX emission tiny contributions from the recombination of donor-bound excitons (D_0X) can be observed at the spectral positions of 3.356 and 3.360 eV. The dominance of the SX peak is most probably due to the small diameters of the wires of d= 40 to 130 nm resulting in an overwhelming contribution of the near-surface effects. Asymmetric SX emission band consists of a whole distribution of SX states. The detected biexponential PL decay changes with the spectral position pointing to a dependence of the slow decay time (τ_2) on a kind of the exciton localizations.

With respect to temperature dependance, it is summarized that a thermal activation involves in the recombination and relaxation process. The decrease of the PL intensity with increasing temperature suggests an activation of excitons trapped in SX states into free-exciton states (FX).

The total number of near-surface states is lower than the total number of volume states. This means that the surface state transitions should be saturated at a lower excitation intensity than those of the volume states. At low excitation power, the PL is strongly dominated by the SX emission. With increasing excitation power, the D_0X peaks increase in intensity relative to the SX peak and finally dominate the spectrum. With increasing excitation power, no spectral shift is observed. This intensity dependence strongly deviated from that of D_0X supports the assignment of the SX peak to surface-related emission.

4.2.3 Negative thermal quenching phenomenon

PL intensity in semiconductors usually shows thermal quenching, i.e. a reduction in PL intensity is observed with increasing temperature. This phenomenon is ascribed to a temperature-induced increase in the nonradiative recombination probability of the PL emission. In some semiconductors, however, the PL intensity increases with increasing temperature [35,36]. It was observed in some semiconducting materials of GaAs [35,37] and ZnS [36] in some temperature range that the PL intensity also increases as temperature increases. This phenomenon is called 'negative thermal quenching (NTQ)'. Bebb *et al.* [35,36] proposed that NTQ for the eA^o emission in GaAs was due to the thermal dissociation of the D^oX system, which resulted in the ejection of a free electron into the conduction band. They could qualitatively explain the NTQ, but did not develop any analytical formula to describe the NTQ curve quantitatively.

ZnO has been emerged as a good candidate for high efficient UV/blue LED due to its large exciton binding energy of 60 meV at room temperature, high radiation resistance, and optical gain [38,39]. Recently, this NTQ was also observed in II-VI ZnO semiconductor material with large band gap (3.37 eV at RT) and the analytical formula was proposed by both Shibata and Meyer et al. Shibata [40,41,42] suggested that the principal mechanism of NTQ is the thermal excitation of electrons to the initial state of the PL transition from the eigenstates with smaller energy eigenvalues.

The simplest model for the system which exhibits PL emission consists of two electron states; intial state (~excited state) and final state (~ground state). Nonradiative transition processes from the initial state to the final state must also be taken into account. If the energy separation between the initial states and the final state is sufficiently large compared with the temperature of the system, thermal excitation of electrons from the final state to the initial state is negligible. In the system, the number of the electrons in the initial state decreases monotonically with increasing temperature. This simple model can account for the positive thermal quenching phenomenon.

However, real systems consist of multilevels; there are plural energy states between the initial state (~excited state) and final states (~ground state), namely, middle states or intermediated states. A energy diagram of the system is schematically shown in the Fig. 4.1. If the energy separation between the initial state (state A; excited states) and some of the middle states (states B_k for k= 1-w) is comparable to the temperature of the system, thermal excitation of electrons from the latter states to the former state is not negligible.

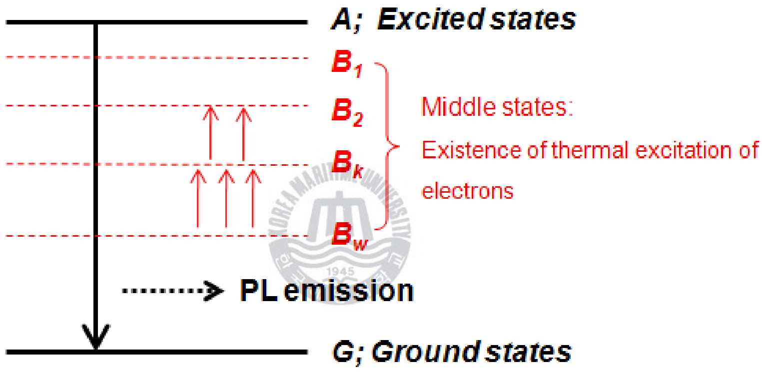

KOREA MARITIME UNIVERSITY 1945

Fig. 4.1 An energy diagram of the model system proposed for the study of the mechanism of the negative thermal quenching phenomenon. Eigenstates denoted by B_k (for k= 1-w) are the middle states between A and G.

4.3 Experimental

4.3.1 Growth of integrated 1D undoped ZnO nanostructures

Integrated 1D ZnO nanostructures were grown by vapor-phase transportation (VPT) process. First of all, a thin layer of AuGe (Ge~43 at.%) was deposited as thickness of 30 nm on Si (111) substrates. When the horizontal quartz tube furnace reached to the expected temperature (550 °C ~ 700 °C), a vertical quartz tray was inserted into the quartz tube furnace for the nanostructure growth. AuGe-coated substrate and zinc powders (5N) were placed on the same tray, the vertical distance was 13 mm. Argon was used as a carrier gas, and flows through the quartz tube during the growth with the flow rate of 200~1000 (m*l*/min). After 30 min growth, the tray was drawn out from the quartz tube furnace and cooled down to room temperature. The morphology and structures of the synthesized samples were analyzed by scanning electron microscopy (SEM) and the photoluminescence (PL) spectroscopy was used to evaluate the optical property of the samples at room temperature. A He-Cd (325 nm) laser was used as an excitation source.

4.3.2. Growth of integrated 1D Al, Ga, In-doped ZnO nanostructures

Integrated 1D ZnO:Al, Ga, and In-doped nanostructures were grown on $Au_{0.57}Ge_{0.43}$-deposited Si (111) substrates. Details on the vertical V-VPT were reported elsewhere [43]. First of all, a AuGe layer of 30 nm was deposited on Si substrate by electron-beam evaporation. For doping, Al and Zn powders, Ga and Zn powders, In and Zn powders were used as the mixture of a source materials, which corresponds to that of each ZnO:Al, ZnO:Ga, and ZnO:In nanorods (NRs). Usually, mesh size of the Al, In, and Zn powders has the value in a range of 75 ~ 150 μm, while Ga powders have the size as large as 850 μm. To control composition of the each doped nanostructures, the weight ratio (WR_{dopant}= dopant/(Zn+dopant), dopant=Al, Ga, and In powder) is varied. The growth was performed at 600 °C under Ar gas flow of 600 SCCM (SCCM denotes cubic centimeter per minute at STP). The surface morphology of each sample was observed by the Quanta 200 FEG field emission scanning electron microscope (FE-SEM). The concentration of dopant in the sample is characterized by energy dispersive x-ray spectroscopy (EDX). The crystal structure and crystal quality of the sample are investigated by X-ray diffraction (XRD) using Cu K_1 line and photoluminescence (PL) at room temperature with He-Cd laser 325 nm as an excitation source. Also the carrier concentration (*n*) was measured by using the Van der Pauw method.

4.4 Growth condition determination of the integrated 1D undoped ZnO nanostructures

The experimental parameters that determine or influence the morphology of the ZnO nanostructures include the gas-phase supersaturation, the surface energy of the growing surface planes, the temperature at the source material and the substrate, temperature gradient in the tube furnace, the distance from the source material and the substrate, the heating rate of the furnace, the gas flow rate, the inner diameter of the ceramic tube, and the starting material. It is generally believed that growth temperature and gas-phase supersaturation determine the growth rate of surface planes and the final morphology of the crystals, with other experimental parameters playing minor roles. Here, I describe the effect of the experimental parameters including the catalyst, growth temperature, the gas flow rate on influencing the growth of integrated 1D ZnO nanostructures.

4.4.1 Control of the growth parameters

Growth parameter; catalyst

Fig. 4.2 shows the morphology of the ZnO nanorods grown with or without catalyst. The images of the Figs. 4.2(a-c) are ZnO nanorods synthesized without AuGe (Ge~ 43 %) at different growth temperature of 600~700 ^{o}C under same carrier gas of 600 sccm. As shown in the Figs. 4.2(a-c), random orientation, irregular density, and diameters with a few hundred nanometers are regarded as bad morphology in terms of uniform rod growth. On the other hand, Fig. 4.2(d) shows uniform ZnO nanostructures grown with a catalyst at the growth temperature of

600 ^{o}C under a carrier gas flow of 600 sccm.

The growth orientation is important for many applications of nanostructures. The well-aligned nanorods can be vertically grown on the substrate by using proper substrate and reaction conditions. Also, catalyst improves the structural morphology in terms of orientation, density, and diameter in the nanostructures.

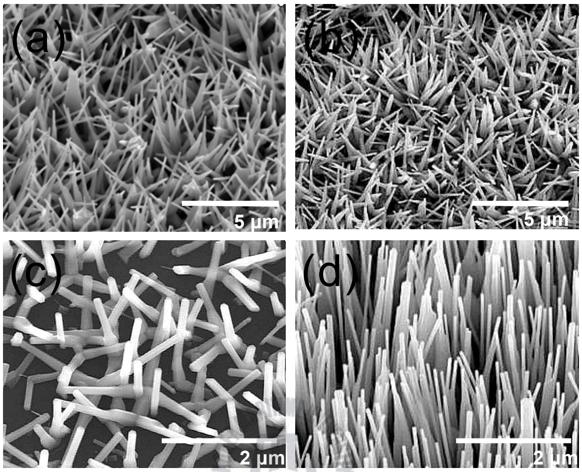

Fig. 4.2 SEM images of ZnO nanorods grown on Si substrate with a carrier gas flow of 600 sccm at different growth temperature without catalyst (a-c); (a) 600 ^{o}C, (b) 650 ^{o}C, (c) 700 ^{o}C, (d) 600 ^{o}C- with AuGe catalyst

Growth parameter; growth temperature and carrier gas flow

Figs. 4.3(a-c) show the morphology of ZnO nanorod grown at different growth temperature (550-700 ^{o}C) under fixed carrier gas flow of 1000 sccm. The images of Figs. 4.3(d-f) are results grown with changing the carrier gas flow of 200-1000 sccm at the same growth temperature of 600 ^{o}C. From the view point of size, density, and alignment of nanorods, the growth conditions for ZnO nanorods are fixed as the growth temperature of 600 ^{o}C under carrier gas flow of above 600 sccm.

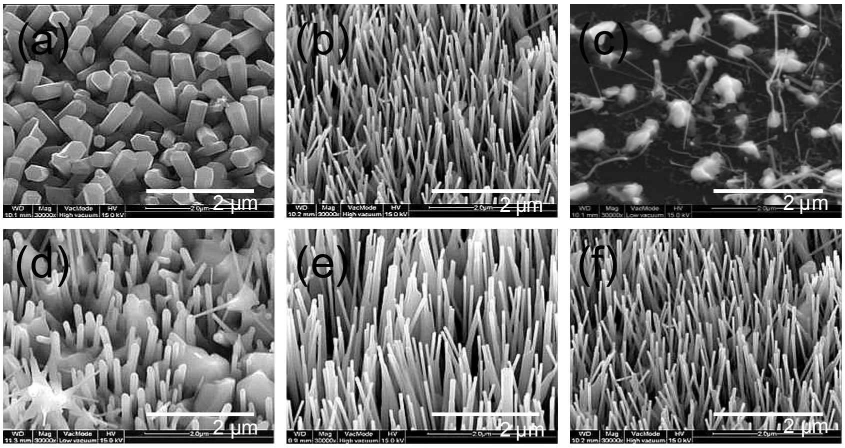

Fig. 4.3 SEM images of ZnO nanorods grown at various growth temperature and flow rate of carrier gas. The samples of (a), (b) and (c) are grown at 550, 650, 700 ^{o}C with a carrier gas of 1000 sccm, respectively. The samples of (d), (e) and (f) are grown at 600 ^{o}C with the carrier gas flows of 200, 600, 1000 sccm.

Although there might be many parameters that affect the formation of nanostructures, the growth temperature determines the vapor pressure of Zn and thermodynamic processes. Therefore, it is generally believed as the most important parameter for nanostructure formation. The conventional model to explain the growth mechanism of 1D structure involves the participation of VLS in the growth process. The central idea of the VLS growth can be divided into two stages: (1) the nucleation and growth of eutectic alloy droplets and (2) the growth of nanorods through the liquid droplets due to supersaturation. During the growth process, the catalyst absorbs the vapor components such as Zn (vapor) and Zn_xO ($x < 1$, vapor), to form a eutectic alloy. When it is supersaturated, crystallization of ZnO will occur [44]. It should be pointed out that if the ambient temperature of this process is too high, oxygen vaporization will be accelerated and the nanostructure tends to contain a lot of oxygen deficiencies. Various reports support this description, generally at high growth temperature the degradation of optical property and forfeit of uniformity are observed [45]. In this experiment, therefore, the growth temperature is restricted to 600 ^{o}C considerably lower than that for AuGe-catalyzed VPT method.

Generally speaking, very low supersaturation (=low growth temperature, low carrier gas flow) favors the growth of perfect crystals with the internal symmetry, moderately low supersaturation benefits the formation of nanowires, medium supersaturation facilitates the growth of nanobelts, moderately high supersaturation (=high growth temperature, high carrier gas flow) tends toward the formation of nanoplatelets, nanosheets, and continuous films, and very high supersaturation causes the rapid formation of poorly crystallized crystals with undefined morphology. This finding may have an important impact on understanding the morphology evolution of nanostructures and achieving desired nanostructures controllably.

KOREA MARITIME UNIVERSITY 1945

4.5 Characterization of integrated 1D Al-doped ZnO nanostructures

4.5.1 Morphological variation and composition

Fig. 4.4 shows the SEM images of ZnO:Al nanostructures grown by changing mixed source ratio (WR_{Al}= 0~0.75) of Zn and Al powders under the consistent growth condition at 600 ^{o}C under 600 sccm.

With increasing Al-composition, the surface to volume ratio (S/V ratio) of ZnO:Al nanorods decreases; (a) 0.059 → (b) 0.028 → (c) 0.019 → (d) 0.009. The Al-content of Figs. 4.4(a-d) is confirmed to be (a) 0 at.%, (b) 0.37 at.%, (c) 0.53 at.%, and (d) 0.69 at.% from EDX, respectively. Compared to the maximum doping concentration (0.31 at.%) of the 0D ZnO:Al nanostructures synthesized at same WR_{Al} ratio of 0.5, that (0.53 at.%) of 1D ZnO:Al nanorods is much increased. Although it is well known that the vapor pressure has a linear relationship with the growth temperature, the increase of Al oxidation rate by growth temperature plays a role to hinder the Al-doping.

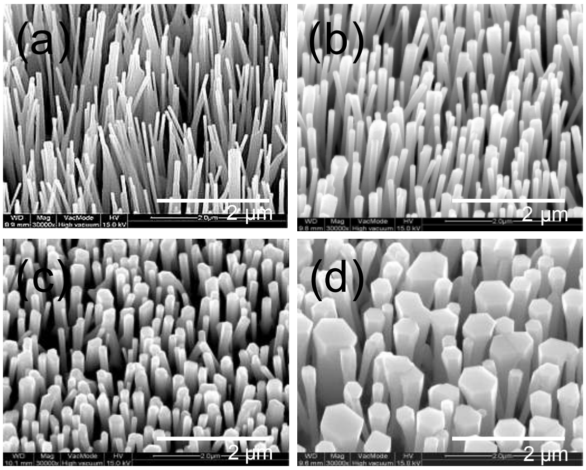

Fig. 4.4 SEM images of ZnO:Al nanorods grown by different mixed source ratio, WR_{Al} of (Al/(Al+Zn)) (a) 0 (b) 0.25 (c) 0.5 (d) 0.75 at 600 ^{o}C under carrier gas of 600 sccm

4.5.2 Optical and electrical properties

Fig. 4.5 is the PL spectra of ZnO:Al nanostructures at room temperature. With increasing Al-composition, the near-band-edge (NBE) emission peak is shifted to the high energy direction by 17 meV (Not shown). The decrease of relative luminescence ratio (I_{NBE} to I_{Deep}; I_{NBE}/I_{Deep}) and the FWHM increase are observed as Al-composition increases. Especially, the fast degradation of the optical property indicates above 0.5 at.% of Al-composition. The broadening of PL band with increasing Al-content and the decrease of luminescence intensity have been usually reported from ZnO:Al film [46,47].

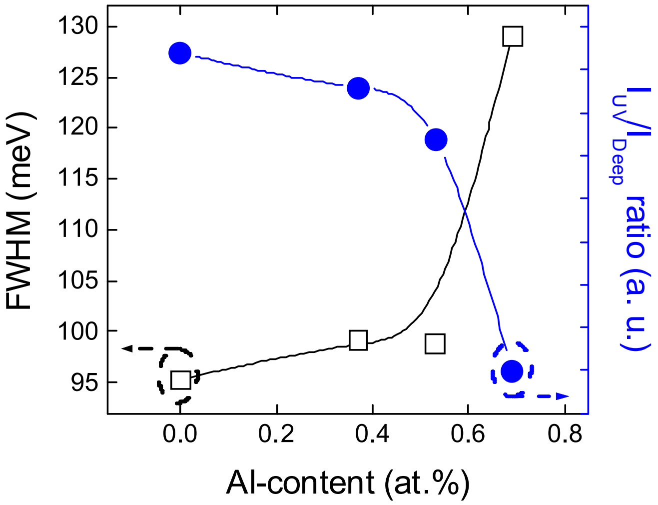

Fig. 4.5 PL spectra of ZnO:Al nanorods

KOREA MARITIME UNIVERSITY 1945 한국해양대학교

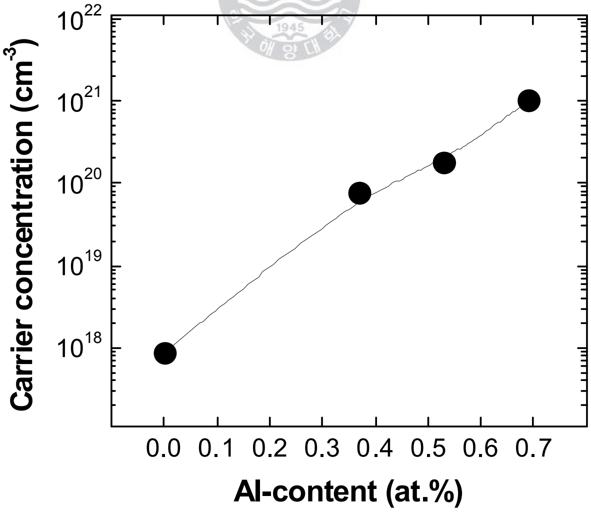

Fig. 4.6 Carrier concentration variation as a function of Al-content in ZnO:Al nanorods

In order to discuss this issue qualitatively, electron concentration should be investigated. Hall effect measurement is used to evaluate electrical properties of ZnO and ZnO:In nanorods, which was performed by using the transition layer (the ZnO:Al_x film with thickness *H, H* is confirmed from the side-view images), instead of preparing a film deposited under the similar growth conditions [48], because usually there are many differences. The extrinsic carrier concentration increases in proportion to WR_{Al} ratio as shown in the Fig. 4.6.

4.6 Characterization of integrated 1D Ga-doped ZnO nanostructures

4.6.1 Morphological variation and composition

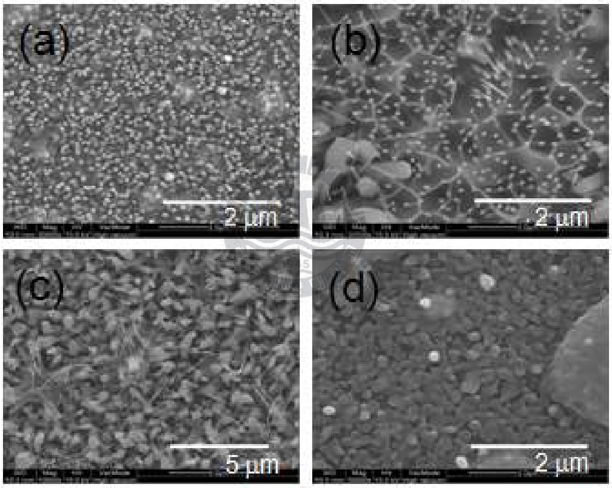

Fig. 4.7 SEM images of ZnO:Ga nanostructures grown by different mixed source ratio, WR_{Ga} of (Ga/(Ga+Zn)) (a) 0, (b) 0.024, (c) 0.033, and (d) 0.1 at 600 ^{o}C under carrier gas of 600 sccm

With increasing WR_{Ga} (WR_{Ga}=0~0.1), the nanostructure morphology became to be more irregular as shown in the Fig. 4.7. From EDX measurement, the Ga-content was detected 0 at.%, 0.06 at.%, 0.11 at.%, and 0.28 at.% as WR_{Ga} increases. One of the most important reasons on irregular structure of ZnO:Ga nanostructures is non-unifomity of Ga vapor pressure. As mentioned previously, the particle size of Ga and Zn powder is each 850 μm and 75 μm. At the growth temperature of 600 °C, Ga (melting temperature; 29.8 °C) gets easily to be segregated, which results in the non-uniform vapor pressure of Ga. This hinders to obtain uniform nanostructures.

4.6.2 Optical and electrical properties

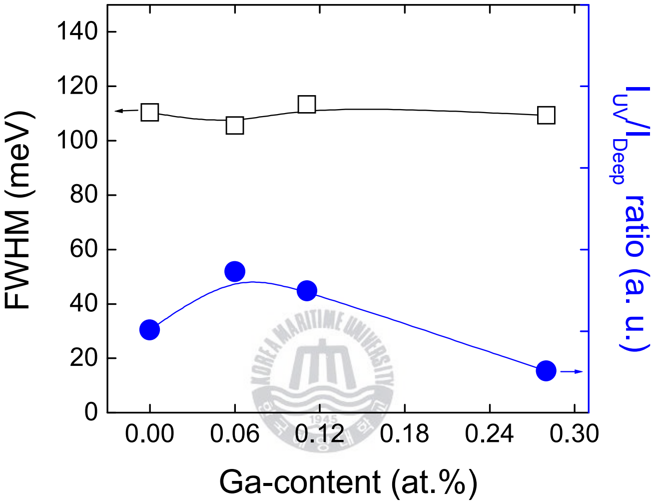

Fig. 4.8 PL spectra of ZnO:Ga nanostructures

Fig. 4.8 is PL spectra at room temperature of ZnO:Ga nanostructures. It was not shown the significant degradation in the FWHM value. Moreover, rather luminescence intensity by Ga-doping increases up to 0.11 at.%. Doping-related behavior has been reported in low-temperature PL spectra of Ga-doped ZnO epitaxial films [49,50] where a Ga-donor bound-exciton complex has been proposed to be responsible for the increase of PL intensity from Ga doping. The dominant peak (~ 3.35 eV) could be related to the Ga donor in view of its contribution to the NBE emission at room temperature. Therefore, at low or moderate Ga doping levels, the increase of PL intensity is primarily caused by the increase of the impurity emission presumably due to an increased carrier concentration by Ga-dopant. However, in heavily Ga-doped ZnO nanostructures, the competition between the two processes, that is, radiative and nonradiative transitions, becomes prominent. Excess Ga atoms can create nonradiative recombination centers, such as impurity complexes likely involving native defects, or impurity-assisted nonradiative transition channels, resulting in a reduction of the NBE luminescence. Hall measurement was performed to estimate extrinsic carrier concentration of the Ga-doped ZnO nanostructures as shown in the Fig. 4.9. It is shown the extrinsic carrier concentration is mostly proportional to the Ga-content despite irregular structure of ZnO:Ga nanostructure.

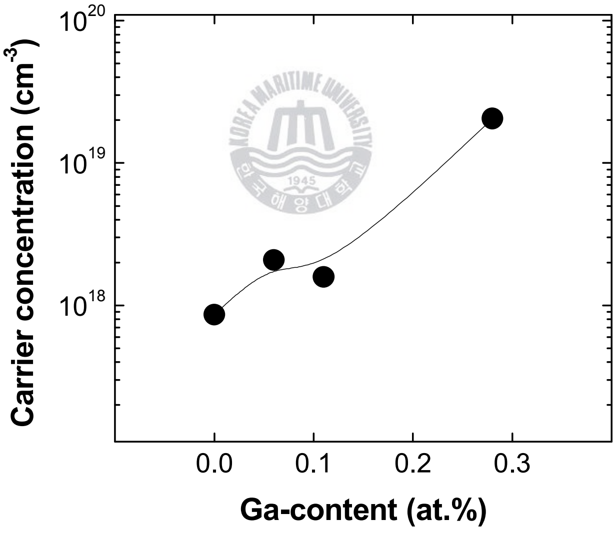

Fig. 4.9 Carrier concentration variation as a function of Ga-content in ZnO:Ga nanostructures

4.7 Characterization of integrated 1D In-doped ZnO nanostructures

4.7.1 Morphological variation and composition

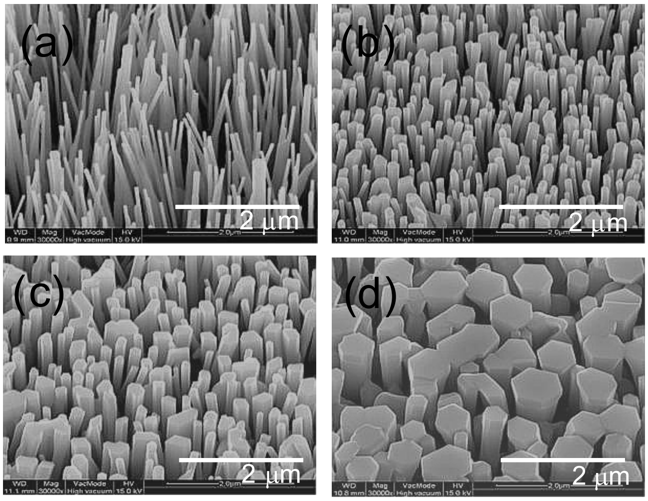

Fig. 4.10 SEM images of ZnO:In nanorods grown by different mixed source ratio, WR_{In} of (In/(In+Zn)) (a) 0 (b) 0.048 (c) 0.061, and (d) 0.1 at 600 ^{o}C under carrier gas of 600 sccm

With increasing In-content, the nominal length (*L*) and diameter (*D*) of ZnO:In nanorods are varied from *L*=4 μm and *D*=68 nm (WR_{In}=0) to *L*=0.9 μm and *D*=190 nm (WR_{In}=0.1). Over all, uniform rod type except for diameter increase was grown in ZnO:In nanostructures as shown in the Fig. 4.10. The nanorods of *L* clearly decreases with increasing their *D* and In-composition. The In-compositions of the samples are measured as 0, 0.12, 0.27, and 0.33 at.%, respectively. The data was expressed as a average value from 5 time measurements at each position.

4.7.2 Optical property and electrical properties

Fig. 4.11 shows the room temperature PL spectra, overall strong emission of NBE peak and weak green emission were observed. As shown in the inset of Fig. 4.11, the NBE emission position was shifted from 3.237 eV to the high-energy side as In-composition increases, and the NBE emission intensity decreased. Usually the variation of luminescence properties of n-type ZnO without a considerable structural change has been explained in terms of metallic transition due to an increase of extrinsic carrier.

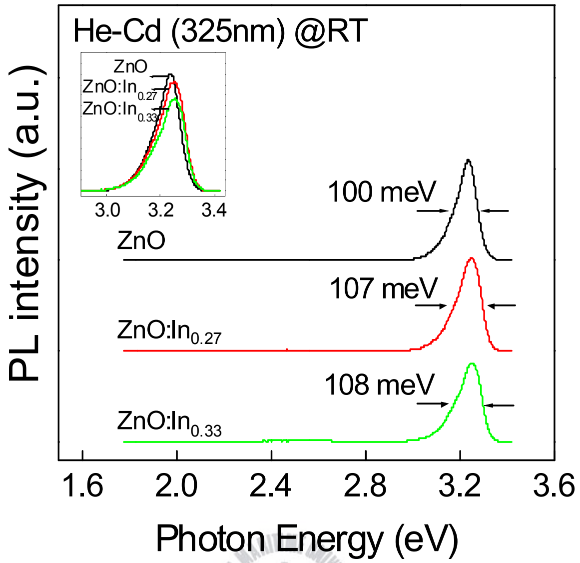

Fig. 4.11 PL spectra of ZnO:In nanorods

According to the semiconductor-metal transition theory, optical band gap (E_g) increases only when the impurity concentration is kept under the Mott critical density [51] and when the impurity concentration reached the Mott density the E_g decreases reached the Mott density the E_g decreases abruptly. Therefore, the blueshift of NBE emission position is tentatively attributed to the increase of In-concentration due to an increase of extrinsic carrier concentration but the impurity concentration is still within the Mott density. Note that when the high density of carriers have, screening between the carriers will happen by the wave-function overlapping of each carrier, also the carriers will scatter excitons. Similar result has been reported by Chen *et al* [52]. They ascribed the NBE emission intensity decrease of ZnO after In-doping due to the decrease of exciton binding energy. They explained that In acts as a scattering center of exciton and generates the screened Coulomb potential field, which makes excitons ionized owing to losing the Coulomb interaction.

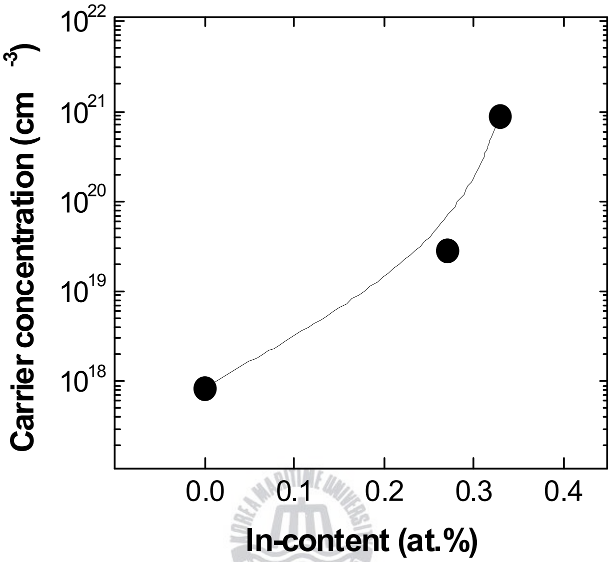

Fig. 4.12 Carrier concentration variation as a function of In-content in ZnO:In nanorods

Hence, the decrease of NBE emission intensity is interpreted as indicating the increase of extrinsic carrier concentration in the sample. As the In-doping increases, the enhanced free carrier concentration was confirmed by hall measurement as shown in the Fig. 4.12.

4.8 Growth mode of In-doped ZnO nanostructures

Fig. 4.13 shows the side-view SEM images of ZnO:In*x* nanorods: (a) x= 0, (b) x= 0.27, and (c) x= 0.33. The respective insets are the 30^{o} inclined images. With increasing In-content the nominal length L and diameter D of ZnO:Inx nanorods vary from L= 4 μm and D= 68 nm (x = 0 at.%) to L= 0.9 μm and D= 190 nm (x = 0.33 at.%). It has been found that the nanorod length L decreases as their diameter D increases.

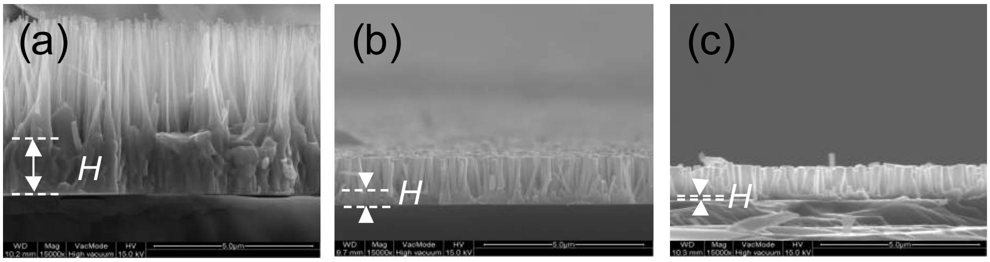

Fig. 4.13 Cross-sectional SEM inspections of ZnO:In nanostructures; (a) ZnO (b) ZnO:In$_{0.27}$, and (c) ZnO:In$_{0.33}$ nanorods

The usual explanation of nanorod growth is the so-called VLS mechanism [18]. In the VLS mechanism, nanorods (≈ whiskers) are assumed to grow due to the adsorption of vaporized atoms on the drop surface and their transfer to the crystal phase due to the solidification of liquid alloy on the crystal surface under the drop. The higher growth rate of rods (≈ whiskers) in the VLS mechanism is explained by a faster chemical reaction or better adsorption on the liquid surface and a faster nucleation of crystal phase from the liquid drop. Since the initial eutectic drops usually have a broad size distribution and the whisker lateral size is usually of the order of drop size. The lateral size dependence of the normal growth rate of whiskers has been studied experimentally by many authors [53,54]. In VLS growth, it has been found that the whisker length L normally increases with their diameter D, therefore, thicker whiskers grow faster than thinner ones. Note that it is clearly opposite to our observation.

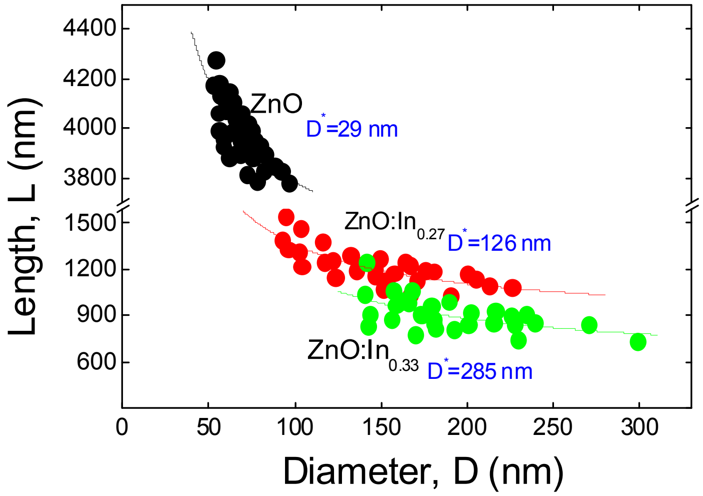

Fig. 4.14 Relationship of the nanorods between length (*L*) and diameter (*D*)

As shown in the Fig. 4.14, the measured $L(D)$ dependence was an inversely proportional relation $L \propto A/D$. Such $L(D)$ dependence is known due to the diffusion-induced (DI) growth of whiskers that was investigated theoretically and experimentally by several authors for molecular beam epitaxy and chemical vapor deposition of nano-whiskers [27,55]. The DI growth is known to be controlled by the diffusion of adatoms toward the whisker top along their side facets. It implies that the drop of a liquid alloy on the top of whisker may be quite an attractor for the adatoms. Although the DI growth of whiskers with additional impurity atoms has not been studied yet, impurity atoms may affect large influence on the whisker growth. Since the impurity atoms generally have different sticking coefficient and migration length in comparison with the host atoms.

The experimental $L(D)$ relationship is analyzed by using DI growth model. Solid lines in the right-hand side graph of Fig. 4.14 are fitted lines by using Eq. (1) [56];

$$L = \left(c + \frac{D^*}{D}\right)H \qquad (1)$$

As the In-content increases, the effective thickness (*H*) is decreased but characteristic diameter (D^*) is increased. The nominal length of nanorods is about 4 or 5 times longer than the *H*. This fact indicates that the growth of ZnO nanorods is governed by the adatom diffusion [27]. Also, the increase of characteristic diameter D^* with increasing In-content can be explained in terms of the DI growth model. Major factors related to the D^* are total deposition rate (V) and equilibrium adatom coverage of the surface (θ_{eq}), as shown in Eq. (2) [27]:

$$D^* = \frac{\theta_{eq} l_s}{V t_s} \sigma \qquad (2)$$

where l_s is the length of adatom diffusion, σ is adatom supersaturation rate, t_s is characteristic time between two consecutive jumps during migration. Equation (2) clearly shows that when we have an adatom with higher sticking coefficient, D^*. will increase. Moreover, the D^*elongates the nominal diameter of nuclei at the initial growth stage, the nominal diameter *D* of rods would be increased when D^* increases. The discussed DI growth model for ZnO:In nanorods is illustrated in the Fig. 4.15. From the phase diagram of AuGe [57] the eutectic melting point of it ($Au_{1-x}Ge_x$, x ~43 at.%) is estimated to be 550 $^{\circ}$C. Therefore, at the growth temperature of nanorods (600 $^{\circ}$C), AuGe would form the liquid droplets on surface by surface tension. On the droplets and substrate surface, In and Zn atoms of the gaseous phase are simultaneously impinged (Fig. 4.15(a)). Since In atoms have lower vapor pressure than Zn atoms, the characteristic diameter D^* would be increased with increasing In composition, simply because it is directly related to the number of deposited particles in the surface (Fig. 4.15(b)). The details on the growth mode and morphological variations will be discussed elsewhere [58].

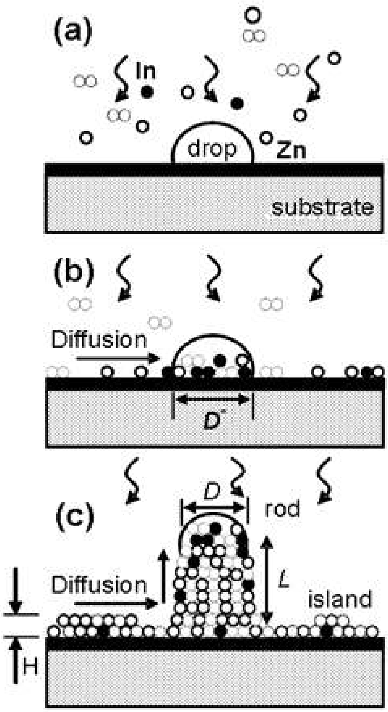

Fig. 4.15 Schematic illustration of diffusion-induced growth mode for ZnO:In nanorods.

KOREA MARITIME UNIVERSITY
1945
한국해양대학교

4.9 In-induced physical phenomena

4.9.1 Variation of surface excitonic emission

Fig. 4.16 shows the low-temperature PL spectra of ZnO and ZnO:In nanorods. The peak of ultraviolet (UV) emission at 3.354 eV is highest in the PL spectrum, and green emission band is relatively negligible. That results mean that the crystal quality of the sample is good.

The inset of Fig. 4.16 shows the PL intensity and full width at half maximum (FWHM) values for those samples. The peak at 3.354 eV was temporally assigned to a donor-related bound exciton emission (DBX) and will be discussed further. The PL intensity decreased with increasing In-content. Usually, the degradation of crystal quality accompanies the decrease of PL intensity. Since the crystal quality degradation increases the inhomogeneity of specimen and the inhomogeneity of the specimen provokes the dispersion of local minimum states, the PL linewidth will broaden. However, considerable FWHM broadening was not observed from this experiment. The FWHM was estimated to be 13.3 meV (ZnO), 10.7 meV (ZnO:In$_{0.27}$), and 10.4 meV (ZnO:In$_{0.33}$). This fact supports that the decrease of observed PL intensity cannot be simply attributed to the degradation of crystallinity.

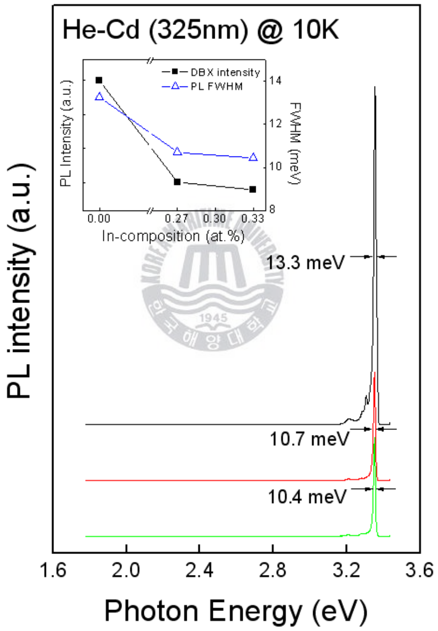

Fig. 4.16 Low-temperature (10 K) PL of ZnO and ZnO:In nanorods. The inset shows integrated PL intensity and FWHM of DBX.

The responsible reason for the decrease of PL intensity seems to be explained in terms of In-addition. Chen et al. reported on the In-induced optical band gap shift and quenching of near-band edge luminescence line at room temperature [59].

They attributed those evolutions to the scattering of excitons by ionized In-impurity. However, in case of this low-temperature PL spectra, considerable effect by ionized impurity is hardly expected due to low measurement temperature (10 K); hence, blue shift of the DBX was not observed. The other In-induced obvious evolution is a decrease of surface to volume (*S/V*) ratio. The nominal rod diameter was increased from 68 to 190 nm, with increasing the In composition from 0 to 0.33 at.%. This fact means considerable decrease of the *S/V* ratio by In-incorporation. Here, it should be pointed out that the decrease of *S/V* ratio could have considerable effect on the luminescence intensity of nanostructured ZnO. Generally speaking the PL intensity is determined by an efficiency and volume of luminescence; more quantitatively, it can be expressed as,

$$I_{PL} = \int_{volume} \sqrt{hv - E_g}\, exp(-\frac{hv - E_g}{k_B T})$$

where hν is a photon energy of excitation light, E_g is an energy gap, k_B is the Boltzmann constant, and T is an absolute temperature. I assume that PL of a nanostructure mainly reflects the information of near the surface region when the PL under weak excitation happens within the nominal extinction length of excitation light. In the case of ZnO, text is 50−70 nm by using the absorption coefficient of 2×10^5−1.5×10^5 cm^{-2} evaluated by Muth et al [60]. Hence, if I consider an nanorod with fixed length and a smaller diameter than text, an increase of rod diameter will be reflected in terms of an increase of PL intensity mainly due to an increase of luminescence volume. In this experiment, the effective volume of luminescence for those nanorods (a volume which participate in the luminescence) was estimated to be 0.61 μm^3 (ZnO), 0.17 μm^3 ($ZnO:In_{0.27}$), and 0.05 μm^3 ($ZnO:In_{0.33}$). Therefore, the decrease of S/V ratio tentatively attributed to the decrease of PL intensity, although it requires more discussion.

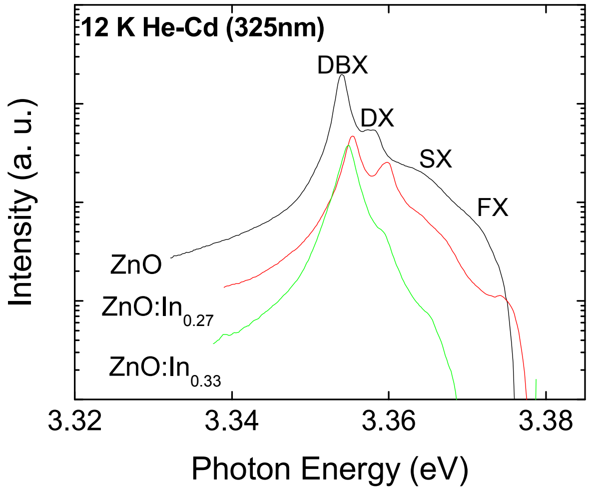

Fig. 4.17 NBE emission lines of ZnO:In nanorods at low temperature

The other result that should be interpreted in terms of the In-doping. I have measured an excitation power dependence of near-band-edge (NBE) emission lines. Fig. 4.17 shows an low temperature PL spectra for ZnO and ZnO:In nanorod samples. The NBE emissions were assigned to surface exciton (SX; 3.365 eV) and donor-boundexciton lines (DX; 3.357 eV (I_9) and DBX; 3.354 eV) based on the reported peak positions [42,61].

It has been well known that excitation power dependence of PL can be analyzed by the simple relationship between the excitation power (L) and the luminescence intensity (I_{PL});

$$I_{PL} = L^{\alpha},[62]$$

where L is the excitation power and a is an exponent. The coefficient a is generally $1 < a < 2$ for the free- and bound-exciton lines within less than three orders of L, and when the excitation energy is tuned to the semiconductor gap the coefficient a for the free exciton becomes equal to 1.

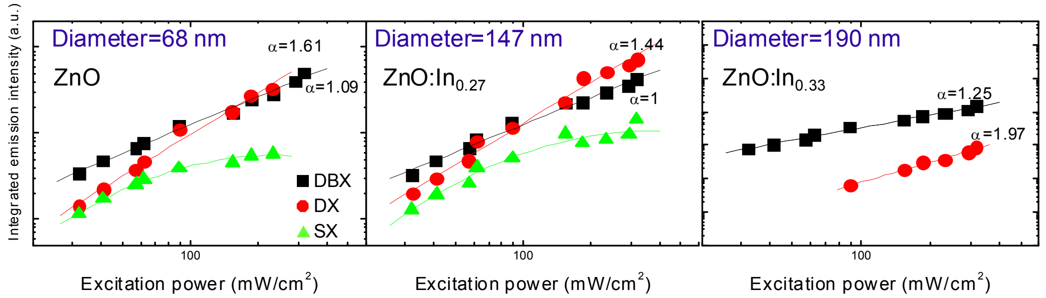

Fig. 4.18 Evolution of integrated intensity of DBX, DX, and SX lines according to excitation power

As shown in the Fig. 4.18, the *a* values for each DBX line are estimated to be 1.09 (ZnO), 1.00 (ZnO:In$_{0.27}$), and 1.25 (ZnO:In$_{0.33}$). Also the *a* values for DX lines are 1.61 (ZnO), 1.44 (ZnO:In$_{0.27}$), and 1.97 (ZnO:In$_{0.33}$). Those results clearly show that those lines are closely related with a shallow impurity bound exciton.

The DX line is well known as an In-donor bound exciton (I_9) [42]. I could observe DX line from ZnO nanorod presumably due to unintentional doping. DX intensity considerably increased for ZnO:In$_{0.27}$ and it collapsed for ZnO:In$_{0.33}$. The evolution of DX line can be regarded as a general feature of impurity bound exciton. An increase of impurity density will increase the PL intensity within a certain impurity concentration; however, further increase in impurity density will degrade the crystal quality by increasing an inhomogeneity. Therefore, bound exciton emission will collapse.

Although the peak position of DBX is very close to the I_{10}, but it is still unclear. However, the evolution of DBX intensity could be explained in terms of *S/V* ratio. This fact suggests a possibility that DBX is a neutral-donor defect complex (NDC) [42,63]. Reynolds *et al.* have reported that the NDC lines (3.35~3.365 eV) have the properties of neutral donors and the optical transitions result from the collapse of excitons bound to the neutral donors. Moreover, by the annealing high-energy side peaks shift toward lower-energy side but the total intensity is conserved. Their observations can be interpreted in terms of a radiative recombination between a shallow impurity bound exciton and a defect at the surface region. Therefore, the DBX line is assigned to a neutral-donor defect complex emission.

Also, Fig. 4.18 provides an evidence for the assignment of SX lines. It is well known that due to a limited density of surface state, SX shows fast saturation behavior. The surface exciton intensity (SX: 3.365 eV) decreased and finally it becomes negligible when the In-composition reached 0.33 at.% presumably due to the decrease of *S/V* ratio. Also it is a matter of fact that the surface states will be affected by the impurity on the surface; hence, the SX intensity should also be affected by In-incorporation. Although discussion on the NBE emissions in terms of the impurity incorporation requires more rigid inspections such as time and spatially resolved PL, if we assume that the incorporated In-atoms make an inhomogeneous localized state, temperature-dependence PL will reflect the inhomogeneity of the specimen.

4.9.2 Inhomegeneity in the doped ZnO nanostructures

Fig. 4.19 reveals temperature-dependence PL spectra of ZnO and ZnO:In nanorods. It shows the evolution of NBE (3.35~3.37 eV), two-electron satellite (TES; 3.31 eV) of DX, and donor-acceptor pair (DAP; 3.23 eV) lines of ZnO nanorods. Fig. 4.19(a) shows very close feature to our previous result [64] on the temperature-dependence PL of ZnO tetrapods. The TES line shows weak luminescence intensity at low temperature; however, it increases along with the PL measurement temperature (T_{PL}) increase and finally merged into bound exciton lines. DAP line also shows similar thermal quenching behavior. With increasing the temperautre of PL, the DAP line excited to free-to-bound transition (eA_0) line. Those lines merged into one broad emission band centered at 3.24 eV at high-temperature region. And I determined not to discuss on ZnO nanorods in detail. However, the origin of dominant lines (DBX) for ZnO:In nanorods (Figs. 4. 19(b-c)) should be considered.

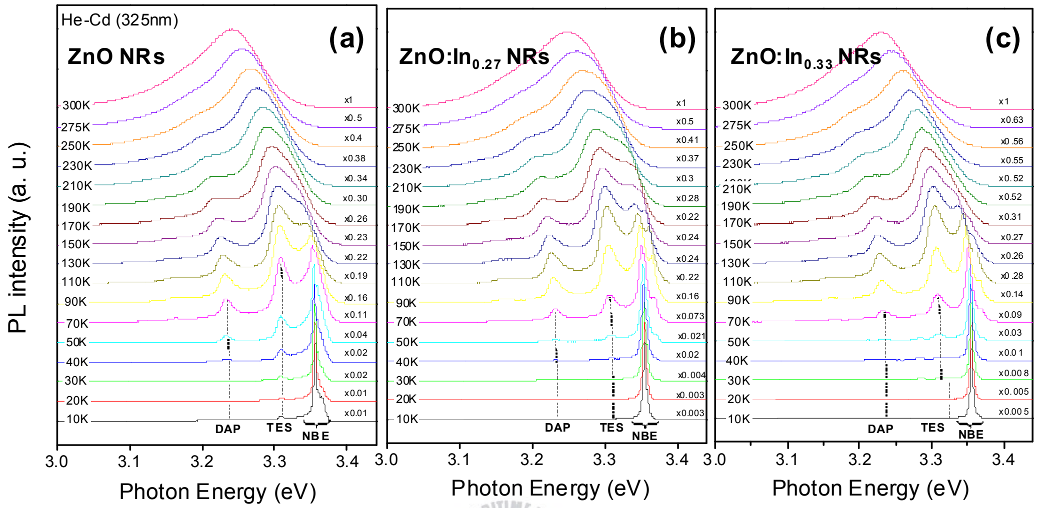

Fig. 4.19 Temperature-dependence PL spectra for (a) ZnO, (b) ZnO:$In_{0.27}$, and (c) ZnO:$In_{0.33}$ nanorods

The donor binding energy shows a linear relationship with the bound exciton localization energies; E_{loc}= (E_{FX}-E_{DX}) known as Haynes rule E_{loc}= αE_D. More generally, E_{loc} is given by the following equation:

$$E_{loc} = A + B \times E_D$$

In case of high quality ZnO, A and B were evaluated to be -3.8 meV and 0.365 for bound excitons in ZnO. When I consider the donor binding energy of In (63.2 meV) [42] then the E_{loc} for In is calculated to be 19.2 meV [65]. The thermal activation energy of DBX lines for both ZnO:In nanorods was evaluated to be 12.6 meV (ZnO:$In_{0.27}$) and 14.9 meV (ZnO:$In_{0.33}$), which do not correspond with the above estimation. It may be primary due to the negative thermal quenching (NTQ) of DBX lines.

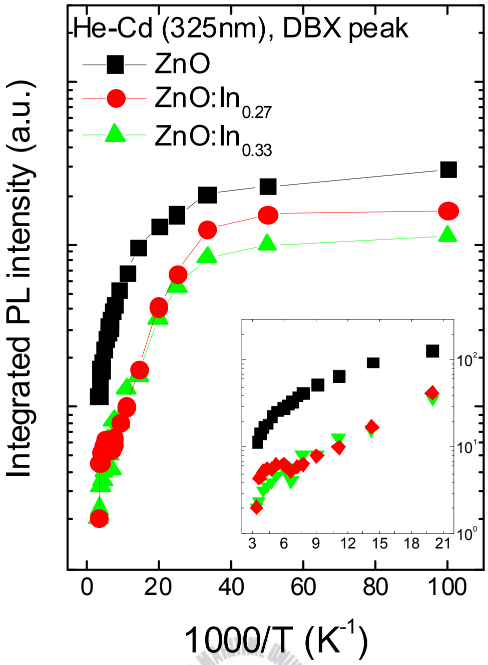

Fig. 4.20 Thermal quenching spectra of DBX lines

Fig. 4.20 shows the temperature-dependence PL intensity variation of ZnO and ZnO:In samples. From the ZnO:In samples, NTQ was observed in the $5.8 < 1000/T < 6.7$ region. The NTQ phenomenon was explained as follows: when the radiative recombination happens in a system with a plural multi-level between initial (excited state) and final (ground state) levels, thermally activated carriers will recombine via intermediate states [40]. If the DBX is related with a defect and a donor bound exciton as Reynolds *et al.* argued that DBX would have an intermediate transition state. Also a shallow state will be thermally activated first. Hence the inconsistency of estimated DBX activation energy is regarded as the evidence that the DBX is not simply related with In impurity but probably related with a defects concentrated near the surface of nanorods. However, it should be mentioned that NTQ has been observed mainly from the doped-semiconductors such as n-type GaAs [36] and n-type ZnS [37], but some report revealed that structural defect could be an origin of NTQ [66]. Although there is a controversy in those reports, all reports indicate that an increase of inhomogeneity in the sample is closely related with the phenomenon. TES line provides valuable information on the shallow donor impurities. In a simple hydrogen like effective mass approach the energy separation between n= 1 and 2 states would be equal to 3/4 of the donor binding energy (63.2 meV) [42]. This simple approximation provides a two-electron separation of 47.4 meV, but it was observed at 50.6 meV low-energy side from the DX [42] In our case, the TES separation for each sample was evaluated to be 49.9 meV (ZnO:In$_{0.27}$) and 46.4 meV (ZnO:In$_{0.33}$), which supports our assignment.

4.10 Summary

In this chapter, to dope group III-metal impurity (M=Al, Ga, and In) in the integrated 1D ZnO nanostructures, the growth condition was fixed by controlling various growth parameters. Morphological variation, structural, optical and electrical properties of the M-doped ZnO nanostructures grown under the consistent growth condition were investigated. Doping induced the increase of extrinsic carrier concentration and morphology change of nanostructure. First of all, ZnO:In nanorods turned out to have excellent physical properties in terms of structural, optical, and electrical properties. Especially, the growth mode of doped ZnO nanostructure was newly interpreted as diffusion-induced model. Futhermore, various properties, such as SX emission decrease due to *S/V* ratio change and NTQ effect originated from In-inhomogeneity, related the In-doped ZnO nanostructures were found out.

References

[1] R. Konenkamp, R.C.Word, C. Schlegel, Appl. Phys. Lett. 85 6004 (2004)

[2] M.H. Huang, S. Mao, H. Feick, H. Yan, Y. Wu, H. Kind, E. Weber, R. Russo, P. Yang, Science 292 1897 (2001)

[3] J.-H. Choy, E.-S. Jang, J.-H. Won, J.-H. Chung, D.-J. Jang, Y.-W. Kim, Adv. Mater. 15 1911 (2003)

[4] Q.H. Li, Y.X. Liang, Q.Wan, T.H.Wang, Appl. Phys. Lett. 85 6389 (2004)

[5] X. Wang, J. Zhang, Z. Zhu, Appl. Surf. Sci. 252 2404 (2006)

[6] S. Ju, K. Lee, D.B. Janes, M.-H. Yoon, A. Facchetti, T.J. Marks, Nano Lett. 5 2281 (2005)

[7] M. Law, L. Greene, J.C. Johnson, R. Saykally, P.Yang, Nat. Mater. 4 455 (2005)

[8] Z.W. Pan, Z.R. Dai, Z.L. Wang, Science 291 1947 (2001)

[9] C.H. Liu, J.A. Zapien, Y. Yao, X.M. Meng, C.S. Lee, S.S. Fan, Y. Lifshitz, S.T. Lee, Adv. Mater. 15 838 (2003)

[10] C.H. Liu, W.C. Yu, F.C.K. Au, J.X. Ding, C.S. Lee, S.T. Lee, Appl. Phys. Lett. 83 3168 (2003)

[11] J.J. Wu, S.C. Liu, Adv. Mater. 14 215 (2002)

[12] K. Govender, D.S. Boyle, P. O'Brien, D. Binks, D. West, D. Coleman, Adv. Mater. 14 1221 (2002)

[13] Y.W. Wang, L.D. Zhang, G.Z. Wang, X.S. Peng, Z.Q. Chu, C.H. Liang, J. Cryst. Growth 234 171 (2002)

[14] H.T. Ng, J. Li, M.K. Smith, P. Nguyen, A. Cassell, J. Han, M. Meyyappan, Science 300 1249 (2003)

[15] S.Y. Li, C.Y. Lee, T.Y. Tseng, J. Cryst. Growth 247 357 (2003)

[16] P.X. Gao, Y. Ding, Z.L. Wang, Nano Lett. 3 1315 (2003)

[17] C.J. Lee, T.J. Lee, S.C. Lyu, Y. Zhang, H. Ruh, H.J. Lee, Appl. Phys. Lett. 81

3648 (2002)

[18] R.S. Wagner, W.C. Ellis, Appl. Phys. Lett. 4 89 (1964)

[19] E.I. Givargizov, A.A. Chernov, Kristallografiya 18 147 (1973)

[20] E.I. Givargizov, J. Crystal Growth 31 20 (1975)

[21] D.N. Mcllroy, A. Alkhateeb, D. Zhang, D.E. Aston, A.C. Marcy, M.G. Norton, J. Phys.: Condens. Matter 16 R415 (2004)

[22] V.G. Dubrovskii, N.V. Sibirev, Phys. Rev. E 70 031604 (2004)

[23] K. Hiruma, M. Yazawa, T. Katsuyama, K. Ogawa, K. Haraguchi, M. Koguchi, Appl. Phys. 77 447 (1995)

[24] D. Kashchiev, Nucleation: Basic Theory with Applications, Butterworth Heinemann, Oxford, 2000

[25] W. Obretenov, D. Kashchiev, V. Bostanov, J. Crystal Growth 96 846 (1989)

[26] L. Schubert, P. Werner, N.D. Zakharov, G. Gerth, F.M. Kolb, L. Long, U. Go sele, T.Y. Tan, Appl. Phys. Lett. 844 968 (2004)

[27] V.G. Dubrovskii, G.E. Cirlin, I.P. Soshnikov, A.A. Tonkikh, N.V. Sibirev, Y.B. Samsonenko, V.M. Ustinov, Phys. Rev. B 71 205325 (2005)

[28] G.E. Cirlin, V.G. Dubrovskii, N.V. Sibirev, I.P. Soshnikov, Y.B. Samsonenko, A.A. Tonkikh, V.M. Ustinov, Semiconductors 39 557 (2005)

[29] M. Schmeits, A. Mazur, J. Pollmann, Phys. Rev. B 27 5012 (1983)

[30] R. Dorn, H. Luth, M. Buchel, Phys. Rev. B 16 4675 (1977)

[31] M.M. Woolfson, J.M. Ziman, Introduction to the Theory of Solid Surfaces, Cambridge University Press, London, P186 1979

[32] X.L. Wu, S.J. Xiong, G.G. Siu, G.S. Huang, Y.F. Mei, Z.Y. Zhang, S.S. Deng, C. Tan, Phys. Rev. Lett. 91 157402 (2003)

[33] A. Puzder, A.J. Williamson, F.A. Reboredo, G. Galli, Phys. Rev. Lett. 91 157405 (2003)

[34] I. Ivanov, J. Pollmann, Phys. Rev. B 24 7275 (1981)

[35] E.W. Williams, J. Emery, in: R.K. Willardson, A.C. Beer (Eds.), Semiconductors and Semimetals, vol. 8, Academic Press, New York, London, 1972, pp. 321. 387

[36] T. Yokogawa, T. Taguchi, S. Fujita, M. Satoh, IEEE Trans. Electron Devices 30 271 (1983)

[37] E.H. Bogardus, H.B. Bebb, Phys. Rev. 176, 993 (1968)

[38] M.W. Cho, T. Minegishi, T. Suzuk, H. Suzuki, T. Yao, S.K. Hong, H. Ko, J. Electroceram. 17 255 (2006)

[39] A.C. Rastogi, S.B. Desu, P. Bhattachary, S. Katiyar, J. Electroceram. 13 345 (2004)

[40] H. Shibata, Jpn. J. Appl. Phys. 37 550 (1998)

[41] M. Watanabe, M. Sakai, H. Shibata, C. Satou, S. Satou, T. Shibayama, H. Tampo, A. Yamada, K. Matsubara, K. Sakurai, S. Ishizuka, S. Niki, K. Maeda, I. Nikkura, Physica B 376 711 (2006)

[42] B.K. Meyer, H. Alves, D.M. Hofmann, W. Kriegseis, D. Forster, F. Bertram, J. Christen, A. Hoffman, M. Strasburg, M. Dworzak, U. Haboeck, A.V. Rodina, Phys. Stat. Sol.(b) 241 231 (2004)

[43] S. Y. Ha, M. N. Jung, S. H. Park, et al., J. Nanosci. and Nanotech. 6 3624 (2004)

[44] E. McGlynn, J. Grabo wska, and K.K. Nanda, Sur. and Coat. Tech. 200 1093 (2005)

[45] C. Andreazza, P. Andreazza, and D. Zhao, Superlatt. and Microstruct. 39 340 (2006)

[46] X. Wang, G. Li, Y. Wang, Chem. Phys. Lett. 469 308 (2009)

[47] H.W. Lee, S.P. Lau, Y.G. Wang, K.Y. Tse, H.H. Hng, B.K. Tay, J. Cyst. Growth 268 596 (2004)

[48] C. X. Xu, X. W. Sun et al, Appl. Phys. Lett. 84 1540 (2004)

KOREA MARITIME UNIVERSITY 1945

[49] H. J. Ko, Y. F. Chen, S. K. Hong, H. Wenisch, T. Yao, and D. C. Look, Appl. Phys. Lett. 77 3761 (2000)

[50] H. Kato, M. Sano, K. Miyamoto, and T. Yao, J. Cryst. Growth 237 538 (2002)

[51] N. F. Mott, Metal-Insulator Transitions (Taylor and Francis, London, 1974)

[52] Y. W. Chen et al., J. Chem. Phys. 123 134701 (2005)

[53] D. N. Mcllroy et al., J. Phys. Condens. Matter 16 R415 (2004)

[54] A. A. Tonkikh et al., Semiconductors 38 1217 (2004)

[55] G. W. Sears, Acta Metall. 1 457 (1953)

[56] V. G. Dubrovskii et al., J. Cryst. Growth 289 31 (2006)

[57] Landolt-B¨ornstein, Numerical Data and Functional Relationships in Science and Technology, Vol. 5 (Springer-Verlag, Berlin, 1994)

[58] M. N. Jung et al., App. Phys. Lett. 94 041906 (2009)

[59] Y. W. Chen et al., J. Chem. Phys. 123 134701 (2005)

[60] J. F. Muth et al., J. Appl. Phys. 85 7884 (1999)

[61] L. Wischmeier et al., Phys. Rev. B 74 195333 (2006)

[62] T. Schmidt et al., Phys. Rev. B 45 8989 (1992)

[63] D. C. Reynolds et al., Phys. Rev. B 57 12151 (1998)

[64] M. J. Jung et al., Physica E 40 2761 (2008)

[65] B. K. Meyer et al., Semiconduct. Sci. Technol. 20 S62 (2005)

[66] M. Watanabe et al., Appl. Phys. Lett. 86 221907 (2005)

Chapter 5. Field emission properties of doped ZnO nanostructures

5.1 Introduction

ZnO is one of the most intensively studied metal-oxide materials for application to nanostructures, due to the unique physical properties such as large exciton binding energy (60 meV) and direct wide band gap (3.44 eV at 0 K) [1]. Many studies have been performed on the synthesis [2,3] and characterization [4,5] of ZnO-based nanostructures [6–8]. Also, there have been numerous efforts to improve the device performance further [9,10]. For instance, it was reported that for a specific application such as field emitter, impurity doping is helpful to enhance the electron emission efficiency by increasing the conductivity of ZnO nanostructures [9,10]. It is well known that group-III metal atoms are efficient donor species for ZnO, and many studies have already been performed on the synthesis and characterization of group-III-doped ZnO nanostructures.

Xu *et al.* have reported on the field emission properties of Ga-doped ZnO nanofibers [10]. They attributed the enhancement of electron emissivity to the increase of conductivity and reduction of work function by Ga doping. Zhong *et al.* reported on the conductivity increase of Ga-doped ZnO nanotips [11]. However, not much has yet become known on the synthesis and application of In-doped ZnO (ZnO:In) nanostructures.

In this work, I aim to realized field emitter using ZnO:In nanostructure with various dimensions by using mixed-source vapor phase transportation (VPT), which has been investigated to prove the effect of impurity doping.

5.2 Theoretical background

5.2.1 Fowler-Nordheim theory

The emission of electrons from a metal or semiconductor into vacuum (or a dielectric) occurs under the influence of a strong electric field. In field emission, electrons tunnel through a potential barrier, rather than escaping over it as in thermionic or photoemission. The effect is purely quantum-mechanical, with no classical analog. It occurs because the wave function of an electron does not vanish at the classical turning point, but decays exponentially into the barrier (where the electron's total energy is less than the potential energy). Thus there is a finite probability that the electron will be found on the outside of the barrier.

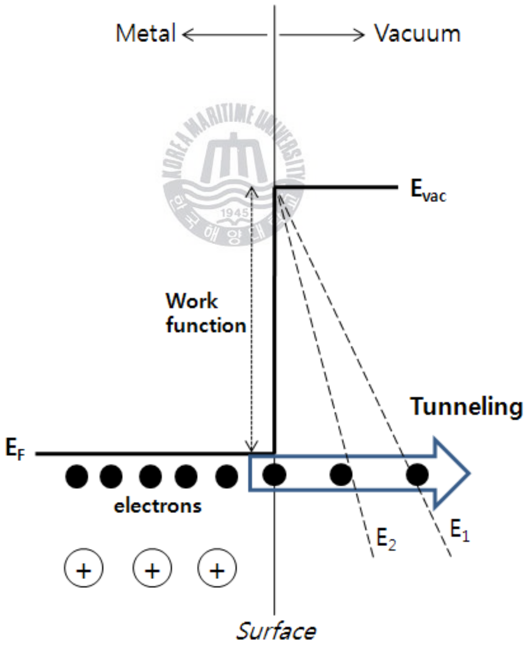

Fig. 5.1 Energy band diagram for metal; E_F: metal fermi level, E_{VAC}: vacuum level at metal surface. Dashed line represents the band diagram in the electric fields applied to metal ($E_1<E_2$).

For a metal at low temperature, the process can be understood in terms of the illustration. The metal can be considered as a potential box, filled with electrons to the Fermi level, which lies below the vacuum level by several electron-volts. The distance from Fermi to vacuum level is called the work function, Φ. The vacuum level represents the potential energy of an electron at rest outside the metal, in the absence of an external field. In the presence of a strong field, the potential outside the metal will be deformed along the line. so that a triangular barrier is formed, through which electrons can tunnel. Most of the emission will occur from the vicinity of the Fermi level where the barrier is thinnest.

Field emission- also called Fowler-Nordheim (F-N) tunneling [12], is the process where electrons tunnel through the surface potential barrier a metal-vacuum interface and float in the vacuum region during the presence of an extremely high electric field (Fig. 5.1). This quantum mechanical tunneling process is an important mechanism for thin surface potential barriers, just like those in highly doped semiconductor-metal junctions. The F-N model describes the tunneling current (I) as a function of the voltage applied between the cathode and anode (V); [12].

$$I/V^2 = a\exp(-b/V)$$

where $a = (\alpha A\beta^2/1.1\Phi)\exp[B(1.44\mathrm{x}10^{-7})/\Phi^{1/2}]$, $b = 0.95B\Phi^{3/2}/\beta$, $\beta = E/V$, $A = 1.54\mathrm{x}10^{-6}$ and $B = 6.87\mathrm{x}10^{7}$, α is the apparent emission area, β is the surface local field enhancement factor (geometric field enhancement factor), E is the electric field intensity at the surface, Φ is the electron work function of the emitter. All these parameters characterize electron field emission.

5.2.2 Factors related to the field emission property

Work function; Φ

Several physical quantities are important for determining the performance of field emission. Among them, an important physical quantity in electron field emission is the surface work function, which is well documented for elemental materials. For the emitters such as carbon nanotubes (CNTs), most of the electrons are emitted from the tips of the CNTs, and it is the local work function that matters to the properties of the CNT field emission. The work function measured from the ln(J/E^2) vs 1/E characteristics curve (the Fowler–Nordheim theory) [13].

By the previous studies, emission at very low applied fields only occurs for nanocrystalline diamond [14,15] carbon nanotubes [16,17] or nanoclustered sp^2 carbon [17,18]. In each case, emission appears to come from sp^2 sites such as the grain boundaries in nanocrystalline diamond [19-21]. These sites have a positive electron affinity. The barrier for emission is high, about 5 eV, the work function of graphite. However, emission over such large barriers requires a very strong local field of thousands of V/μm. Some groups have suggested that the materials with high energy band gap or doping result in the barrier energy decrease.

Field enhancement factor, β

The field enhancement factor is related to the slope of the F–-N plot, m, by the following equation [22].

$$\beta = \frac{(-6.83 \times 10^3 \phi^{3/2})}{m}$$

where ϕ is the work function of the emitter material. In the present case, the work function of ZnO (ϕ) is assumed to be 5.3 eV, which is reported to be independent of the size and aspect ratio of the nanostructure [23]. In the low-field region, it is identified to be directly dependent on the aspect ratio ratio of length to tip radius of the nanostructure [24]. In the context of F-N theory, the applied field is defined as F=βV, where V is the applied voltage V and β is the field enhancement factor (cm^{-1}). Further $\beta = 1/kr$, where k is a constant called as the geometrical factor and has the value 5 for hemispherical emitter, and r is the tip radius [12,25]. If the same factor is assumed in the two regions, the low-field region corresponds to emission from the conduction band of ZnO and the high-field region corresponds to an additional emission from the valence band, 3.37 eV below the conduction band.

Geometry of nanostructure

Schematic illustration of three micro- and nanostructures is shown in Fig. 3.

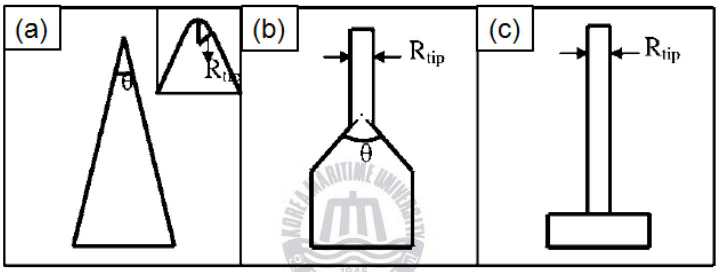

Fig. 5.2 Schematic illustration of the (a) agave-like structure, cone angle of 25° with tip of 25 nm (b) pencil-like structure, cone angle of 75° with tip of 70 nm, and (c) hierarchical structure, cone angle of 180° with tip of 70 nm

β is directly correlated with the geometry of emitter structures. The geometrical factor of micro- and nanostructures plays a crucial role in their field emission ability. Ku *et al.* demonstrated that the tip cone angle (Θ) and the tip radius (R_{tip}) are two important factors for the field emission property of emitter, i.e., small Θ and R_{tip} are beneficial to field emission [26]. By Yang *et al.* [27], they found that the geometry of the micro- and nanostructural emitters (Fig. 5.2) plays a crucial role in the field emission of

ZnO. Definitely, both Θ and R_{tip} of the agave-like structure are the smallest in three structures, and the values Θ of and R_{tip} of the pencil-like structure are smaller than that of hierarchical structure. The experimental β values for the samples (a-c) of Fig. 5.2 reveal 6041, 3461, and 514, respectively. These results indicate that the field emission of the agave-like structure seems to be the best among three structures.

The orientation of nanostructures has much influence on the field emission. Usually, nanostructures are vertically grown on substrates as the cathode will benefit for the field emission.

Surface states

Q. Zhao *et al.* [28] reported the field emission properties of the ZnO nanorods are considerably improved after annealing in oxygen and getting worse when annealing in air or ammonia. Surface states correlative with oxygen vacancy in ZnO nanorods may play a key role in determining the field emission performance. Thermal annealing can significantly reduce the surface oxygen vacancy concentration in ZnO nanorods. Oxygen chemisorption is predominant during the annealing in O-rich condition. The donor-like defects, such as oxygen vacancies or zinc interstitials, are self-compensated, and the related green emission intensity decreased [29]. They explain that the annealing in oxygen had better field emission properties due to its better crystallinity, lower work function, and increased conductivity.

5.3 Experimental

Experimental processes on the fabrication field emitter using 0D and 1D doped ZnO nanostructure is described in the Fig. 5.3.

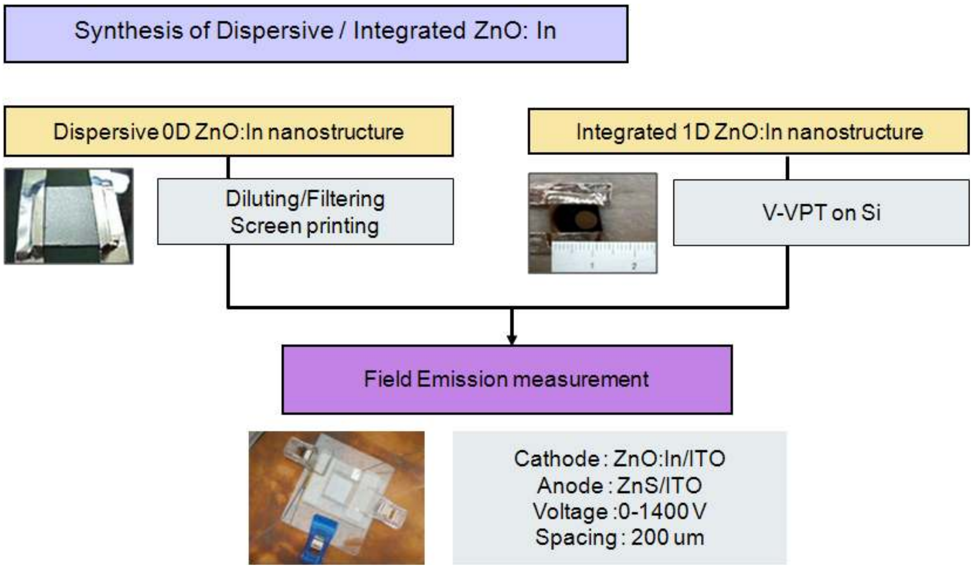

Fig. 5.3 Device fabrication process for field emitter

5.3.1 Fabrication process of dispersive 0D ZnO:In nanostructures

ZnO:In nanostructures with various indium content were synthesized by a vapor transportation technique with mixed-sources (Zn and In_2O_3 powders) by using a horizontal furnace. A reaction tube with a diameter of 31 mm was used. To control the In content of ZnO:In nanostructures, the weight ratio of source materials was controlled. The growth temperature was 1100 ^{o}C, and nitrogen with a flow rate of 300 ml/min was used as an ambient gas. The morphologies of ZnO:In nanostructures were investigated by scanning electron microscopy (SEM). To fabricate a field emission device (FED), the ZnO:In nanostructures were diluted in ethanol solution and then were sprayed on indium-tin-oxide (ITO) substrate. The FE measurement was performed in a vacuum chamber with a pressure of <1 x 10^{-6} Torr at room-temperature. The distance between two electrodes was estimated as ~200 μm and the measured emission area was 0.264 mm^2. The emission current was measured when applying a voltage up to 1400 V.

5.3.2 Fabrication process of integrated 1D ZnO:In nanostructures

ZnO:In nanorods were grown on AuGe/Si (111) substrates in horizontal tube furnace by V-VPT method. The weight ratio of the source materials (WR_{In}= In/In+Zn), WR_{In}=0~0.1) was varied by different WR_{In}. The growth temperature for ZnO:In nanorods was 600 °C under Ar gas flow of 600 sccm. The morphology of each sample was observed by a field emission scanning electron microscope (FE-SEM). Finally the field emission measurement was carried out in vacuum under 10^{-5} torr at room temperature. The indium tin oxide (ITO) glass was used as an anode. The nominal distance between cathode and anode was 200 μm. The current was measured by varying the applied voltage between the cathode and anode from 0 to 1400 V with 10 V step.

5.4 Field emission property of dispersive 0D ZnO:In nanostructures

Fig. 5.4 shows SEM images of ZnO and ZnO:In nanotetrapods. Sample A is pure ZnO, while sample B is ZnO:In TPs synthesized by a mixed source with a weight ratio (Zn/In_2O_3)~ 4.

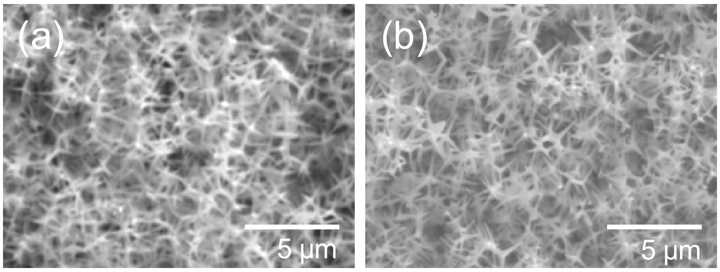

Fig. 5.4 SEM images of (a) sample A, ZnO nanotetrapods, (b) sample B, ZnO:In nanotetrapods with In content of 8 at.%

Sample A has a diameter of 88 nm and length of 830 nm. The nominal diameter and length of sample B are about 130 nm and 785 nm, respectively. Since the morphological variation of ZnO:In nanotetrapods has not been investigated in detail [30], qualitative discussion on the shape of ZnO:In nanotetrapodsis still difficult. However, generally the shape of the nanostructure is considered to be decided by Wulff construction [31] (Appendix A), which implies similar shapes from similar crystal structure. Therefore, I tentatively assigned the similarity of shape to substitutional incorporation of In atoms into the host lattice.

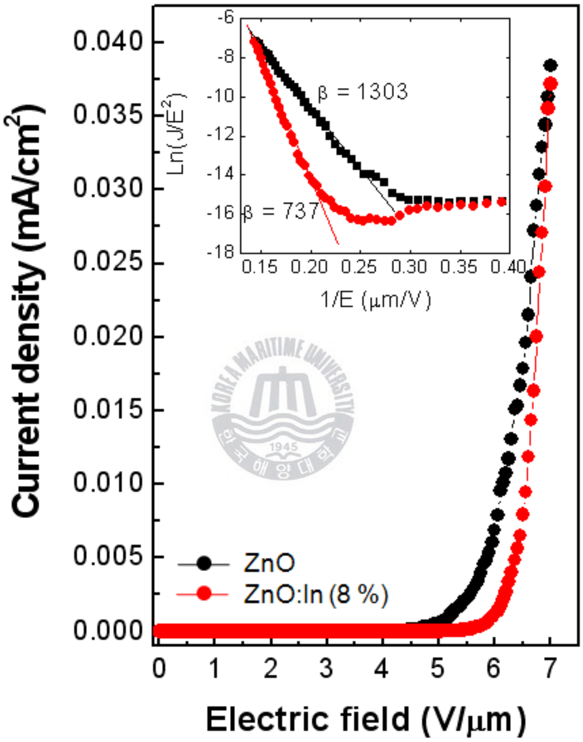

KOREA MARITIME UNIVERSITY
1945
한국해양대학교

Fig. 5.5 Field emission properties of ZnO and ZnO:In nanostructures (8 at.% In). The field enhancement factor (β) was estimated from the slope of Ln(J/E^2) against 1/E.

Fig. 5.5 shows a graph of emission current density against electric field from pure ZnO and ZnO:In nanostructures (In content of 8 at.%). The inset of Fig. 5.5

indicates the Fowler-Nordheim (FN) relationship of pure ZnO and ZnO:In nanostructures with In content of 8 at.%. The fitting was carried out by using the simplified FN equation [13]:

$$J=\frac{A\beta^2E^2}{\phi}exp(-\frac{B\phi^{3/2}}{\beta E})\ ,$$

where J is the current density, E is the applied field strength, u is the work function (5.3 eV for ZnO) and b is the field enhancement factor. A and B are constants of value 1.56 x 10^{10} (AV^{-2} eV) and 6.83 x 10^{3} (VeV$^{-3/2}$μm^{-1}), respectively.

In the case of ZnO and ZnO:In nanostructures (8 at.%), the threshold electric field (E_{th}) is estimated to be about 4.46 V/μm and 5.39 V/μm at a current density of 0.1 μA/cm^{2}, respectively. Also, the estimated β (β~ 737) for ZnO:In (8 at.%) nanostructures is almost comparable to a previous report [32], but considerably smaller than that of ZnO (β~ 1303). The FN equation indicates that a high field enhancement factor (β) and low work function (ϕ) are directly related with an increase of current density (J). Since a lowering of work function is presumable for ZnO:In nanostructures due to the increase of extrinsic carrier concentration, the relatively large threshold electric field should be attributed to the small field enhancement factor. The field enhancement factor β reflects the ability of the emitter to enhance the local electric field at the tip compared to the average macroscopic value [33]. Therefore, sharper and vertically well aligned tips are required to decrease the threshold electric field.

5.5 Field emission property of integrated 1D ZnO:In nanostructures

Fig. 5.6 is the morphology of ZnO:In nanorods. As In-content increases, the surface to volume (S/V) ratio is decreased from (a) 0.059 to (b) 0.028 and (c) 0.022 due to diameter increase and length decrease. Fig. 5.7 shows field emission properties of ZnO and ZnO:In nanorods (0.27 and 0.33 at.% of In). The E_{th} was defined as the E corresponding to the J of 0.1 μA/cm^2. The β values are shown in the inset of Fig. 5.7. The respective E_{th} of ZnO, ZnO:In (0.27 at.%), and ZnO:In (0.33 at.%) nanorods are estimated to be 5.17, 4.32, and 4.82 V/μm.

The ZnO:In nanorods show considerably low E_{th}. In case of the ZnO:In nanorods with 0.27 at.% of In the calculated β value of 1258 is most higher than other samples. As discussed above, those results could be obtained only when the effect of reduction overwhelms the increase of φ, and it strongly indicates the reduction of ZnO work function by In doping.

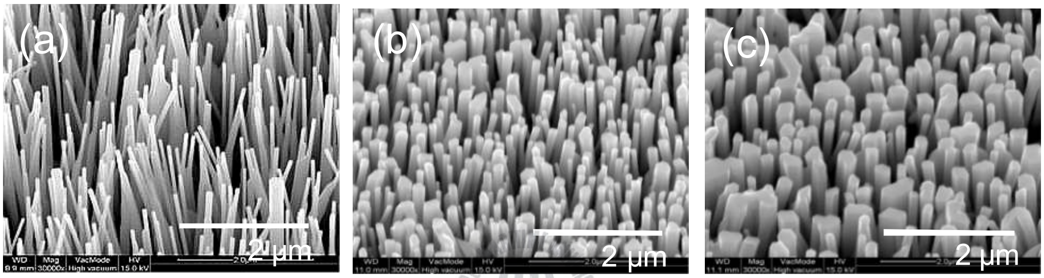

Fig. 5.6 SEM images of (a) ZnO, (b) ZnO:In (In~ 0.27 at.%), and (c) ZnO:In nanorods (In~ 0.33 at.%)

Table 5.1 Morphological properties and E_{th} variation In-doped ZnO nanostructure as a function of different dimensions

Dimensional	0-dimensional (0D)		1-dimensional (1D)		
Samples	ZnO	ZnO:In (8 %)	ZnO	ZnO:In (0.27 %)	ZnO:In (0.33 %)
Diameter, D [nm]	88	130	68	147	190
Length, L [nm]	830	785	3981	1218	908
Surface to volume (S/V) ratio	0.19	0.13	0.059	0.028	0.022
E_{th} [V/μm]	4.46	5.39	5.17	4.32	4.8

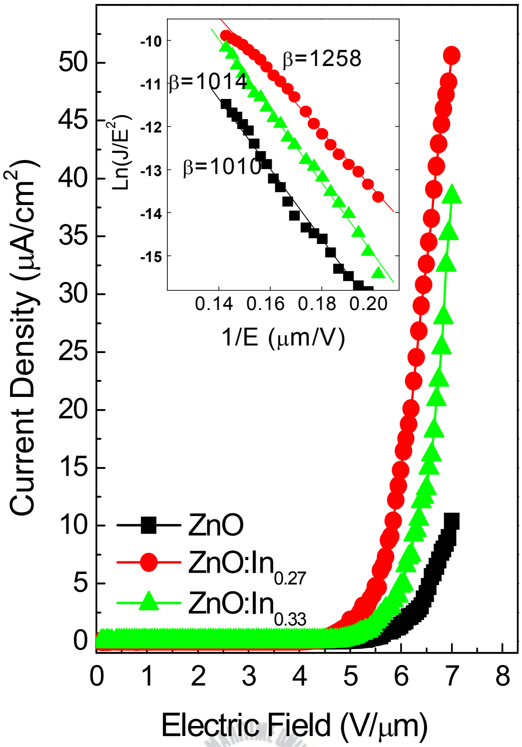

Fig. 5.7 Field emission properties of ZnO and ZnO:In nanorods (0.27 and 0.33 at.% of In). The field enhancement factor (β) was estimated from the slope of Ln(J/E^2) against 1/E (inset).

KOREA MARITIME UNIVERSITY 해양대학

5.6 Summary

Field emission properties are discussed from diverse ZnO:In nanostructures. Device performance is described in terms of structural (field enhancement factor; β) and electrical factors (work function; Φ) of doped ZnO nanostructures. The former indicates demerits induced by doping, while the later indicates enhancement of extrinsic carrier concentrations in the doped nanostructures.

References

[1] M.H. Huang, S. Mao, Feick et al, Science 292 1897 (2001)

[2] C.J. Lee , T.J. Lee, S.C. Lyu, Zhang et al, Appl. Phys. Lett. 81 3648 (2002)

[3] W.I. Park, Y.H. Jun, S.W. Jung and G.C. Yi, Appl. Phys. Lett. 82 964 (2003)

[4] Z.L. Wang, Mater. Today 7 26 (2004)

[5] J.H. Park, H.J. Choi, Y.J. Choi, S.H. Sohn et al, J. Mater. Chem. 14 35 (2004)

[6] J.H. Park, H.J. Choi and J.G. Park, J. Cryst. Growth 263 237 (2004)

[7] B.D. Yao, Y.F. Chen et al, Appl. Phys. Lett. 81 757 (2002)

[8] Y.C. Kong, Yu D.P. Yu, B. Zhang et al, Appl. Phys. Lett. 78 407 (2001)

[9] X.Y. Xue, L.M. Li, H.C. Yu, Y.J. Chen, Y.G. Wang, and T.H. Wang, Appl. Phys. Lett. 89 043118 (2006)

[10] C.X. Xu, X.W. Sun and B.J. Chen, Appl. Phys. Lett. 84 1540 (2004)

[11] C. Xu, M. Kim, J. Chun, and D. Kim, Appl. Phys. Lett. 86 133107 (2005)

[12] Y.W. Zhu, H.Z. Zhang, X.C. Sun, S.Q. Feng, J.Xu, Q. Zhao, B. Xiang, R.M. Wang, and D.P. Yu, Appl. Phys. Lett. 83 144 (2003)

[13] R.H. Fowler and L. . Nordheim, Proc. R. Soc. London, Ser. A 119 173 (1928)

[14] A.A. Talin, L.S. Pan et al, Appl. Phys. Lett. 69 3842 (1996)

[15] F. Lacher, C. Wild, D. Behr et al, Diamond Relat. Mater. 6 1111 (1997)

[16] W.A. deHeer, A. Chatelain, and D. Ugarte, Science 270 1179 (1995)

[17] W. Zhu, C. Bower, O. Zhou et al, Appl. Phys. Lett. 75 873 (1999)

[18] B.F. Coll, J. E. Jaskie et al, Mater. Res. Soc. Symp. Proc. 498 185 (1998)

[19] G.A.J. Amaratunga, M. Baxendale et al, New Diamond Frontier Carbon Technol. 9 31 (1999)

[20] O. Groning, O.M. Kuttel et al, J. Vac. Sci. Technol. B 18 665 (2000)

[21] A.V. Karabutov, V.D. Frolov, S.M. Pimenov, and V.I. Konov, Diamond Relat. Mater. 8 763 (1999)

[22] R. Gomer, Field Emission and Field Ionization, American Vacuum Society Classics (AIP, Woodbury, NY, 1993)

[23] Y.K. Tseng, C.J. Huang, H.M. Cheng et al, Adv. Funct. Mater. 13 811 (2003)

[24] X. Bai, E. G. Wang, P. Gao, and Z. L. Wang, Nano Lett. 3 1147 (2003)

[25] N. de Jonge, M. Allioux, J.T. Oostveen, K.B.K. Teo, and W.I. Milne, Phys. Rev. Lett. 94 186807 (2005)

[26] T.K. Ku, M.S. Chen, C.C. Wang, M.S. Feng, I.J. Hsieh, J.C.M. Huang, H.C. Cheng, Jpn. J. Appl. Phys., Part 1 34 5789 (1995)

[27] Y.H. Yang, B. Wang, N.S. Xu et al, Appl. Phys. Lett. S 89 043108 (2006)

[28] Q. Zhao, X.Y. Xu et al, Appl. Phys. Lett. 88 033102 (2006)

[29] J.D. Ye, S.L. Gu, S.M. Zhu, F. Qin et al, J. Appl. Phys. 96 5308 (2004)

[30] S.Y. Bae, H.C. Choi, C.W. Na, J. Park, Appl. Phys. Lett. 86 033102 (2005)

[31] A.W. Adamson, A.P. Gast, Physical Chemistry of Surfaces (John Wiley & Sons, New York, 1997)

[32] C.X. Xu, X.W. Sun, Appl. Phys. Lett. 83 3806 (2003)

[33] Q. Zhao, H.Z. Zhang, Y.W. Zhu, S.Q. Feng, X.C. Sun, J. Xu, D.P. Yu, Appl. Phys. Lett. 86 203115 (2005)

Chapter 6. Summary and Conclusion

In this study, investigation on growth and characterization of group III-metal elements (M=Al, Ga, and In) doped ZnO nanostructures has been performed. Growth of doped ZnO nanostructure with various dimensions (dispersive 0D-tetrapod and integrated 1D-rod) was accomplished. Doping was performed under consistent growth condition. Various physical property related to doping was investigated. Impact of doping on the nanostructures was studied by using field emitter.

Growth condition for dispersive 0D ZnO nanostructures was determined; The growth conditions like as growth temperature (900~1100 ^{o}C), Zn vapor pressure (0.05~0.2 g) and with/without graphite were considered for determination of growth condition. Dispersive 0D ZnO nanostructures grown at the growth temperature of 1100 ^{o}C using Zn amount of 0.05 g show the high quality crystallinity in terms of in structural and optical properties. Under the consistent growth condition (1100 ^{o}C, Zn amount 0.05 g), ZnO:Al doping by controlling WR_{Al} ratio in the range of 0~0.5 was tried, however it was not easy due to rapid Al-oxidation rate at the high growth temperature of 1100 ^{o}C. To increase Al-composition in nanostructures, graphite as the mixed source materials are used, which enhances the Al-doping, on the other hand it deteriorates the structural and optical properties. To grow ZnO:Ga nanostructures is used as the mixing source material not Ga but Ga_2O_3 powder with graphite. Synthesis was achieved in the full range from ZnO to Ga_2O_3 (WR_{Ga}; 0~1) The shape change and conductivity increase owing to Ga-doping were confirmed at the Ga-composition above 7.7 %. But, as Ga-composition increases brought about remarkable morphological deformation to the microstructures. ZnO:In nanostructures was achieved in the full range from

KOREA MARITIME UNIVERSITY

ZnO to In_2O_3 via adjustment of WR_{In} ratio (WR_{In}; 0~1). The high doping concentration (In < 35%) with the uniform morphology was accomplished and enhanced extrinsic carrier concentration was also confirmed.

Growth condition for integrated 1D ZnO nanostructures was determined; The growth conditions like as catalyst ($Au_{0.57}Ge_{0.43}$), growth temperature (550~700 °C), carrier gas flow (200~1000 sccm) were considered for control of growth condition. ZnO nanorods grown at the growth temperature of 600 °C under the carrier gas flow of 600 sccm show the high quality crystallinity in terms of in structural and optical properties. ZnO:Al doping by controlling WR_{Al} ratio in the range of 0~0.75 under consistent growth condition (600 °C, 600 sccm) was tried. As Al-composition increases, surface to volume (S/V) ratio was decreased. Fast degradation of optical properties by doping was observed, however, the increased extrinsic carrier concentration was revealed with increasing Al-composition. Ga doping was achieved by adjusting WR_{Ga} ratio (0~0.1). The morphology of Ga-doped nanostructures was not uniform as a function of Ga-composition, which causes non-uniformity of Ga flux. Although, the luminescence properties were enhanced in terms of negligible variation of FWHM value and luminescence intensity increase, the control of systematical carrier concentration was not observed. ZnO:In nanostructures with uniform rod type were grown by changing WR_{In} ratio (0~0.1). As In-composition increases, the extrinsic carrier concentration was increased and degradation of the optical property could be negligible by doping.

The growth mechanism of impurity doped nanorods has been newly interpreted as the diffusion induced growth mode. Also, doping induced various properties were observed by diverse optical properties; One was decrease of surface exciton (SX) emission related with decrease of S/V ratio, the other was negative thermal quenching phenomenon originated from the inhomogenous In-distribution in the nanostructure.

In conclusion, synthesis and characterization of 0D and 1D doped ZnO nanostructures were investigated. The former showed high dopant concentration and non-uniform morphology. In contrast, the latter requires strict growth condition control but it is apt to obtain uniform nanostructure.

The various physical properties and restrictions of doping were confirmed. Doping into a dispersive 0D nanostructure induces phase separation owing to the different bonding strength between host and dopant atoms and solubility limit. Also doping into a integrated 1D nanostructure is restricted by the decrease of surface to volume ratio. Such difference is deduced to come from the different total energy and growth mechanism of each nanocrystal.

Finally, field emitting devices were fabricated by using the doped dispersive/integrated nanostructures. The field emission property was influenced by the impurity doping. As a consequence, impurity doping enhances the electrical properties of nanostructures, however, it also restricts some properties by increasing the dimension of nanostructures.

Appendix. A Classical nucleation theory

The formation of nanopaticles (or nanocrystals) usually takes place via nucleation and growth stages. Nucleation of new particles from a continuous phase can occur heterogeneously or homogeneously [1]. Heterogeneous nucleation occurs on foreign nuclei or dust particles, ions, or surfaces. On the other hand, homogeneous nucleation occurs in the absence of such foreign objects. The free-energy changes associated with the process of homogeneous nucleation can be considered as follows: The overall excess free energy, ΔG, between a small solid particle of a solute and the solute in solution is equal to the sum of excess surface free energy, ΔG_S, that is, the excess free energy between the surface of the particle and the bulk of the particle, and the volume excess free energy, ΔG_V, that is, the excess free energy between a very large particle and the solute in the solution. ΔG_S is a positive quantity, the magnitude of which is proportional to square of the particle size (r^2). In a supersaturated solution, ΔG_V is a negative quantity proportional to r^3. Thus:

$$\Delta G = \Delta G_s + \Delta G_v = 4\pi r^2 \gamma + \frac{4\pi r^3 \Delta G_V}{3} \qquad (1)$$

where ΔG_V is the free-energy change per unit volume and γ is the interfacial tension between the developing crystallite surface and the supersaturated solution. The two terms on the right-hand side have opposite signs and depend differently upon r. Therefore, the free energy of formation, ΔG, passes through a maximum. This maximum value ΔG_{crit}, corresponds to the critical nucleus, r_c, and for a spherical cluster can be obtained by setting

$$\frac{dG}{dr} = 8\pi r \gamma + 4\pi r^2 \Delta G_v = 0 \qquad (2)$$

$$r_c = -2\gamma / \Delta G_v \qquad (3)$$

where ΔG_V is a negative quantity. From Equations (1) and(3) we get:

$$\Delta G_{crit} = 16\pi\gamma^3/3(\Delta G_v)^2 = 4\pi\gamma(r_c)^2/3 \qquad (4)$$

The behavior of a newly created crystallite depends on its size; it can either grow or redissolve via the reduction of free energy of the particle. The critical radius r_c represents the minimum size of a stable nucleus. Particles smaller than r_c will dissolve while the particles bigger than r_c will grow to achieve a reduction in the free energy. The above equation explains the formation of critical nuclei necessary for the formation of nanoparticles. The amount of energy (ΔG_{crit}) necessary to form critical nuclei arises from the local variation in energy of the fluid system due to the statistical distribution of molecular velocity in the molecules constituting the system. In the supersaturated regions, where the energy level rises temporarily to a high value, nucleation will be favored. The rate of nucleation J can be expressed in the form of an Arrhenius reaction rate constant, such as that commonly used for thermally activated processes.

$$J = A\exp(-\Delta G/kT)$$

where k is the Boltzmann constant. The basic Gibbs–Thomson relationship for a non-electrolyte is given by

$$\mathrm{In}\,S = 2\gamma\nu/kTr \qquad (5)$$

where S is the ratio of solution concentration to that of equilibrium saturation concentration at a given temperature; ν is the molar volume. This gives:

$$-\Delta G_v = 2\gamma/r = kT\ \ \mathrm{In}\ \ S/\nu$$

Hence, equation (4) becomes:

$$\Delta G_{crit} = 16\pi\gamma^3\nu^2/3(kT\ \ \mathrm{In}S)^2 \text{ and}$$

$$J = A\exp[-16\pi\gamma^3\nu^2/3k^3T^3(\mathrm{In}S)^2]$$

This equation indicates that three main variables govern the rate of nucleation: temperature T, degree of supersaturation S, and interfacial tension

γ.

Nuclei larger than the critical nuclei have a lower chemical potential than the precursors in the solution, and thus grow to bigger sizes at the expense of precursors. In analogy with the Gibbs–Thomson equation (Equation (5)), Peng *et al.* [2] observed that the solubility of crystals increases as the size of the crystal decreases. This plays an important role in determining the growth kinetics of the nanocrystals. If the monomer concentration in the solution is higher than the solubility of all the existing nanocrystals, then all of the nanocrystals in the solution grow and the size distribution narrows. This is known as the “focusing of size distribution”, which can be exploited for the formation of highly monodisperse colloidal nanocrystals. The depletion of the monomer by the growth of nanocrystals will eventually make the small nanocrystals in the solution soluble, due to strong size-dependent solubility in the nanometer regime. This means that the smaller nanocrystals in solution shrink and the bigger ones continue to grow. As a result, the size distribution broadens. This is “defocusing of the size distribution”, an effect also known as Ostwald ripening, and should be avoided for the formation of relatively monodisperse nanocrystals. The evolution of an ensemble of nanoparticles in a colloidal solution has also been studied theoretically, where the conditions leading to either "focusing" or "defocusing" of the particle size distribution were further determined [3]. The model described two general strategies to improve particle size distributions; First, to carry out experiments in a diffusion-controlled regime, presumably by decreasing the diffusion or mass-transfer coefficient of the system. Second, to increase the surface tension at the solvent–nanoparticle interface, for example, by a careful choice of surfactant. The crystal structure, size, and morphology of grown particles depends on the system and reaction parameters. These shapes occur either in order to minimize the surface energy of the particles or because of the kinetics of the growth. If kinetics dominates, then the shape is determined by the rate at which the different crystal faces grow. If the particles are formed in thermal equilibrium, their shape or crystal habit results from minimizing the surface energy. In the later case, the surface can be determined by performing a Wulff construction.

Appendix. B Free and bound exciton recombinations of ZnO crystals

High-quality ZnO crystals show pronounced neutral donor-bound exciton recombinations. In the following, we will focus on the recombination lines labelled I_4 to I_9. For the precise energy location see Table. I [4,5].

Table. I Energy positions of the free and neutral donor-bound exciton recombinations, their localization energies, the respective donor binding energies according to Haynes rule and the chemical identity where possible. ([a]A_L and A_T are the longitudinal and transversal free A-exciton states. A_T is the reference for the determination of the bound exciton localization energy. **I_2 and I_3 are assigned to ionised donor bound exciton recombinations.)

Line	Energy (eV)	Localization energy (meV)	Donor binding energy (meV)	Chemical identity
A_L[a]	3.3772			
A_T[a]	3.3759			
I_0	3.3725	3.4		
I_1	3.3718	4.1		
I_{1a}	3.3679	8.0		
I_2**	3.3674	8.5		
I_3**	3.3665	9.4		
I_{3a}	3.3660	9.9		
I_4	3.3628	13.1	46	H
I_5	3.3614	14.5	51.4	
I_6	3.3608	15.1		Al
I_{6a}	3.3604	15.5	53	Al
I_7	3.3600	15.9		
I_8	3.3598	16.1	54.5	Ga
I_{8a}	3.3593	16.6		
I_9	3.3567	19.2	63.2	In
I_{10}	3.3531	22.8	72.6	
I_{11}	3.3484	27.5		

References

[1] Cao Guozhong, Nanostructures and Nanomaterials - Synthesis, Properties and Applications, 2004 World Scientific

[2] X. Peng, L. Manna, W. Yang, J. Wickham, E. Scher, A. Kadavanich, Nature 404 59 (2000)

[3] D. V. Talapin, A. L. Rogach, M. Hasse, H. Weller, J. Phys. Chem. B 105 12278 (2001)

[4] B K Meyer, J Sann, D M Hofmann et al, Semicond. Sci. Technol. 20 S62 (2005)

[5] B. K. Meyer, H. Alves, D. M. Hofmann et al, phys. stat. sol. (b) 241 231 (2004)

List of publications & presentations

International publications

M. N. Jung, J. E. Koo, S. J. Oh, B. W. Lee, W. J. Lee, S. H. Ha, Y. R. Cho, and J. H. Chang, "Influence of growth mode on the structural, optical, and electrical properties of In-doped ZnO nanorods"
Appl. Phys. Lett. Vol.94, pp.041906(1)-041906(3), Jan, 2009.

Mina Jung, J.E. Koo, S.J. Oh, T.-I. Jeon, W.J. Lee, S.H. Park, J.S. Park, J.S. Ha, T. Yao, J.H. Chang, "A study on the indium induced variations in photoluminescence properties of Indium-doped ZnO nanorods"
International Journal of Nanoscience, Vol.8, pp.137-145, Jun, 2009.

M. N. Jung, E.S. Lee, T.-I. Jeon, K.S. Gil, J.J. Kim, Y. Murakami, S.H. Lee, S.H. Park, H.J. Lee, T. Yao, H. Makino, J.H. Chang, "Synthesis and investigation on the extrinsic carrier concentration of indium doped ZnO tetrapods"
Journal of Alloys and Compounds, Vol.481, pp.649-654, Mar, 2009.

D.C. Oh, S.H. Park, H. Goto, I.H. Im, M.N. Jung, J.H, Chang, T. Yao, J.S. Song, C.H. Bae, C.S. Han and K.W. Koo, " Influence on heat treatments on electrical properties of ZnO films grown by molecular-beam epitaxy"
Applied Physics Letters, vol. 95, pp.161908(1)-161908(3) 2009.

Mina Jung, Sunyeo Ha, Seungjun Oh, Jieun Koo, Jungjin Kim, Keisuke Kobayashi, Yoshihiro Murakami, Tae-In Jeon, Takafumi Yao, Jiho Chang, "Investigation on the electronic state of In-doped ZnO nanocrystals by hard X-ray photoemission spectroscopy"
Current Applied Physics, Vol.9, pp.e165-e168, Mar, 2009.

Jiho Chang, M.N. Jung, J.S. Park, S.H. Park; H. J. Lee, J. S. Ha, T. Fujii, T. Hanada, T. Yao, Y. Murakami, N. Ohtsu, G. S. Kil, "X-ray Photoelectron Spectroscopy Study on the CrN surface Grown on Sapphire Substrate to Control the Polarity of ZnO by Plasma-Assisted Molecular Beam Epitaxy"

Applied surface science, Vol.255, pp8582-8586, Jul, 2009.

Siyoung Kim, Woong Lee, Mina Jung, Jiho Chang, Khaing N Aung, Hongchan Lee, Junsuk Song, Dongcheol Oh, Seunghwan Park, Takafumi Yao, "Impact of ZnTe buffer on the electrical properties of n-type GaSb:Te films"
Applied surface science, Vol.256, pp1261-1264, Nov, 2009.

M.N. Jung, S.H. Ha, S.J. Oh, J.E. Koo, Y.R. Cho, H.C. Lee, S.T. Lee, T.-I. Jeon, H. Makino, J.H. Chang, "Field emission properties of indium-doped ZnO tetrapods"
Current Applied Physics, Vol.9, pp.e169-e172, Mar, 2009.

M.N. Jung, S.J. Oh, J.E. Koo, S.N. Yi, B.W. Lee, W.J. Lee, D.C. Oh, T. Yao, J.H. Chang, "One-step formation of ZnO nanorod bridge structure using geminated Si substrates by vapor phase transportation"
Current Applied Physics, Vol.9, pp.e161-e164, Mar, 2009.

J. S. Park, T. Minegishi, S. H. Lee, I. H. Im, S. H. Park, T. Goto, M. W. Cho, T. Yao, S. K. Hong J. W. Lee, J. Y. Lee, S. M. Ahn, H. S. Jeon W. Lee, M. N. Jung, and J. H. Chang, "Fabrication of 1D and 2D periodically polarity inverted ZnO structures using the patterned CrN buffer layers"
Journal of Vacuum Sci & Tech. B, Vol.27(3), pp.1658-1661, May/Jan, 2009.

M.N. Jung, S.H. Park, S.Y. Ha, S.J. Oh, Y.R. Cho, J.S. Park, I.H. Im, B.H. Koo, T. Yao and J.H. Chang, "Localization of the excitonic luminescence of ZnO nano-tetrapods"
Physica E, Vol.40, pp.2761-2764, Jun, 2008.

S.J. Oh, M.N. Jung, S.Y. Ha, S.G. Choi, J.J. Kim, K. Kobayashi, S.T. Lee, H.C. Lee, Y.R. Cho, T. Yao, J.H. Chang, "Microstructure evolution of highly Ga-doped ZnO nanocrystals"
Physica E, Vol.41 pp.31-35, Oct, 2008.

Woong Lee, Myunghoon Jung, Mina Jung, Hongchan Lee, Sangtae Lee, Seunghwan Park, Takafumi Yao, Joonsuk Song, Hangju Ko and Jiho Chang, "Structural deformation

reduction of ZnTe heteroepitaxial layers grown on GaAs substrates by using low-temperature buffer"
Journal of Cryst. Growth, Vol.304, pp.22-25, Mar, 2007.

M.N. Jung, S.Y. Ha, S.H. Park, M. Yang, H.S. Kim, W.H. Lee, Takafumi Yao, J.H. Chang, " Investigation of luminescence properties of ZnO nanostructure"
Physica E, Vol.31, pp.187-190, Feb, 2006.

M.N. Jung, S.Y. Ha, H.S. Kim, H.J. Ko, H. Ko, W.H. Lee, D.C. Oh, Y. Murakami, T. Yao, J.H. Chang, "The Shape Control of ZnO Based Nano-Structures"
Journal of Nanoscience and Nanotechnology, Vol.6, pp.3628-3632, Oct, 2006.

S.Y. Ha, M.N. Jung, S.H. Park, H.J. Ko, H. Ko, D.C. Oh, T.Yao, J.H. Chang, "Growth of Well-Aligned ZnO Nanorods using AuGe Catalyst by Vapor Phase Transportation"
Journal of Nanoscience and Nanotechnology, Vol.6, pp.3624-3627, Oct, 2006.

Mina Jung, Sunyeo Ha, Hangju Ko, Hyunchul Ko, Wookhyun Lee, Dongchul Oh, Takafumi Yao, and Jiho Chang, "Realization of a Low-threshold-voltage Field Emitter by Using High-quality ZnO Nano-tetrapod"
Journal of the Korean Physical Society, Vol.48, pp.1334-1337, Jun, 2006.

S. H. Park, J. H. Chang, M. N. Jung, Y. K. Park, K. Goto, T. Yao, "Interface disorder of $Zn_{1-X}Cd_XTe$/ZnTe multiple quantum wells grown by MBE using RHEED intensity oscillations"
J. Cryst. Growth, 278 311 (2005).

Mina Jung, Juyoung Lee, Seungwhan Park, Hongseung Kim, Jiho Chang, "Investigation of the annealing effects on the structural and optical properties of sputtered ZnO thin films"
J. Cryst. Growth, 283 384 (2005).

Domestic publications

J. E. Koo, M. N. Jung, S. J. Oh, S.N. Kim, S. N. Yi, J. H. Chang, S. H. Ha, Y. R. Cho, W. J. Lee, "Growth Mechanism of ZnO:In Nanorods and Application as Field Emission Device (FED)"
Sea Mulli (The Korean Physical Society) 57 231 (2008).

S. N. Kim, M. N. Jung, S. J. Oh, J. E. Koo, I. H. Heo, H. S. Ahn, S. N. Yi, J. H. Chang, H. J. Jung, B. W. Lee, H. H. Hwang, W. J. Lee, "Structural, Optical, and Electrical properties of ZnO:Al Nanorods grown by Using a AuGe Catalyst"
Sea Mulli (The Korean Physical Society) 57 238 (2008).

S.J. Oh, M.N. Jung, S.Y. Ha, S.G. Choi, J.H. Chang, J.J. Kim, K. Kobayashi, S.T. Lee, H.C. Lee, Y.R. Cho, "Investigations of the Growth Conditions and the Structural Evolution of Ga-doped ZnO Nanocrystals"
Sea Mulli (The Korean Physical Society) 56 303 (2008).

Siyoung Kim, Woong Lee, Mina Jung, Jiho Chang, Hongchan Lee, Sangtae Lee, Youngrae Cho, "GaSb Thin Films Grown on ZnSe/ZnTe Superlattice Buffer Layers"
Sea Mulli (The Korean Physical Society) 56 266 (2008).

S. H. Park, M. N. Jung, J. Y. Yi, M. Yang, H. S. Kim,J. H. Chang, D. C. Oh, J. J. Kim, "Effect of Structural Defect on the Electrical Properties of Thick GaN Films"
Sae mulli (The Korean Physical Society) 52 278 (2006).

하선여, 정미나, 박승환, 양민, 김홍승, 이욱현, Takafumi Tao, 장지호, "기판 표면의 영향에 의한 ZnO의 나노 구조 성장에 관한 연구"
한국해양정보통신학회 2005년도 춘계종합학술대회 9 1022 (2005).

장현경, 정미나, 박승환, 신대현, 양민, Takafumi Tao, 장지호, "Metal 증착한 Si 기판 상의 ZnO 나노 구조 특성"
한국해양정보통신학회 2005년도 춘계종합학술대회 9 1034 (2005).

정명훈, 박승환, 김광희, 정미나, 양민, 안형수, 장지호, 김홍승, "ZnSe 박막 성장을 위

한 Molecular Beam Epitaxy 성장 조선의 결정"
한국해양정보통신학회 2005년도 춘계종합학술대회 9 990 (2005).

김광희, 최석철, 이태훈, 정진우, 박승환, 정미나, 정명훈, 양민, Takafumi Tao, 장지호, "Grapoepitaxy법을 사용하여 SiO_2 기판 위에 제작한 ZnO 박막의 특성에 관한 연구"
한국해양정보통신학회 2005년도 춘계종합학술대회 9 1026 (2005).

정진우, 안현철, 이창용, 김광희, 최석철, 이태훈, 박승환, 정미나, 정명훈, 이호준, 양민, Takafumi Tao, 장지호, "주기적 표면 구조의 SiO_2 기판을 이용한 ZnO 박막의 Graphoepitaxy"
한국해양정보통신학회 2005년도 춘계종합학술대회 9 1042 (2005).

정미나, 하선여, 박승환, 양민, 김홍승, 이욱현, Takafumi Yao, 장지호, "서로 다른 ZnO 나노 구조의 형상에 따른 발광 특성의 조사"
한국해양정보통신학회 2005년도 춘계종합학술대회9 1013 (2005).

Presentations in the international conferences

M.N Jung, J.H. Chang, H-J. Lee, C.K. Kim, S.H. Park, J.E. Koo, H.S. Kim, J.S. Ha, H. Fujii, and T. Yao, The 8th international conference on nitride semicondoctors, ICC, Jeju, Korea (Octoboer, 2009), "Plasma assisted molecular beam epitaxy of GaN films on ZnO templates"

M.N. Jung, J.E. Koo,S.J.Oh, S.H. Ha, S.Y. Kim, Y.R. Cho, W.J. Lee, B.W. Lee, J.H. Chang, The 2008 Asian conference on nanoscience and nanotechnology, Biopolis, Singapore (November, 2008), "Enhancement of Field emission properties by In-doping in ZnO nanorods"

M.N. Jung, S.J. Oh, J.E. Koo, S.N. Yi, B.W. Lee, W.J. Lee, D.C. Oh, T. Yao, J.H. Chang, The 6th International nanotech symposium & exhibition, KINTEX, Korea (August, 2008), "Fabrication of ZnO-UV detector by one step nanowire growth using sandwiched Si substrate"

M.N. Jung, J.E. Koo, S.H. Ha, T.R. Cho, H.C. Lee, S.T .Lee, T.I. Jeon, H. Makino, J.H. Chang, The 6th International nanotech symposium & exhibition, KINTEX, Korea (August, 2008), "Field emission properties of ZnO:In Tetrapods"

M.N. Jung, S.Y. Ha, J.J. Kim, K. Kobayashi, H.C. Lee, S.T. Lee, T.I. Jeon, J.H. Chang, The 6th International nanotech symposium & exhibition, KINTEX, Korea (August, 2008), "Investigation on the electronic structure of ZnO:In nanocrystals by hard X-ray"

M.N. Jung, S.H. Ha, S.J. Oh, Y.R. Cho, G.S. Kil, T.I. Jeon, J.H. Chang, The 2nd International Conference on Display and Solid State Lighting, Convention & Exhibition (COEX), Seoul, Korea (January, 2008), "Realization of Field Emitter by using In-doped ZnO Nano-crystals"

Mina Jung, Sunyeo Ha, Sunggook Choi, Sanghoon Ha, Seungjun Oh, Taein Jeon, Jungjin Kim, Yoshihiro Murakami, Takafumi Yao and Jiho Chang, The 13thInternational Conference on II-VI Compounds, Hotel Shilla, Jeju, Korea (September, 2007), "Optical and Electrical Properties of InZnO Nano-Crystals"

Mina Jung, Sunyeo Ha, Hangju Ko, Yoshihiro Murakami, Jungjin Kim, Sanghyun Lee, Inho Im, Takafumi Yao and Jiho Chang, Asia Conference on Nanoscience & Nanotechnology (AsiaNano 2006), Busan, Korea (November, 2006), "Synthesis and Optical Analysis of InZnO Nanostructures"

M. N. Jung, S. Y. Ha, H. J. Ko, Y. Murakami, J. J. Song, T. Yao, J. H. Chang, IUMRS-ICA-2006 (MRS), Jeju, Korea (September, 2006), "Structural and optical properties of ZnInO nanostructures"

M. N. Jung, S. Y. Ha, H. J. Ko, Y. Murakami, J. J. Kim, T. Yao, and J. H. Chang, The 13th International Symposium on the Physics of Semiconductors (2006 ISPSA), Jeju, Korea (August, 2006), "The Investigation on the Morphological

Variation of the InZnO Nanostructures by In-Content"

M. N. Jung, S. Y. Ha, H. K. Jang, H. J. Ko, H. C. Ko, W. H. Lee, D. C. Oh, T. Yao and J. H. Chang, International Conference on Advanced Materials and Devices (ICAMD), Jeju, Korea (December, 2005), "Realization of Low Threshold Voltage Field Emitter by using High Quality ZnO Nano-Tetrapods"

M. N. Jung, S. Y. Ha, H. K. Jang, H. J. Ko, H. C. Ko, W. H. Lee, D. C. Oh, Y. Murakami, T. Yao and J. H. Chang, International Conference on Nanoscience and Nanotechnology, Gwangju, Korea (November, 2005), "The Shape Control of ZnO Based Nano-Structures"

M.N.Jung, J.Y.Lee, H.S.Kim, M.Yang, H.S.Ahn, J.H. Chang, The 3rd international workshop on ZnO and related materials, Sendai, Japan (Oct 5-8, 2004), "Structural and luminescence properties of post annealed ZnO films in H_2O ambient"

Acknowledgement

I want to thank the people who have helped make this thesis possible. First and foremost I would like to express extreme gratitude to my advisor, Prof. Jiho Chang for his invaluable guidance and mentorship. His inspirational guidance and encouragement enabled me to learn countless aspects of this research work. I believe the experiences he has shared and his advice which have made me a better researcher.

My special thanks to Prof. Samnyung Yi and Prof. Hyungsoo Ahn. They have been the head of our department for past several years and I will surely remember them for his words of advice, his insightful comments and the impressive speeches.

I am extremely thankful to Prof. Min Yang, Prof. Hongseung Kim, Prof. Bonheun Koo, Prof. Dongcheol Oh, Prof. Hyojong Lee, and Dr. Hangju Ko for their discussions and suggestions and for serving as my thesis committee members.

Heartfelt appreciation goes to Prof. Takafumi Yao for his support in many laboratory equipments and invaluable comments. I would like to express my deepest thanks to previous and present members of the Yao laboratory, especially Prof. Takenari Goto, Dr. Jungjin Kim, Dr. Katsushi. Fujii, Dr. Jun-seok Ha, Dr. Hyunjae Lee, Dr. Jinsub Park, Dr. Sanghyun Lee, Dr. Hyunjung Lee, Mrs. Yukiko Takahashi and Miss Koike Kayo. It has been a great pleasure knowing and learning with them.

In the course of this work, many people have assisted me. I am grateful to all members of the Nano Material and Device (NMD) laboratory, that I have been a part of, for their many helpful encouragement and stimulation over the five years. My special thanks go to Dr. Seunghwan Park, Mr. Kwanghee Kim, Mr. Woong Lee, Mr. Sungkuk Choi, Mr. Sanghun Ha, Mr. Siyoung Kim, Mr. Seungjun Oh,

Mr. Jinyeop Yoo, and Miss Miyeon Joo. Expecially, Dr. Park as a respectable senior of our laboratory gave me a consistent help and advices. Also, I would like to thank my junior, Miss Jieun Koo, Miss Sinae Kim, and Miss Youngji Cho, who have constantly supported and encouraged me. I am grateful to Mrs. Bongchun Lee, Dr. Kyoung Hwa Kim, and Miss Juyoung Lee for their assistance and encouragement in my life.

Finally, I would like to express my deepest thanks to all my family members, especially my parents, sister, brother-in-law, and nephew. They have stood by me throughout my studies with undying support and love. To them, I dedicate this thesis.